NUMERICAL AND EXPERIMENTAL INVESTIGATION OF EFFECTS OF POROUS LAYER ON COOLING OF ELECTRONIC COMPONENTS

EYUP KOÇAK

MARCH 2023

ÇANKAYA UNIVERSITY

GRADUATE SCHOOL OF NATURAL AND APPLIED SCIENCES

DEPARTMENT OF MECHANICAL ENGINEERING

Ph.D. Thesis in

MECHANICAL ENGINEERING

NUMERICAL AND EXPERIMENTAL INVESTIGATION OF EFFECTS OF POROUS LAYER ON COOLING OF ELECTRONIC COMPONENTS

EYUP KOÇAK

MARCH 2023

ABSTRACT

NUMERICAL AND EXPERIMENTAL INVESTIGATION OF EFFECTS OF POROUS LAYER ON COOLING OF ELECTRONIC COMPONENTS

KOÇAK, EYUP

Ph.D. in Mechanical Engineering

Supervisor: Prof. Dr. Haşmet Türkoğlu

March 2023, 151 Page

In this thesis, heat transfer and fluid flow characteristics over an electronic component covered with a porous medium were investigated both experimentally and numerically. For these purposes, an experimental setup was developed and constructed, and a computer program was developed using the OpenFOAM platform. The electronic component considered was modelled by a heat dissipating block made from brass. The heat dissipating block was made in the same dimensions as a real graphic processing unit (GPU). The top surface of the block was covered by a porous layer made from aluminum. To study the heat transfer from the block under different flow conditions, it was placed in a rectangular channel. To compare the role of the porous layer on cooling of the electronic components, both experimental and numerical studies were also conducted for the block without porous layer. The problem was assumed to be three dimensional, turbulent and steady.

In the experimental studies, the temperature distribution in the heat dissipating block was measured at different Reynolds numbers ($20000<Re<35000$) and heat generation values (6.72 W, 10 W, 14.2 W, 18.3 W) for both blocks with porous layer cover and without porous layer cover. From the measured data, the Nusselt number was calculated.

For numerical investigations, the problem was mathematically modelled using Darcy-Forchheimer approach. The k-ε turbulence model was used. It was assumed that the fluid and the porous layer material are in local thermal equilibrium (LTE). For the solution of the equations, a computer code based on OpenFOAM platform was developed. For the numerical solutions, the finite volume method and SIMPLE algorithm was used. A second order upwind method was used for the discretization of convective terms. The Gauss-Seidel iteration technique was used to solve the algebraic equations. Using the developed computer program, the velocity and temperature distribution within the solution domain (in flow, porous layer and block) were simulated. To check the validity of the numerical results, experimental results obtained in the present study and data from literature were used. For the heat transfer from the block, Nusselt numbers were calculated using the obtained temperature distribution. Numerical studies were conducted at different Reynolds numbers ($15000<Re<50000$), heat generation rate values (6.72 W, 10 W, 14.2 W, 18.3 W), porosity values ($0.55<\varphi<0.98$), the porous medium height to the channel height ratios ($0.064<h/H<0.66$), and the block width to the porous medium height ratios ($2.5<t/h<3.75$). Experimental and numerical results were used to develop a correlation equation and an artificial neural network architecture for Nusselt number.

From the results of the study, it was observed that porous mediums can be used as an alternative to the fin structures for electronic cooling applications. As the Reynolds number of the flow increases, the Nusselt number also increases. The porosity of the porous medium is an important parameter affecting the heat transfer rate. The Nusselt number increases with increasing porosity up to porosity of 0.9. However, with further increase in the porosity, the Nusselt number does not change considerable with increasing porosity at a given Reynolds number. The ratio of the height of the porous medium to the channel height (h/H) is another parameter that is important for the heat transfer. As the h/H ratio increases, the average heat transfer coefficient from the electronic components increases at a constant Reynolds number. The effects of the h/H ratio was evaluated by considering two different Nusselt number definition. The Nusselt number defined based on the hydraulic diameter decreases as the h/H ratio increases. The Nusselt number defined based on the height of the porous medium (h) increases as the h/H ratio increases. The width of the porous medium has no noticeable effect on the Nusselt number. The obtained correlation equation contains four different independent parameters contrary to the studies in the literature. By the

correlation equation developed, the Nusselt number can be obtained with a maximum error of 16.79% as a function of Reynolds number, Darcy number, porosity, and the ratio of porous medium height to channel height. Artificial neural network developed reveals as a better tool compared to correlation equation for the determination of Nusselt number. Using the artificial neural network architecture developed within the scope of the thesis, the Nusselt number can be obtained with a maximum error of 1% for similar systems.

Keywords: Porous Medium, Electronic Cooling, CFD

ÖZET

GÖZENEKLİ MALZEMELERİN ELEKTRONİK KOMPONENTLERİN SOĞUTULMASINDA ETKİSİNİN DENEYSEL VE SAYISAL İNCELEMESİ

KOÇAK, EYUP
Makine Mühendisliği Doktora

Danışman: Prof. Dr. Haşmet Türkoğlu
Mart 2023, 151 Sayfa

Bu tezde, gözenekli ortamla kaplı elektronik bir bileşen üzerindeki ısı transferi ve akış karakteristikleri deneysel ve sayısal olarak araştırılmıştır. Bu amaçla, bir deney düzeneği geliştirilmiş ve kurulmuş ayrıca OpenFOAM platformu kullanılarak bilgisayar programı geliştirilmiştir. Elektronik bileşen, pirinçten yapılmış bir ısı dağıtan blok modeli olarak modellenmiştir. Isıtılmış blok, gerçek bir grafik işlemci birimi (GPU) ile aynı boyutlarda üretilmiştir. Bloğun üst yüzeyi alüminyumdan yapılmış bir gözenekli malzeme ile kaplanmıştır. Bloktan ısı transferini farklı akış koşullarında incelemek için, blok dikdörtgen bir kanala yerleştirilmiştir. Elektronik bileşenlerin soğutmasında gözenekli tabakanın rolünü karşılaştırmak için, gözenekli tabaka olmadan hem deneysel hem de sayısal çalışmalar yapılmıştır. Problemin üç boyutlu, türbülanslı ve zamandan bağımsız olduğu kabul edilmiştir.

Deneysel çalışmalarda, ısıtılmış bloktaki sıcaklık dağılımı, gözenekli tabaka kaplanmayan ve kaplanan bloklar için farklı Reynolds sayıları ($20000<Re<35000$) ve ısı üretim değerleri (6,72 W, 10 W, 14,2 W, 18,3 W) altında ölçülmüştür. Ölçülen verilerden Nusselt sayısı hesaplanmıştır.

Sayısal çalışmalar için, incelenen problem matematiksel olarak Darcy-Forchheimer yaklaşımı kullanılarak modellenmiştir. k-ε türbülans modeli kullanılmıştır. Akışkan ve gözenekli tabaka malzemesinin yerel termal denge içinde olduğu varsayılmıştır. Denklemlerin çözümü için OpenFOAM platformuna dayalı bir bilgisayar kodu

geliştirilmiştir. Sayısal çözümler için, sonlu hacim yöntemi ve SIMPLE algoritması kullanılmıştır. Konvektif terimlerin ayrıklaştırması için ikinci derece Upwind yöntemi kullanılmıştır. Cebirsel denklemlerin çözümü için Gauss-Seidel iterasyon tekniği kullanılmıştır. Geliştirilen bilgisayar programı kullanılarak, çözüm alanındaki (akış, gözenekli tabaka ve ısıtılmış blok) hız ve sıcaklık dağılımı simüle edilmiştir. Sayısal sonuçların geçerliliğini kontrol etmek için, bu çalışmada elde edilen deneysel sonuçlar ve literatür verileri kullanılmıştır.

Elde edilen sonuçlar doğrultusunda, gözenekli ortamların elektronik soğutma uygulamaları için kanatçık yapılarına alternatif olarak kullanılabileceği gözlemlenmiştir. Akışın Reynolds sayısı arttıkça, Nusselt sayısı da artmaktadır. Gözenekli ortamın gözenekliliği, ısı transfer hızını etkileyen önemli bir parametredir. Nusselt sayısı, gözenekliliğin %90 değerine kadar artış göstermektedir. Ancak, gözenekliliğin daha fazla artmasıyla, Reynolds sayısı sabitken Nusselt sayısı artış göstermemektedir. Gözenekli ortam yüksekliği ile kanal yüksekliği oranı (*h/H*) ısı transferi için önemli bir parametredir. *h/H* oranı arttıkça, sabit Reynolds sayısında elektronik bileşenlerden ortalama ısı transfer katsayısı artar. *h/H* oranının etkileri, iki farklı Nusselt sayısı tanımı dikkate alınarak değerlendirilmiştir. Hidrolik çap temelli tanımlanan Nusselt sayısı, *h/H* oranı arttıkça azalır. Gözenekli ortam yüksekliği (*h*) temelli tanımlanan Nusselt sayısı, *h/H* oranı arttıkça artar. Gözenekli ortam genişliğinin Nusselt sayısı üzerinde fark edilir bir etkisi görülmemiştir. Elde edilen korelasyon denklemi, literatürdeki çalışmaların aksine dört farklı bağımsız parametre içermektedir. Geliştirilen korelasyon denklemi ile Nusselt sayısı, Reynolds sayısı, Darcy sayısı, porozite ve gözenekli ortam yüksekliği ile kanal yüksekliği oranının fonksiyonu olarak %16,79 maksimum hata ile elde edilebilir. Tez kapsamında geliştirilen yapay sinir ağı mimarisi, korelasyon denklemine kıyasla daha iyi bir araç olarak ortaya çıkmıştır. Yapay sinir ağı mimarisi kullanılarak, benzer sistemler için Nusselt sayısı %1 maksimum hata ile elde edilebilir.

Anahtar Kelimeler: Gözenekli Ortam, Elektronik Soğutma, HAD

ACKNOWLEDGEMENT

I would like to express my sincere gratitude to my supervisor Prof. Dr. Hasmet Turkoglu for his continuous support, patience and motivation during my study. I have benefited greatly from his wealth of knowledge and meticulous editing. I also thank to my committee members Prof. Dr. Nuri Yucel, Assoc. Prof. Dr. Ulku Ece Ayli, Assoc. Prof. Dr. Ekin Ozgirgin Yapici and Assist Prof. Dr. Salih Karaaslan for their continuous support and encouragement.

I would also like to say a heartfelt thank you to my mom Havva Kocak, my dad Prof. Dr. Saim Kocak and my sister Elif Kocak for always believing in me and encouraging me to follow my dreams.

I would like to express my sincere gratitude to Dr. Levent Bilir from TUBITAK MAM for providing the porous material used in the experimental studies.

I would also like to acknowledge the financial support provided by Cankaya University Scientific Research Projects Unit, which has been essential in covering various expenses related to experimental part of this thesis.

TABLE OF CONTENTS

LIST OF TABLE

LIST OF FIGURES

LIST OF SYMBOLS AND ABBREVIATIONS

SYMBOLS

a	:Algebraic equation coefficient
A	:Surface area, m^2
A_c	:Cross sectional Area, m^2
A_{ins}	:Block surface area in contact with the insulation material, m^2
c	:Filtering coefficient
C_f	:Specific heat at constant pressure, J/kgK
C_{solid}	:Specific heat of block material
f	:Frequency, Hz
d_b	:Bead diameter, m
D_h	:Hydraulic diameter, m
g	:Gravitational acceleration, m/s^2
G_k	:Turbulent Kinetic Energy Production
h	:Heat transfer coefficient, W/m^2K
I	:Current, A
k	:Thermal conductivity, W/mK
k_s	:Thermal conductivity of solid material of porous medium, W/mK
k_{solid}	:Thermal conductivity of heated block, W/mK
k_{ins}	:Heat conduction coefficient of the insulating material, W/mK
k_f	:Thermal conductivity of fluid, W/mK
K	:Permeability, m^2
L	:Length, m
L_c	:Characteristic Length, m
Nu	:Nusselt number based on hydraulic diameter
Nu*	:Nusselt number based on porous medium height
P	:Pressure, Pa
P*	:Estimated pressure, Pa

P'	:Pressure correction
Pe	:Peclet Number
Pr	:Prandtl Number
Pr_t	:Turbulent Prandtl number
R	:Dependent Variable
Re	:Reynolds number based on channel hydraulic diameter
Re_{Dp}	:Reynolds number based on pore diameter
S	:Source term
t	:Porous medium width, m
T	:Temperature, K
T_i	:Air inlet temperature, K
T_p	:Average block temperature, K
q"	:Heat flux, W/m^2
q"'	:Heat generation, W/m^3
Q	:Total heat, W
Q_{conv}	:Surface to air heat transfer by convection, W
Q_e	:Total amount of electric power, W
Q_{rad}	:Total amount of heat transfer by radiation, W
u	:Velocity component in x-direction, m/s
v	:Velocity component in y-direction, m/s
V	:Velocity, m/s
w	:Velocity component in z-direction, m/s
W	:Width, m
W_R	:Amount of error
x	:Horizontal Coordinate
x_i	:Measured raw value
y	:Vertical Coordinate
y_n	:Filtered value
y_{n-1}	:Filtered value at previous instant
α	:Heat diffusion coefficient, m^2/s
δ	:Constant for source term
ΔT	:Temperature difference, K
Δx	:Insulation thickness, m

ρ	:Fluid density, kg/m^3
μ	:Dynamic viscosity, kg/ms
μ_{eff}	:Effective viscosity, kg/ms
μ_{lam}	:Laminar viscosity, kg/ms
μ_t	:Turbulent viscosity, kg/ms
φ	:Porosity
ν	:Kinematic viscosity, m^2/s
ϕ	:Field variable
Γ	:Diffusion coefficient
Γ_{eff}	:Effective total heat diffusion coefficient
ε	:Emissivity
σ	:Stephen-Boltzmann Coefficient, $5.670x10^{-8}$ W/m^2K^4

ABBREVIATIONS

ANN	:Artificial Neural Network
BR	:Bayesian Regulation training algorithm
CFD	:Computational Fluid Dynamics
LM	:Levenberg-Marquardt training algorithm
PDE	:Partial Differential Equation
PPI	:Pore per inch
SCG	:Scaled Conjugate Gradient training algorithm
TC	:Thermocouple

CHAPTER I
INTRODUCTION

Thermal management of electronic devices has been one of the important areas of heat transfer research. Electronic devices usually contain chipsets placed in an enclosure to protect the chips from the environment. This enclosure provides a safe zone and physical miniaturization of the electronic equipment. Miniaturization applications decrease equipment size; however, thermal management for reliable and efficient operation becomes an issue. Increasing demand for high system performance intensifies the heat released from electronic components. Hence, advanced materials and an excellent thermal design are crucial for developing electronic equipment. To increase the performance and reliability of electronic components, researchers focus on cooling of electronic systems to keep the temperature of electronic components below the safe temperature when they are operating.

Figure 1 shows a motherboard manufactured by Intel for a desktop computer. A chip is a slice of single-crystal silicon consisting of microscopic electronic circuits. It may be enclosed in a package to isolate the chip from the environment. The package contains multiple electrical leads to transmit the pulsed signal to another electronic component. A module is formed by attaching several chips to the same package. Packages or modules are then mounted on a printed circuit board (PCB), where layers of conductor networks are fabricated to connect different modules electrically. The electronic component implemented in the computer graphic cards and motherboards consist of printed circuit boards, a power supply, and a fan.

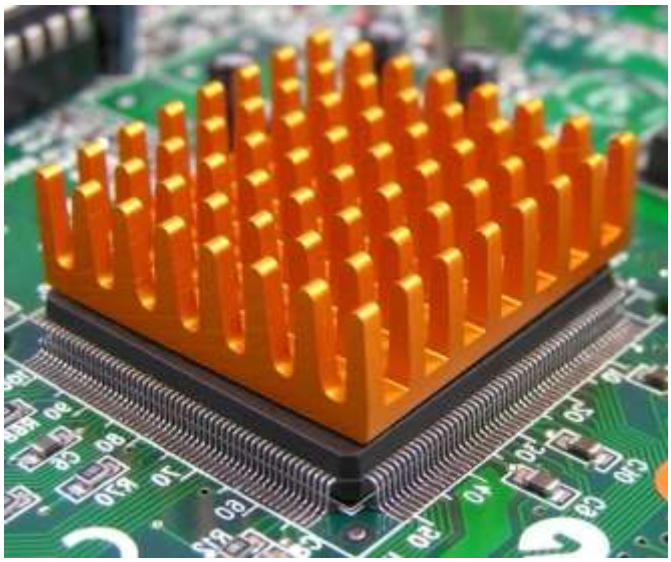

Figure 1.1: A CPU and its cooling attachment used by Intel Corporation.

Electronic packages are composed of chips, fins, and thermal interfaces. These are shown schematically in Fig. 1.2. From the thermal management point of view, the chip may be considered as a heat source in a package. The fins are structural members, which diffuses the heat generated by chips to the environment through the extended heat transfer surface formed. For high-power chips, thermal interfaces made from a highly conductive plate in contact with the chip surface are used to diffuse heat from the chip to the finned structure. Fins attached to the exterior of the package act as heat spreaders.

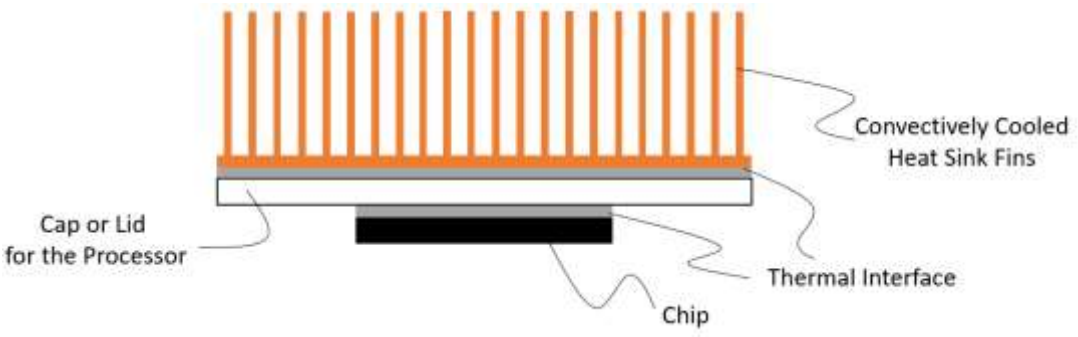

Figure 1.2 : Schematic view of a chip and heat sinks.

The thermal control system of an electronic component may consist of several tasks: Removing heat from the sources (chips), transporting the heat to the fin arrays, and transferring the heat from the internal heat sink (fins) to the environment or cooling fluid. These tasks require a well-designed efficient system that fulfills several features such as performance, reliability, small size, manufacturability, compatibility, and cost.

In today's electronic equipment, various cooling systems and coolants are used utilizing different heat transfer methods. All those methods can be grouped as air-cooling and liquid-cooling techniques. Air is widely used as a coolant due to its low cost and high reliability. Its availability in the desired amounts, low cost, and easy maintenance makes air the right choice for many cooling applications. Nevertheless, water is also widely used as a coolant for desktop computers due to high cooling load requirements, especially for GPUs and CPUs. Convection heat transfer is the primary heat transfer mode in air and water cooling applications, although conduction and radiation also have to be considered. The comparison of cooling capabilities of different heat transfer modes is given in Fig 1.3 (Incropera 2007). Figure 1.3 highlights the importance of choosing the appropriate convection method and heat flux values to ensure that electronic components remain within their thermal design limits. The figure presents four different convection methods, which are direct air with natural convection, direct air with forced convection, immersion with natural convection, and immersion with forced convection. Each method is associated with a range of surface heat flux values that can be released from the electronic component. When using direct air with natural convection, the range of released surface heat fluxes from the electronic component that will maintain a temperature below the thermal design limit is between 1000-3000 W/m^2. However, if the surface heat flux is between 3000-6000 W/m^2, the electronic component temperature will exceed the thermal design limit (Steinberg 1991)

Direct air flow with forced convection, on the other hand, can handle a slightly higher range of released surface heat fluxes from the electronic component, which is between 1000-5000 W/m^2. However, to keep the temperature under the thermal design limit, the surface heat flux must be between 1000-5000 W/m^2. If the surface heat flux exceeds 6000 W/m^2, the component temperature will exceed the thermal design limit. (Steinberg 1991)

The immersion method can handle a much higher range of released surface heat fluxes from the electronic components, depending on whether natural or forced convection is used. With immersion and natural convection, the temperature will exceed the thermal design limit when the surface heat flux is around 7000 W/m^2. On the other hand, when using immersion with forced convection, the temperature will exceed the thermal design limit when the surface heat flux is around 10000 W/m^2 (Steinberg 1991).

The heat flux of an electronic component (GPU or CPU) during operation can vary depending on the specific model, but it generally falls within the range of 1000 to 5000 W/m^2 (Intel Corporation 2018). This means that forced convection using air is a suitable cooling method for many electronic devices, as it can effectively dissipate heat at these heat flux levels. However, high-end graphics cards designed for demanding applications such as gaming, video editing, or scientific computing can generate even higher heat fluxes, typically in the range of 5000 to 8000 W/m^2 (Intel Corporation 2018). As Fig. 1.3 shows, if the heat flux exceeds 5000 W/m^2, the use of forced convection with air may not be sufficient to keep the component temperature within its thermal design limits. In such cases, forced convection with water generally preferred by manufacturers to prevent the component from overheating.

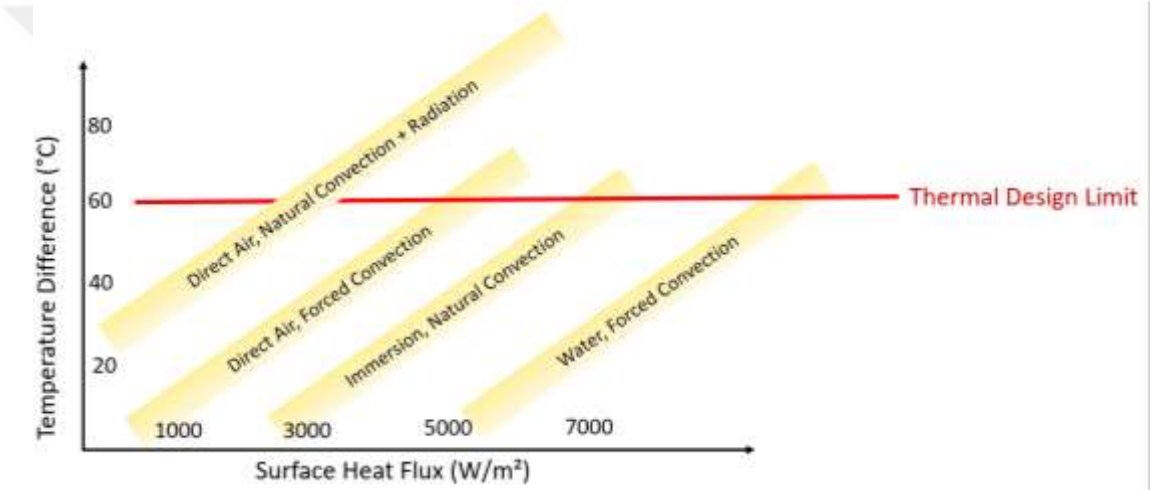

Figure 1.3 : Comparison of cooling capabilities of different techniques and coolants used for electronic cooling (Incropera 2007).

As previously indicated, fin-array structures are often preferred in electronic cooling applications. However, high-performance chips require high electrical power, which means current passes through extremely small cross-sections, causing the transistors (chips) to heat up. This effect is then multiplied by the sheer amount of transistors present in a component. Hence, the cooling load capacity of the fin structures is constrained to maintain chip temperatures below the thermal design limits. Hence, in recent years, porous layers have been used instead of fin arrays.

This thesis study focuses on heat transfer enhancement using porous mediums as a cooling attachment instead of conventional fin-array structures for electronic cooling applications. In this context, the study consists of three parts:

- In the first part, an experimental system is designed and constructed to experimentally investigate the heat transfer behavior of porous mediums. The effect of an aluminum porous medium placed on a heated brass block which is in the same size as an actual graphic card (GPU) was studied in terms of heat transfer.
- In the second part, the OpenFOAM-based Computational Fluid Dynamics (CFD) code was developed for conducting numerical simulations. The effects of geometric dimensions and characteristics of the porous medium at different flow conditions on heat transfer were analyzed in detail.
- In the third part, an artificial neural network (ANN) model with a three-layer feedforward neural network was adopted to obtain the Nusselt number on the basis of four inputs for electronic cooling applications using porous mediums. In this part, a Nusselt number correlation equation was also developed based on the Reynolds number, Darcy number, porosity, and the ratio of the height of the porous material to the channel height.

The outline of the thesis is as follows:

- In Chapter 2, the related fundamental concepts and the previous studies found in the literature are summarized and the state-of-art is given in detail.
- In Chapter 3, the methodology used throughout the experimental study is explained. The experimental setup is described, data collection and analysis methods are explained, the results are presented in terms of the component temperature and Nusselt number.
- In Chapter 4, physical description of the problem is given and governing equations are derived, and boundary conditions are given. Turbulence model used is also formulated.
- In Chapter 5, the numerical method used and the computer program developed is explained. The numerical method verification results are also presented.
- In Chapter 6, the results obtained from the experimental study are presented.
- In Chapter 7, the numerical results are presented.
- In Chapter 8, the statistical method used to correlate Nusselt number and the methodology of artificial neural network study are explained. Architecture of the artificial neural network used is described. In addition to the ANN, a

Nusselt number correlation equation based on four dimensionless parameters is presented.

- In Chapter 9, the study is summarized. Conclusions, contributions to the literature, and recommendations for future studies are presented.

CHAPTER II
FUNDAMENTAL CONCEPTS AND LITERATURE SURVEY

In this chapter, fundamental concepts related to porous materials and studies found in the literature about heat transfer and flow characteristics in finned structures and porous mediums are summarized.

2.1 FUNDAMENTAL CONCEPTS

The use of porous mediums is one of the passive heat transfer enhancement techniques. Characterization of the porous mediums for heat transfer and fluid flow studies is difficult due to their random nature and geometric complexity. Different types of porous materials are shown in Fig.2.1. The basic properties and some classical theories about heat and fluid flow in porous mediums are explained in this section. Porous materials are characterized by the properties porosity, pore density, permeability and Darcy number. These properties related to the porous materials are explained below.

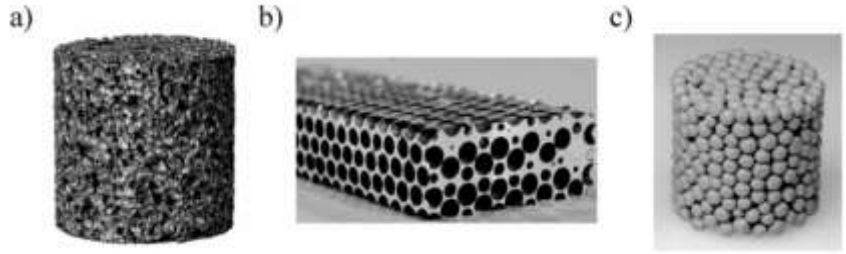

Figure 2.1: Different types of porous materials: a) Closed-cell metal foam, b) Hollow alumina spheres embedded in a magnesium matrix, c) Hollow sphere foam (Fiedler et al. 2006).

2.1.1 Porosity

The ratio of pore (fluid) volume to the total volume of the porous medium is defined as porosity (φ), and can be expressed as;

$$\varphi = \frac{v_{fluid}}{v_{total}} \tag{2.1}$$

where v_{fluid} is volume occupied by fluid (pore volume) and v_{total} is the total volume of the porous medium. Thus, 1- φ is the fraction that is occupied by the solid matrix.

The voids (pores) of the porous medium can be in two different types: (1) open-cell porous medium that voids are connected to each other, and (2) closed-cell porous medium that voids are not connected with each other. Generally, heat and fluid flow is investigated in open-cell porous media due to the permeability that allows fluid flow inside the medium. The porosity is mostly between 0.2 and 0.6 for natural mediums such as sand, soil, and coal. However, this value approaches to one in human-made materials such as aluminum or brass foams (Nield and Bejan 2012:1).

2.1.2 Pore Density

Pore density (PPI) defines the number of pores (voids) per inch square. Commercial foams generally exhibit a pore density ranging from 10 to 100 pores per inch (PPI), corresponding to porosity ranging from 88 to 95%. Scaled photographs of aluminum foams with various PPI values are shown in Fig. 2.2.

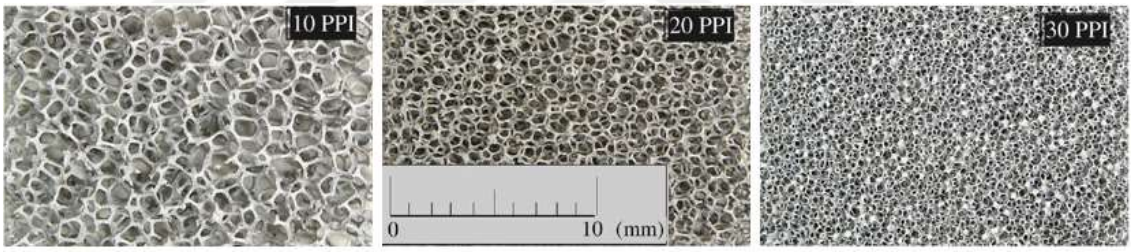

Figure 2.2: Photographs of aluminum foams with various pore densities (PPI values) (Kurtbas and Celik 2009)

2.1.3 Permeability and Darcy Number

Permeability (m^2), *K*, is the ability of the porous medium to transfer fluid flow inside its structure. The structure of the porous medium determines the permeability. The high permeability means less pressure loss of the fluid passing through the porous structure. Estimation of the permeability is done for each specific type of porous material, and it may vary according to the production method of the porous material (Nield and Bejan 2012).

Darcy number is a dimensionless number, which describes the relative effect of the permeability of the medium versus its cross-sectional area. Darcy number can be formulated as follows (Nield and Bejan 2012)

$$Da = \frac{K}{L_c^2} \tag{2.2}$$

where K is permeability and L represents the characteristic length of the system considered. Characteristic length could be the length of a fully filled cylindrical column or the height of the porous medium for partial usage applications.

2.1.4 Modelling the Heat Transfer in a Porous Medium

A porous material consists of small irregular pores (passages) and thin solid material. The sizes of the pores and solids in a porous material are in the order of millimeters. As seen in Fig 2.3., fluid flows through small pores, and heat transfer occurs between the fluid and the solid material.

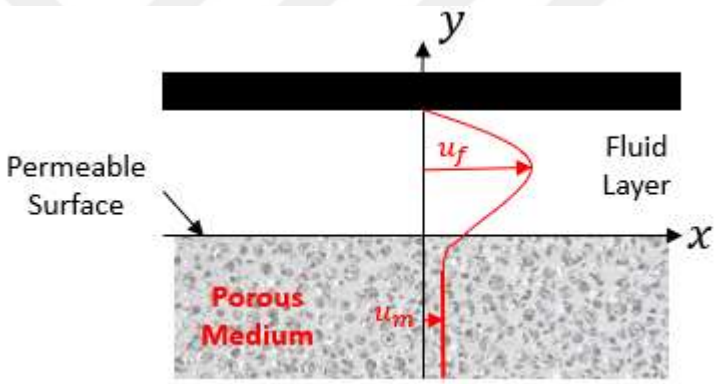

Figure 2.3: Velocity profile across the porous medium and in free stream region.

The fundamental problem in heat transfer through porous media is the prediction of the heat transfer rate between the free stream flow and the fluid-saturated porous medium. In practice, the heat transfer measurement is challenging in porous mediums due a thermal gradient during the fluid flow across the porous medium (Bauer 1993, Ghanbarian and Daigle 2016). Besides radiative effects, viscous dissipation, the work done by pressure, and the solid and fluid thermal conductivities are also factors to be taken into account. The most important of these factors is the thermal conductivity of the material. Generally, the thermal conductivity of solid material is much higher than the thermal conductivity of fluid flowing in a porous medium. As a natural consequence, thermal conductivities should be considered to solve the heat transfer in porous mediums mathematically. In addition, there may be no thermal equilibrium between the solid and fluid phases inside the porous medium

in a real case. In such situations, the heat transfer coefficient (h) should be known or calculated to solve energy equations. For high-speed transients and when a heat generation exists in the solid or fluid phase, a non-equilibrium treatment should be made. However, if there is no heat generation and the problem is assumed to be steady, a thermal equilibrium can be considered where solid and fluid phase temperatures are equal. Consequently, depending on the pore structure, material conductivity, flow conditions, etc. generally following two approaches are used to model heat transfer in porous mediums:

1) Local thermal equilibrium method,

2) Thermal non-equilibrium method.

Studies following both approaches may be found in the literature. Energy equations that include different assumptions will be given in Chapter 4.

2.2 LITERATURE SURVEY

The removal of heat generated in electronic and mechanical systems is important in terms of efficiency, safety and system life. Especially in electronics, automotive, aerospace, ventilation and many other applications, the heat removal from the heat generating systems and effective transfer of the heat from one environment to another remain as important issues. Active and passive heat transfer methods have been developed to remove (cooling) heat from these systems. Active methods remove heat from the system by equipment that requires a motor drive. Passive thermal control methods involve no equipment which requires a motor drive. An increase in heat transfer is ensured through modifications made in geometry, surface size, material, etc., ensuring that the temperatures of the heat-generating elements remain below the safe operating temperature (Liu and Sakr 2013, Nagarani et al. 2014). In a passive method, heat transfer occurs by natural convection. Increasing the heat transfer area by placing fins on the heated surface is very common due to its low cost and ease of application (Jeng and Tzeng 2007). However, especially in electronic cooling applications, the amount of heat removed from the heated surface by natural convection is not sufficient for safe operating conditions. Therefore, using a finned structure and fan to pressurize the fluid is preferred. In recent years, the use of porous materials instead of finned structures has become an alternative technique.

2.2.1 Heat Transfer Studies using Fin-Array Combinations

In the literature, the effects of the geometries of the finned structures (circular, square, rectangular, triangular etc.) on heat transfer are a thoroughly studied subject. Rectangular cross-section fins are one of the most preferred fin geometries because of their low cost, and easy manufacturability. Researchers have been studying the impact of rectangular fins on heat transfer since the mid-20th century and have contributed to the literature (Ko et al. 1989). Heat transfer with perforated and truncated rectangular fin structures are common fin types that have been operating for the past 20 years. Studies with different fin types are conducted experimentally, numerically and analytically, and these studies aim to achieve theoretical definitions and empirical correlations. The ability to increase heat transfer by natural and forced convection depends on parameters such as fin length, fin height, the distance between fins, fin thickness, fin material, and fin number. Several studies have been conducted to investigate the effect of the parameters mentioned.

Harahap and McManus (1967) investigated the heat transfer performance of a rectangular fin array under natural convection conditions. The fin array was positioned with the base oriented horizontally, and the average heat transfer coefficients were determined experimentally. At the end of the study, collected experimental data was used to obtain a new correlation that can overcome the inadequacy of parameters of previously offered correlations to calculate more sensitive heat transfer coefficient values.

Jones and Smith (1970) suggested a correlation equation to determine the heat transfer coefficient for natural convection fin array problems. The researchers collected data that included seventy-two combinations of array parameters such as fin height, fin spacing, and temperature difference between the heated surface and the environment. At the end of the study, a correlation was offered to calculate more sensitive heat transfer coefficient under natural convection conditions. The researchers also suggested a preliminary design procedure to achieve an array that dissipates more heat from the heated surface.

Leung et al. (1985) studied a horizontal rectangular duralumin fin array in a rectangular channel to investigate the heat transfer performance of vertical and horizontal fin arrays by natural convection. Firstly, the optimal separations were determined to obtain the highest heat loss rate for both positions of the arrays. The uniform fin base temperature was kept between 40˚C and 80˚C and the ambient

temperature was 20˚C. Experiments have shown that, for the same geometric shape, fin arrays that are arranged vertically have the highest heat loss rates.

Ko et al. (1989) studied a similar natural convection problem in order to determine the effect of fin material on heat transfer. Duralumin and stainless-steel materials are used to manufacture a fin array that has rectangular fins. The distance between fins is also kept constant, and the steady-state heat dissipation rates are obtained under natural convection conditions. The experimental data was compared for both case studies, and the results showed that even though the thermal conductivity of the material is almost doubled, the maximum heat loss rates change by around 3.5%.

Harahap and Seti (2001) collected data from experimental studies with five duralumin vertical fin arrays horizontally oriented. The goal was to obtain two types of Nusselt number correlation equations that were valid over a wide range. One of the correlation equations used the distance between fins as the prime geometric parameter. The second correlation equation used fin length as a prime parameter. Researchers reported that these two correlation equations could calculate the Nusselt number more precisely for similar systems.

Awasarmol and Pise (2015) investigated a perforated fin array under natural convection conditions. Different inclination angles (0-90) and perforation parameters (4-12 mm) were used to increase the heat transfer coefficient. The results showed that the highest heat transfer coefficient was obtained at 12 mm perforation and a 45° angle of orientation. The heat transfer coefficient was increased by around 30% compared to the standard fin array arrangement under the same conditions.

The literature survey showed that the heat transfer coefficient for the fin array cooling systems under natural convection conditions is below 20 W/m^2K (Ahmadi et al. 2014, Alessa et al. 2008, Awasarmol and Pise 2015). However, these heat transfer coefficient values obtained by natural convection are not sufficient for electronic cooling applications (Lee et al. 2017). Therefore, researchers focused on cooling methods using similar geometric combinations under forced convection to get higher heat transfer coefficients (Ledezma and Bejant 1996).

Peng (1984) conducted an experimental study to determine the heat transfer performance of full cross-pin fin arrangements. In this study, the function of the pin fins is to increase the heat transfer area and act as a vortex promoter. However, pin fin positions over the heated surfaces would create higher pressure losses. In order to determine optimum arrangement specifications, pin height, spacings and channel

height-to-length ratio were investigated experimentally. Results showed that the fin height is the critical parameter for higher heat transfer rates.

Olson (1992) measured the heat transfer coefficient and pressure drop of three different heat transfer experimental setups using helium as a fluid for Reynolds numbers between 450 to 36000. All of the setups have the same length and width. In order to determine which setup has the highest heat transfer rate, several cases are conducted for different Reynolds numbers. The first setup includes circular tubes placed inside a rectangular channel, the second setup is classic channel flow, and the third setup has a fin-pin array in a rectangular channel. Experimental results show that pin-fin array transfers heat around five times better than others. Olson (1992) also offers a correlation equation to determine the Nusselt number and friction factor for similar problems.

Another experimental study was conducted by Tahat et al. (2000) to determine the effect of pin-fin spacing on forced convection heat transfer. Uniform heat flux was applied to the heated fin base, and all combinations of the fin arrays were tested in the same flow conditions. All experiments were conducted for Reynolds numbers between 3000 to 10000. Results showed that heat transfer coefficients could be increased by almost double (~25 to ~50 W/m^2K) for the same Reynolds number using the optimum design of fin-array attachment. A Nusselt number correlation equation was also presented to choose the optimal design for steady-state laminar flows.

Dogan and Sivrioglu (2009) investigated mixed convection heat transfer from longitudinal fins inside a horizontal channel in a natural convection-dominated region. An experimental parametric study was conducted on the effects of fin spacing and fin height for Re=250. Their experimental study showed similar behavior as previous studies. The average convection heat transfer coefficient increases first with fin spacing. Then it takes a maximum value, after which it starts to decrease with the increased fin spacing. For their case study, the optimum heat transfer coefficient was obtained around d/H=0.18.

Adhikari et al. (2020) focused on characterizing the optimum heat transfer and flow patterns using three-dimensional, steady-state, laminar, and conjugate heat transfer simulations in order to determine optimum fin structure under natural convection operating conditions. Their heat transfer simulations showed a good agreement with the experimental results. The developed numeric model showed that heat transfer coefficient behavior is similar to previous studies, and researchers believe

optimal geometric parameters should be investigated separately for each design and operating condition. Researchers declared that it is possible to observe velocity vectors and temperature contours to understand heat transfer behavior using CFD.

Ayli et al. (2016) conducted an experimental and numerical study to investigate heat transfer from rectangular fins for fully turbulent flow. The experimental results were used to verify the numerical methodology. k-ε, k-ω and k-ω SST turbulence model results were compared with the experimental results to determine which turbulence model can predict better heat transfer and flow phenomena. Nine different fin configurations were simulated to determine the heat transfer coefficient for each test case. At the end of the study, a Nusselt number correlation equation was presented for turbulent flows. It is also possible to increase heat transfer coefficients using geometrically modified fin structures such as interrupted, perforated, dimpled, or drop-shaped fin arrays in cases in which increasing the heat transfer coefficient is much more important than the manufacturing costs (Ahmadi et al. 2014, Awasarmol and Pise 2015, Chang et al. 2016, Sahin and Demir 2008, Wang et al. 2012, Aldoori 2021).

In summary, previous studies about cooling with fin array applications have shown that heat transfer coefficients are generally limited to 300 W/m^2K on forced convection heat transfer. However, in recent years, heat dissipation from electronic components, particularly in graphics cards and CPUs, has increased. To remove such high heat dissipation from the electronic components, fan speeds have been increased while simultaneously raising the Reynolds number to achieve higher heat transfer coefficients. However, this technique results in increased fan noise and energy usage. Hence, more effective techniques need to be developed. One way to increase heat transfer coefficients has been the utilization of geometrically modified structures. As a result, the concept of employing porous materials, which offer higher heat transfer possibilities, has become and alternative approach.

2.2.2 Heat Transfer Studies using Porous Medium

In recent years, as part of both passive and active thermal control methods, the effects of porous mediums on heat transfer have been examined. The results have shown that it is possible to effectively transfer heat from a source to the environment using porous mediums. In order to increase the heat transfer rate using porous mediums, some researchers have focused on the material characteristics of the metal

foams and properties (porosity, pore density, darcy number, etc.) of the porous medium. Lots of analytical, experimental and numerical studies have been carried out.

Hyung et al. (1995) conducted an interchannel forced convection experiment using porous mediums. The researchers examined the effects of the porous material thickness and width and the channel height. It was demonstrated that as the thickness of the porous structure increases, the velocity of the fluid in contact with the heated surface increases due to the constricted flow area. It was also shown that the loss of channel pressure increases as the thickness and width of the porous medium increase.

Izadpanah et al. (1998) performed an experimental and numerical study, and investigated the temperature and pressure changes that occur when a constant heat flux is applied to a porous medium. Experimental results were compared to the numerical solution of a mathematical model. The comparison showed that the numerical results differed by 10% from the experimental results. At the end of the study, it was demonstrated that realistic results could be obtained with the use of a mathematical model formed with Darcian assumptions.

Ko and Anand (2003) examined the effect of porous media on heat transfer with sequential structure placed in the channel experimentally. Researchers investigated heat transfer coefficients and pressure losses when the porous medium is attached periodically to the upper and bottom walls of the channel. Porous structures were made of aluminum with the same porosity (φ=0.92) but had different pores per inch (10, 20 and 40 PPI). The results obtained revealed that the number of Nusselt increases as the number of pores increases and that this value may increase three-fold compared to flat vanes. They also determined that the coefficient of friction increased as pore density increased.

One example of the heat transfer characteristics of porous mediums is presented by Hsieh et al. (2004). Researchers experimentally investigated the effects of porosity (ε), pore density (PPI), and air velocity on the heat-transfer characteristics of aluminum-foam heat sinks. Experimental results show that the Nu increases as the pore density increases due to the fact that aluminum foam with a larger pore density has a larger heat-transfer area. As a result, the Nusselt number increases with the increase of porosity. Researchers also observed that temperatures of the solid and gas phases of the aluminum foam decrease as the Reynolds number increases, caused by the increased convective heat-transfer rate at a higher Reynolds number. The

temperature difference increases with the decrease of Reynolds number and the distance away from the heat source.

Leong and Jin (2005) carried out an experiment on heat transfer in an oscillating flow through an aluminum foam-filled channel, under a constant wall heat flux. They analyzed the pressure drop characteristics and the effects of oscillating flow on heat transfer by measuring the surface temperature distribution on the wall, the flow velocity through the porous channel, and the pressure drop across the test section. The results of their study showed that the use of porous media in a plate channel significantly enhances heat transfer in oscillating flow. They also obtained a correlation equation for the length-averaged Nusselt number, which depends on the Reynolds number and the flow displacement, for a specific porous channel.

Tzeng and Jeng (2006) have investigated the convective heat transfer and pressure drop in porous channels with 90-deg turned flow. As a porous medium, aluminum foams with a porosity of 0.93 were used in their experimental study. The effect of the variable geometric and porosity parameters were investigated experimentally, and results showed that for the 90 degrees turned flow, increasing Re increases the average Nusselt number (Nu). On the other hand, the effects of the width-height ratio and PPI of porous mediums are negligible on heat transfer.

Lu et al. (2006) studied forced convection heat transfer characteristics in high-porosity open-cell metal-foam-filled pipes. The Brinkman-extended Darcy momentum model and the two-equation heat transfer model for porous media were employed in their analytical model. Based on the analytical solutions, they obtained the velocity and temperature distributions in metal-foam-filled pipes. The effects of the microstructure of metal foams on overall heat transfer were examined. The results show that the pore size and porosity of metal foams play important roles in overall heat transfer performance. The use of metal-foam can dramatically enhance the heat transfer but at the expense of higher pressure drop.

Tzeng, (2007) investigated the spatial thermal regulation of an aluminum foam heat sink using a high-conductivity conductive pipe. In this study, four different case study prepared to examine the heat transfer coefficient of the porous medium and its effects. The range of Reynolds number was limited to 4416, and results indicated that the conductive pipe in the porous heat sink was useful in spatial thermal regulation. However, the conductive pipe in the aluminum foam heat sink does not improve overall heat transfer for their test conditions. Another study on convective heat transfer

in an annulus filled with aluminum foam investigates non-Darcy flow and the effect of high porosity foams on heat transfer (Noh et al. 2006). The results show that aluminum foam enhances heat transfer from a surface compared with that of laminar flow in a clear annulus. Researchers also developed correlations for the friction factor and the Nusselt number based on their experimental results.

Calmidi and Mahajan (1999) conducted both experimental and numerical studies on forced convection in metal foams. Their experimental investigations involved the use of aluminum metal foams with different porosities and pore densities, and air as the fluid medium. They obtained the Nusselt number as a function of the pore Reynolds number. In their numerical study, they used a semi-empirical volume-averaged form of the governing equations, which was validated with the experimental data. The empirical constants were determined based on the numerical and experimental data. They proposed a correlation equation for the Nusselt number that is adequate for modeling forced convection in metal foams within a limited range of pore Reynolds numbers.

Hwang et al. (2002) studied convective heat transfer and friction drag in a duct with aluminum foams experimentally. The combined effect of porosity and flow Reynolds number ($1900<Re<7800$) are examined to understand the heat transfer performance of porous mediums. Results show that both the friction factor and the volumetric heat transfer coefficient increase with decreasing the foam porosity at a fixed Reynolds number. Besides, the aluminum foam of φ =0.8 has the best thermal performance under the same pumping power constraint among the three aluminum foams investigated. At the end of the study, empirical correlations for pore Nusselt number are developed in terms of Reynolds number under various foam porosities.

Kurtbas and Celik (2009) performed an experimental study to investigate the heat transfer performance of the porous mediums with different PPI characteristics on natural and forced convection through the channel. The test section was filled with the porous medium completely. The top and bottom walls are heated with a uniform heat flux, and temperature values are measured using thermocouples along the center of the heated walls. The Reynolds number was varied from 600 to 33000 to determine heat transfer characteristics of porous medium for both laminar and turbulent flow. The average Nusselt number is determined by averaging the local Nusselt numbers based on the values obtained by thermocouples. Results showed that the average Nusselt number increases proportionally to the porosity and aspect ratio of the rectangular

channel cross-section. Researchers also noted that the average Nusselt number increases rapidly until a critical value of the Reynolds number. After the critic Reynolds numbers, Nusselt number slowly decreases.

Ejlali et al. (2009) investigated fluid flow and heat transfer behavior of porous medium under laminar flow regimes for the high heat load removal system. Open-source and commercial numerical solvers were used to solve momentum and energy equations. The effects of porosity, PPI values, thermal dispersion, and local thermal non-equilibrium model constants were examined for different Reynolds numbers between 600 and 1000. At the end of the study, the heat transfer coefficients of porous mediums and conventional fin-array structures were compared. Results showed that heat removal using porous mediums could be increased by around 50% compared to the traditional methods for air-flow cooling systems.

Mancin et al. (2011) conducted an experimental study to examine the effects of heat transfer performance and characteristic properties on the pressure drop of porous mediums with different pore diameters and pore densities. The experimental heat transfer coefficients and pressure drops were measured at different Reynolds numbers and heat fluxes. The heat transfer coefficient was calculated with a method that takes into account foam-finned surface efficiency, fluid temperatures at the inlet and outlet of the test section, and heated plate wall temperatures. Calculations showed that the Nusselt number increases proportional to the Reynolds number, and applied heat flux to the wall does not affect the Nusselt number. Researchers also point out that high-pressure drops between the inlet and outlet should be considered when they are used for thermal management applications.

Bhattacharya and Mahajan (2002) conducted an experimental study investigating electronic cooling applications using porous mediums. Porous mediums were stacked inside the conventional fin structure to increase the heat transfer from the heat sink to the environment. All heat sinks were produced on-site, then porous mediums were placed without any conductive material. The forced convection results demonstrate that adding fins to metal foam considerably improves heat transfer. The heat transfer coefficient also increases with adding more fins due to increased heat transfer surface area. On the other hand, enhancement on heat transfer expenses of increased pressure drop. Researchers pointed out that the performance of porous mediums placed inside the fin-array structure was superior compared to the conventional fin-array structures. An empirical Nusselt number correlation was also

proposed for similar heat transfer problems in terms of Peclet number and pore diameter.

As seen from the literature survey, researchers focus on examining the heat transfer performance of porous mediums and obtain Nusselt number correlations for specific conditions such as constant geometric sizes or limited Reynolds number ranges. A summary table consisting of different correlation equations proposed by different researchers are given in Table 2.1.

As seen in Table 2.1, the Nusselt number correlations found in the literature are defined as a function of limited parameters and are valid for the limited range of these parameters. In this study, the effects of porosity, pore density, geometric parameters and Reynolds number on the heat transfer characteristics of porous mediums will be investigated in a wider range, both experimentally and numerically. In the present thesis study, a square heat dissipating block representing an electronic component placed on the bottom wall of a channel is considered. A porous layer is placed at the top surface of the heat dissipating block. The flow and heat transfer characteristics in the porous layer are investigated experimentally and numerically under different flow and porous material properties. The results obtained by the numerical and experimental studies are used as input data for the neural network study and for developing a correlation equation for Nusselt number. Thus, an ANN tool and a correlation equation are obtained for the Nusselt number, which are based on flow Reynolds number, porous material properties, and geometric parameters contrary to the proposed equations in the literature.

Table 2.1 *:* Summary of Nusselt Number correlations developed by different researchers for forced convection heat transfer through a porous medium

Researcher	Material	PPI	Case	Correlation Equation
Tzeng and Jeng (2006)	Al Foam	10 - 40	90-deg turned air flow in a fully filled channel	$Nu = 21.1Re^{0.457}$
Leong and Jin (2005)	Al Foam	40	Oscillating air flow in a fully filled channel	$Nu = 12.3A_0^{0.95}Re^{0.31}$
Hsieh et al. (2004)	Al Foam	20-40	Air flow in a fully filled channel	$Nu = 0.44\ Re_{Dp}^{0.44}$ for 20PPI $Nu = 0.63Re_{Dp}^{0.46}$ for 40 PPI
Tzeng, (2007)	Al Foam	10	Air flow in a fully filled channel	$Nu = 4.385Re^{0.52}$
Noh et al. (2006)	Al Foam	10	Air flow in a fully filled channel	$Nu = 23.1Re^{0.4}Pr^{-0.1}Da^{0.09}$
Calmidi and Mahajan (1999)	Al Foam	5-10-20-40	Air flow in a fully filled channel	$Nu = 0.52\left(\frac{Re}{\varphi H}\right)^{0.5} Pr^{0.37}$

Table 2.1 Continue

Researcher	Material	PPI	Case	Correlation Equation
Kakac et al. (1987)	Copper or Steel Alloy	10-20-30-60	Air flow in a fully filled pipe	$Nu = 0.76Re^{0.4}Pr^{0.37} \quad 1 \leq Re \leq 4$ $Nu = 0.52Re^{0.5}Pr^{0.37} \quad 4 \leq Re \leq 10^3$ $Nu = 0.26Re^{0.6}Pr^{0.37} \quad 10^3 \leq Re \leq 2x10^5$
Hwang et al. (1995)	Sintered Bronze Beads	None	Air flow in a fully filled channel	$Nu = 0.081(1-\varphi)\varphi^2 Re_{Dp}^{1.35} Pr^{0.33}\left(\frac{D_p}{d_b}\right)^{0.35} \quad for\ Re_{Dp} \leq 75$ $Nu = 21.65(1-\varphi)\varphi^2 Re_{Dp}^{0.59} Pr^{0.33}\left(\frac{D_p}{d_b}\right)^{0.35} \quad for\ Re_{Dp} \leq 350$
Hamadouche et al. (2016)	Al Foam	40	Air flow in a fully filled channel	$Nu = 0.0117Re^{0.64}$
Ichimiya (1999)	Ceramic Foam	20	Air flow in a fully filled channel	$Nu = 2.43Re_{Dp}^{0.4} \quad 65 \leq Re \leq 457$
Hwang et al. (2002)	Al Foam	10	Air flow in a fully filled channel	$Nu = 0.32Re^{0.6} \quad 1900 \leq Re < 7800$

Re : Reynolds Number based on Channel Hydraulic Diameter (m) Pr: Prandtl Number A_0: Amplitude
Re_{Dp} : Reynolds Number based on Porous Diameter (m) D_p : Pore Diameter (m) φ : Porosity
H: Channel Height (m) d_b : Bead Diameter (m) Da: Darcy Number

CHAPTER III
EXPERIMENTAL STUDY

Within the scope of this thesis, considering that the heat-dissipating brass block, which represents the electronic element, is placed in a horizontal channel in order to investigate the heat transfer characteristics of porous mediums as electronic cooling attachments. For this purpose, an experimental setup was constructed. The effects of the Reynolds number of the flow in the channel and heat generation rate on the heat transfer from the block were investigated. In this chapter, the experimental setup and data analysis procedure are explained in detail.

3.1 EXPERIMENTAL SETUP

The experimental setup comprises a rectangular cross sectioned channel, a heat emitting block representing the electronic component, a porous medium placed on the block surface, thermocouples, a 12 V power supply, a datalogger, a thermal anemometer, and a fan. A schematic view of the experimental setup is shown in Fig. 3.1. A photograph of the test set up built is shown in Fig. 3.2. The porous medium with known thermophysical and pore characteristics was provided by TUBITAK-MAM. The block representing the electronic component is composed of two brass plates with a resistance heater (resistance wire) placed between them and four thermocouples placed in the brass plate. The power is supply to the resistance heater through 12 V power supply device. The temperature of the brass block was measured using four thermocouples, which are also placed in the block. The temperature data is transmitted to a computer via a datalogger, processed and stored using Elimko commercial software. The fan operates in the pressurized mode, and a frequency inverter is used to control the fan speed, and hence the air flow rate in the channel. The flow velocity inside the channel is measured and collected at 1 Hz rate by a hot wire thermal anemometer.

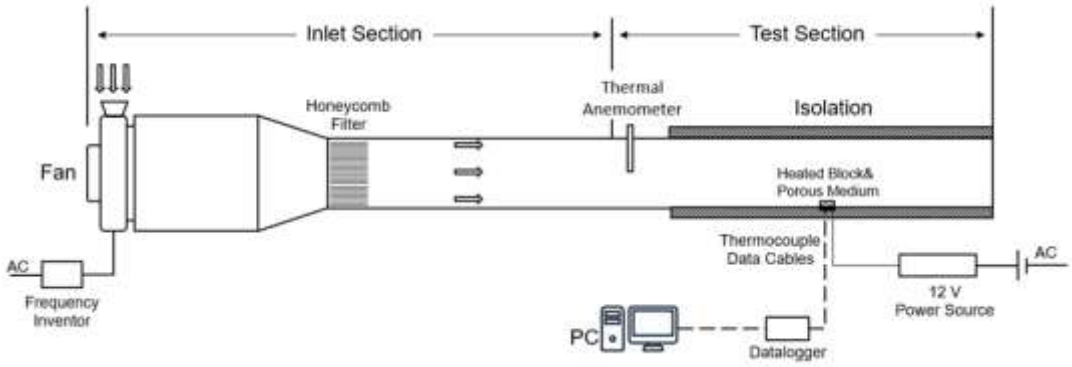

Figure 3.1: Schematic view of the experiment assembly.

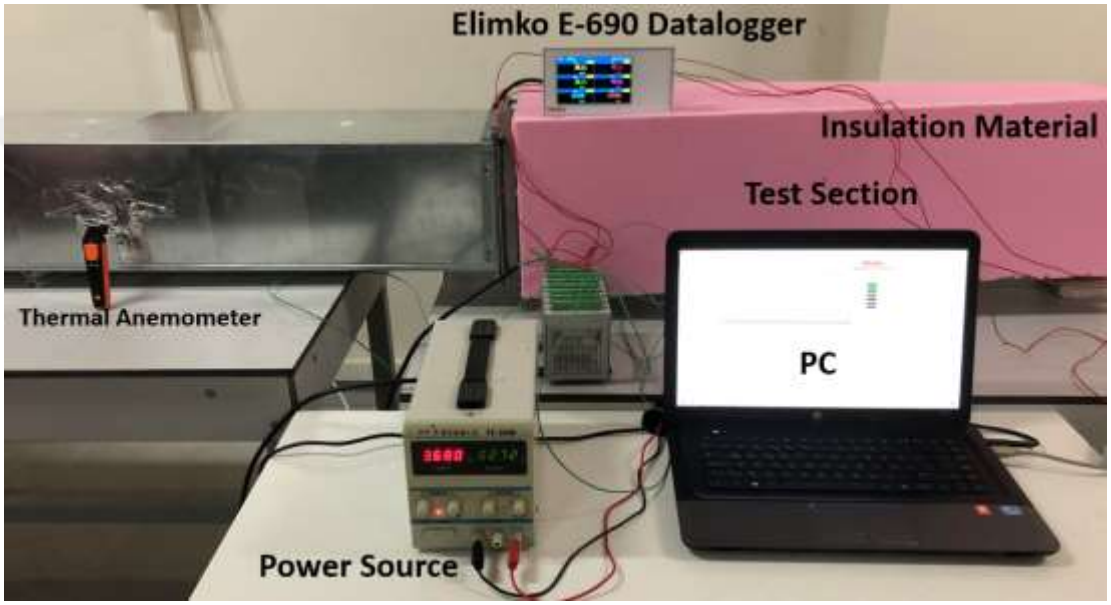

Figure 3.2: A photograph of the experimental setup.

The photograph and details of the test system are explained below by dividing it into two sections as inlet and test sections as shown in Fig. 3.1.

3.1.1 Inlet Section

The inlet section consists of a converging duct, and a constant cross-sectioned rectangular channel. A honeycomb is placed at the inlet of the rectangular channel. An axial fan is mounted at the inlet. The motor is powered through a frequency inverter to control the fan speed, and hence the air flow rate. The air supplied by the fan enters the converging duct, then reaches the honeycomb. The purpose of the honeycomb is to minimize the swirl and eddies as air enters the test section. The honeycomb is 200×250 mm in size and 30 mm in thickness, and it is made of aluminum. The honeycomb used in the experimental setup is shown in Fig. 3.3.

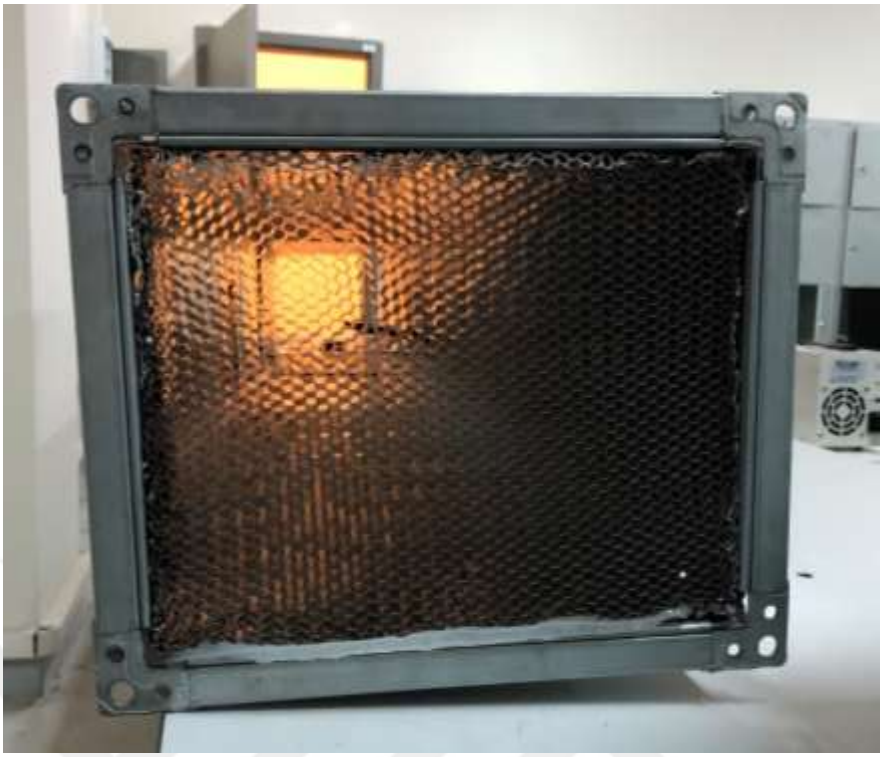

Figure 3.3: Honeycomb used in the experimental setup.

3.1.2 Test Section

The air passing through the honeycomb reaches the test section. This section consists an insulated rectangular channel, the heated block placed at bottom wall, a porous layer placed on the heated block top surface, thermocouples, and a thermal anemometer. The test section cross-section is 200×250 mm and has a length of 1200 mm. The bottom wall of the channel is made of 10 mm thick heat-resistant plexiglass. The side and top walls of the channel are manufactured from 1 mm thick steel sheet.

The dimensions of the heated block were determined as 40×40 mm by considering the dimensions of a GPU of an actual graphic card. The heated block is made of two pieces 6 mm thick brass blocks placed one on top of the other. One of the pieces was machined to form mini channels for housing the resistance wire, as shown in Fig. 3.4. The total length of the mini channel in the block is 672 mm, and the channel width and the depth are 1 mm. Four holes of 3 mm diameter were drilled at the corners to colligate brass pieces using bolts and nuts after placing the resistance heater and the thermocouples in places.

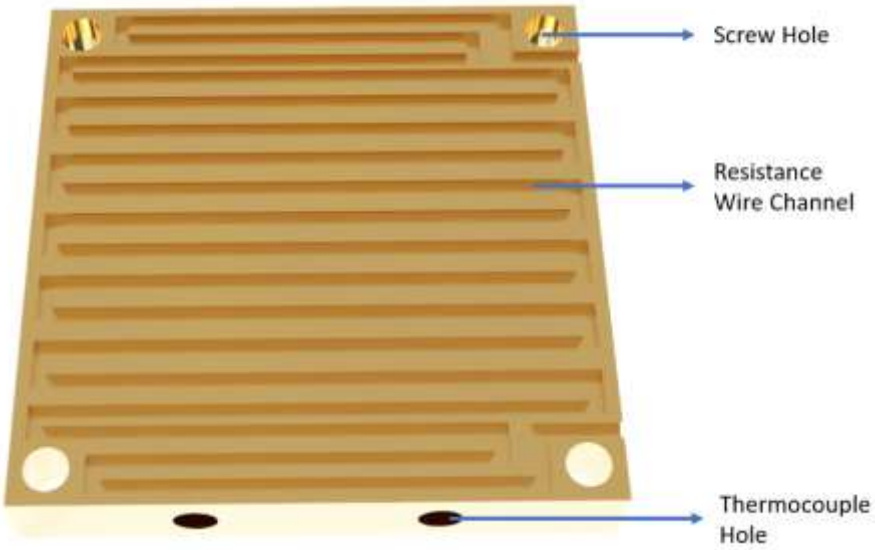

Figure 3.4: Mini channel machined brass plate for housing the resistance wire.

Four cylindrical slots with 3 mm diameter and 12 mm depth were drilled from two opposite sides of the brass plate into the plate to place four thermocouples at four different points inside plate. In a transparent view, the housings for the thermocouples are shown in Fig 3.5.

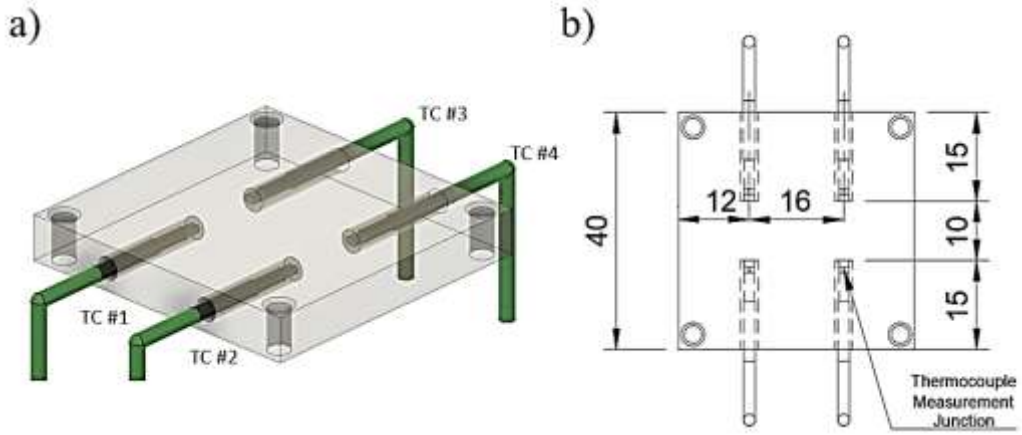

Figure 3.5: CAD drawing of slots in the brass plate to place the thermocouples a) CAD view and b) drawing with dimensions.

The second piece was used as a bottom cap to keep the resistance wire inside the heated block. An acrylic coating spray is applied to provide electrical insulation between the brass blocks and the resistance wire. A 0.5 mm resistance wire is placed inside the channel, as shown in Fig. 3.6. The resistance of the resistance wire is

1.95×10^{-3} ohms/mm. Exploded CAD geometry of the heat generating block assemly is shown in Fig. 3.7.

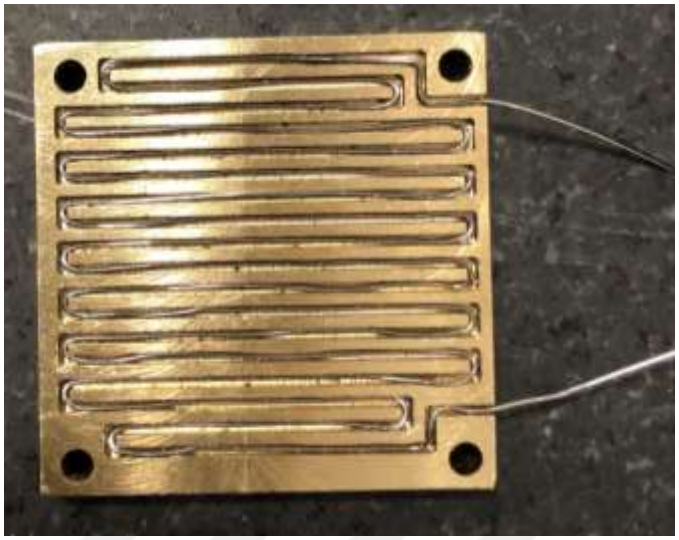

Figure 3.6: The resistance wire placed inside the channel.

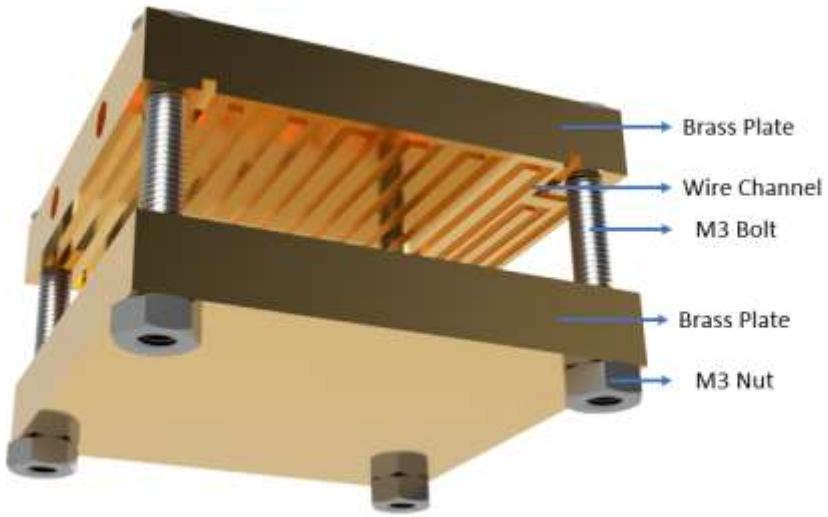

Figure 3.7: Exploded CAD model of the heat generating block representing an electronic component.

After the resistance wire is placed into the channels, the brass plates are joined using bolt-nut pairs. Then, the assembled block is fixed on a metal sheet placing an insulating material between the bottom brass block and sheet metal as shown in Fig. 3.8. The thermal conductivity of insulation material is 0.039 W/mK. After fixing the brass block on the sheet metal, the thermocouples are inserted into the slots in the upper block as shown in Fig. 3.8a.

a)

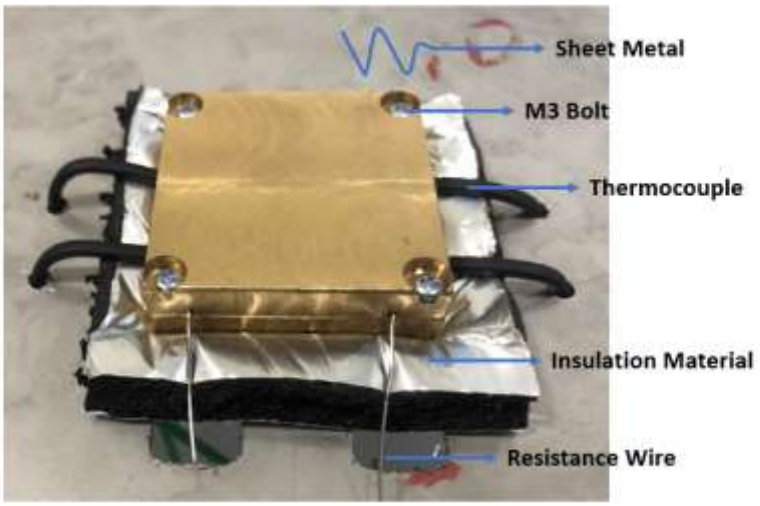

b)

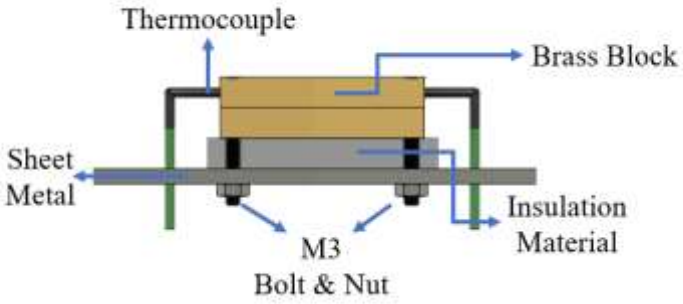

Figure 3.8: Installation of the brass block on sheet metal, a) implementation of the brass block, and b) CAD drawing.

Then, the assembly is placed on the plexiglass bottom wall of the test channel such a way that the top surface of the block is flush with the plexiglass plate. To place the block assemble on the plexiglass plate, a square place in the size of the block is machined in the plexiglass plate and the block is fixed there using the spring mechanism shown in Fig. 3.9. The springs, which are concentric with the bolts at the corners of the plexiglass wall, are placed between the plexiglass plate and a sheet metal. As the bolts are screwed, the distance between the plexiglass and the sheet metal is adjusted to the desired position.

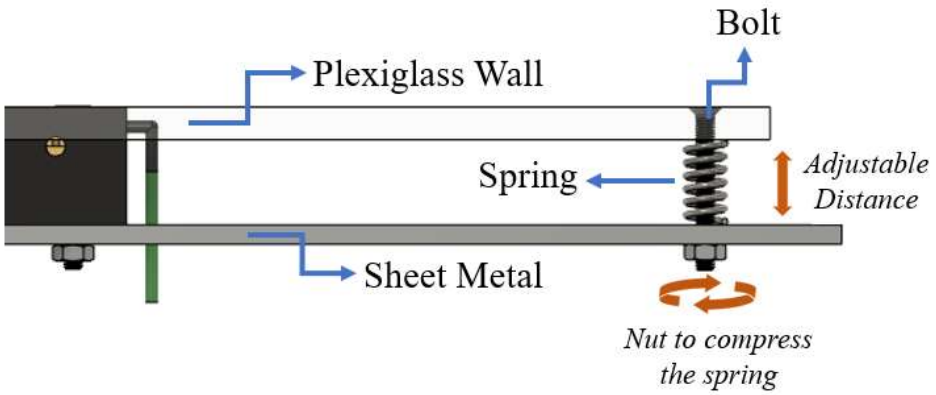

Figure 3.9: The spring mechanism used to change the distance between the plexiglass wall and the sheet metal.

As shown in Figure 3.10, the block assembly is positioned within the plexiglass plate forming the bottom wall of the test channel. An insulation material is placed around the block, between the block side surfaces and the plexiglass side surfaces. Then, the porous layer is mounted on the top surface of the block. To mount the porous layer on the block, Thermalright TF7 thermal compound paste with high conductivity is used. The material conductivity and the maximum exposure temperature of the thermal paste are 12.8 W/mK and 250℃, respectively. The porous medium used as a cooling attachment has an average pore diameter of 4 mm and porosity of 95% and is made of aluminum. The exploded CAD model of the brass block assembly is given in Fig. 3.11.

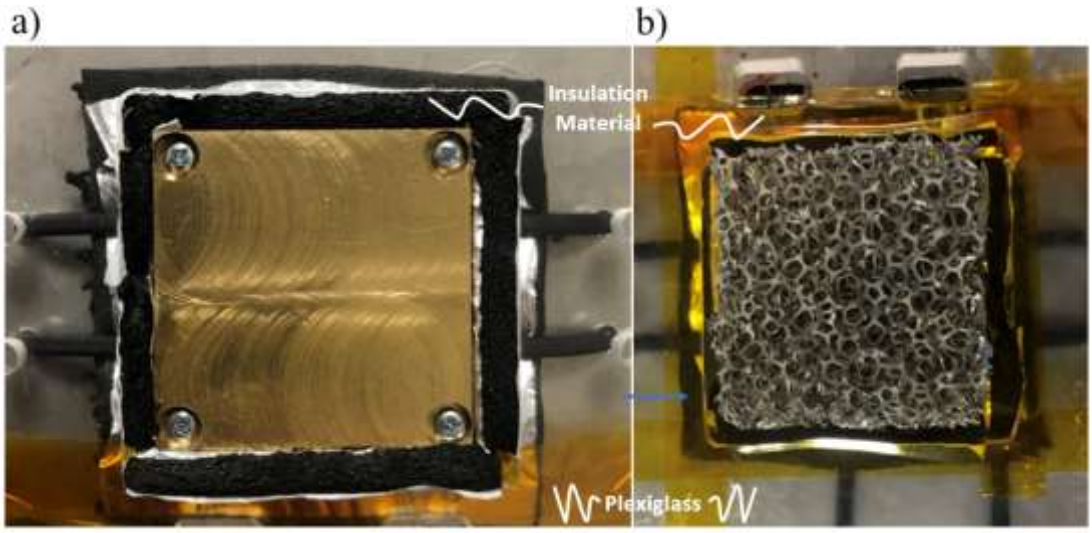

Figure 3.10: The block assembly mounted within the plexiglass plate, a) before porous layer is mounted, and b) after porous layer is mounted.

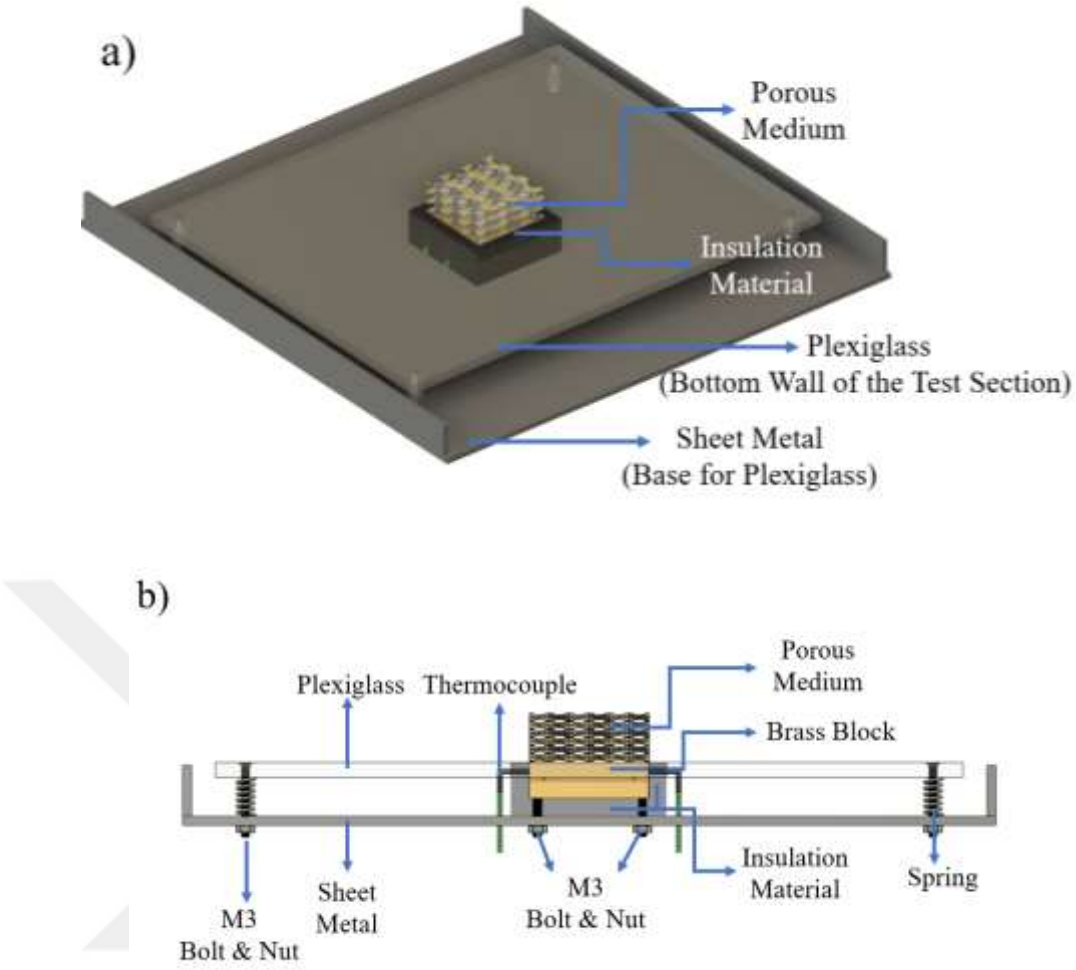

Figure 3.11: CAD images of brass block assembly representing the electronic component, a) assembled view and b) side view.

After mounting the block assembly on the bottom wall of the test section, the thermocouples and power cables are connected to the data logger and power source. Aluminum tape is used to prevent air leakage between the plexiglass and the sheet metal part of the channel. An image of the test section taken through the channel is shown in Figure 3.12.

Figure 3.12: A photograph of the test section

3.1.3 Devices used in the Experimental Setup

The main devices and their functions in the experimental setup are explained below.

3.1.3.1 Fan

A BVN BDTX-B circular axial duct fan is used to pressurize air to the rectangular channel. The fan can supply 2610 m^3/h air at the maximum impeller speed of 2610 rpm.

3.1.3.2 Frequency Inverter

A frequency inverter, also known as a variable frequency drive (VFD), is a device that is commonly used to control the speed of an electric motor. A frequency inverter is used to adjust the speed of the motor that drives the fan blades. The main advantage of using a frequency inverter to control the speed of the fan is that it allows for precise control over the airflow rate, which is important for achieving optimal ventilation and air quality in the space. By varying the frequency of the electric currentd supplied to the motor, the speed of the fan can be adjusted to meet the specific requirements of the application. In this thesis study, Yılmaz YA2000 Series 7.5 kW frequency inventor is used to achieve the desired Reynolds number (air velocity) within the channel.

3.1.3.3 Thermal Anemometer

Testo 405i Smart Thermal Anemometer is used to measure air velocity. The thermal anemometer can collect air velocity data at 1 Hz rate, and the readings are transmitted wirelessly to the computer. The resolution of the thermal anemometer is ± 0.01 m/s. The telescopic tube allows the measurement to be made exactly at the desired point inside the channel to determine the Reynolds number precisely. The probe on the telescopic tube was placed in the channel just before the inlet of the test section during the experiments.

3.1.3.4 Power Supplier

To supply the desired electrical power to the resistance heater in the block assembly, the power supplier of brand TT Technic PS-300SD is used. The power supplier can supply 18V voltage output with a sensitivity of 0.01 V. By connecting the positive and negative poles of the device directly to the resistance wire, voltage is applied to the resistance wire. In order to determine the heat generation in each experiment, voltage values were manually adjusted from the power supplier. power supply device allows adjusting voltage or current values during experiments.

3.1.3.5 Thermocouple

K-type thermocouples were used in order to measure the temperature in block assembly, insulation material surface temperature, the environmental temperature, and air inlet temperature. The temperature measurement range of the K-type thermocouples is −200 °C to +1350 °C. The K-type thermocouples consists of nickel-chromium and nickel-alumel conductors. These two dissimilar conductors are joined using a resistance welding machine (spot welder). The welded point is called the measurement junction. In this study, the measurement junction is covered by thermal paste which has a thermal conductivity of 12.8 W/mK, and placed into the slots in the the brass plate. To determine the surface temperatures of the insulation material, thermocouples were directly attached to the surfaces with heat-resistant tape. The thermocouple used in this study is shown in Fig 3.13.

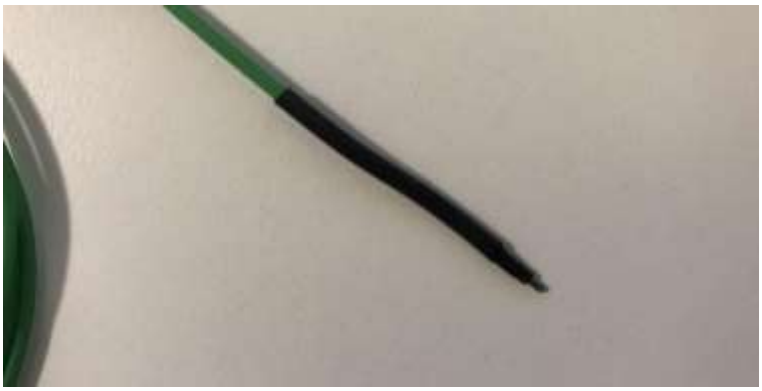

Figure 3.13: K-type thermocouple used in this study

3.1.3.6 Datalogger

Elimko E-690 Series universal datalogger was used to collect temperature data during the experiments. Its high sampling rate of 200 milliseconds per channel, which allows for fast and accurate data collection. Datalogger has a variety of communication options, including Ethernet and RS485, allowing it to easily interface with a computer for data transfer and analysis. The Ethernet interface allows the datalogger to be connected to a local area network (LAN), providing a way to transfer data to a PC. The RS485 interface, on the other hand, is a serial communication protocol that allows the datalogger to communicate with other devices, such as sensors or controllers, over long distances. The E-690 datalogger collected temperature values from twelve channels for multiple location measurements simultaneously. The

3.1.3.7 Elimko Software

Elimko software was used to transfer, store and analyze the temperature data collected in the datalogger. The software has the ability to label and graph temperature data for each experiment.

3.2 EXPERIMENTAL PROCEDURE

Experimental studies were conducted to examine the effect of porous material on cooling of an electronic component using the experimental setup described above. The experimental study was performed following the procedure described below:

1. The fan is turned on.
2. The thermal anemometer is turned on and verified if it monitors and records instantaneous air velocity values.

2. Using the frequency inverter, the fan speed is adjusted so that the prescribed air speed in the channel and hence the desired Reynolds number is obtained.
3. The data logger and the computer are turned on, and the data analysis Elimko program is controlled if the temperature data is transferred to the computer and stored.
4. The power supply is turned on and set the desired voltage values.
5. Whole system is run until all measured temperature values reach steady state conditions.
6. When all the measured values reach the steady state conditions, instantaneous temperature values are recorded on the computer via the Elimko program.
7. Air velocity values stored on thermal anemometer are transferred to the computer via a wireless connection.
8. The experiment is terminated, and all instruments are turned off.

3.3 ANALYSIS OF EXPERIMENTAL DATA

The main objectives of the experimental study are to determine the temperature of the block representing an electronic component and the Nusselt number from the porous layer mounted block to the air flowing in the channel with different Reynolds numbers and the heat generation rate conditions. For these objectives, the experiments were performed at different Reynolds numbers and heat generations. For all the experiments, the same porous layer was used.

During the experiments, the temperature at four different points inside the heated block, the air temperature at the test section inlet, the internal and external surface temperatures of the insulation material covering the bottom and side surfaces of the block, and the ambient temperature were measured. In addition, instantaneous air velocity was measured using a thermal anemometer, and the voltage and current values of the heater were measured. From these measured data, the Reynolds number was calculated using the air velocity and channel hydraulic diameter. The average Nusselt number was calculated using power supplied to the block, heat loss to the ambient was calculated. The details of the data analysis are given below:

3.3.1.1 Reynolds Number

Reynolds number is calculated based on the hydraulic diameter D_h of the channel as

$$Re = \frac{\rho V D_h}{\mu} \tag{3.1}$$

where ρ represents the density of the air, V represents the air velocity, D_h is the hydraulic diameter of the channel and μ is the dynamic viscosity of the fluid. The hydraulic diameter of the channel is calculated as

$$D_h = \frac{4A_c}{P} = \frac{4(w \times H)}{2(w + H)} \tag{3.2}$$

where, A_c represents the cross-sectional area of the channel, P represents the perimeter of the channel and w and H are the width and height of the test section.

3.3.1.2 Average Nusselt Number

In order to calculate the Nusselt number, it is necessary to determine the heat transferred to the air by convection from the block through the porous material. The general definition of the Nusselt number is as follows;

$$Nu = \frac{hL_c}{k_f} \tag{3.3}$$

where h is the heat transfer coefficient, k_f is the conductivity of the air, and L_c is the characteristic length. In this study, using the channel hydraulic diameter (D_h) and porous medium height as the characteristic length, the two different Nusselt numbers were calculated. Because, especially in cases where the effect of channel height is studied, the effect of hydraulic diameter on Nusselt number is dominant compared to the heat transfer coefficient. Therefore, the Nusselt number based on the height of the porous medium (Nu*) has also been calculated for each case.

To determine the average The heat transfer coefficient from the block, the heat transferred by convection to the air flowing in the channel can be expressed as

$$Q_{conv} = h\, A\, (\overline{T_p} - T_i) \tag{3.4}$$

where Q_{conv} is the surface-to-air heat transfer by convection, h is the average heat transfer coefficient, A is the brass block heat transfer surface area (top surface area), $\overline{T_p}$ is the average block temperature which is calculated as the arithmetic average of temperatures measured from four different ponts in the block, T_i is the air inlet temperature measured at the entrance of the test section.

The average heat transfer coefficient, h, can be solved from the above equation as;

$$h = \frac{Q_{conv}}{A(\overline{T_p} - T_i)} = \frac{q''}{(\overline{T_p} - T_i)} \tag{3.5}$$

where q'' is surface heat flux ($q''=Q_{conv}/A$) . Substituting Eq. (3.5), into Eq. (3.4), the following equation is obtained for the Nusselt number.

$$Nu = \frac{Q_{conv}}{A(\overline{T_p} - T_i)}\frac{D_h}{k_f} = \frac{q''}{(\overline{T_p} - T_i)}\frac{D_h}{k_f} \tag{3.6}$$

In Eq. (3.6), the values of all the variables are measured directly or can be calculated from the measured data.

In order to determine the heat flux, the total amount of heat transferred from the block through the porous material to the fluid needs to be calculated. For this purpose, assuming that whole electrical power supplied to the resistance heater is converted into heat, the energy balance for the system can be written as,

$$Q_{conv} = Q_e - \Delta Q \tag{3.7}$$

where, Q_{conv} represents the total amount of heat transferred from the block surface to the fluid, Q_e is the total amount of electrical power (heat) supplied to the resistance wire, and the ΔQ is the total heat loss from the system by conduction and radiation.

The total power supplied to the resistance heater in the block can be calculated as,

$$Q_e = I\,V \tag{3.8}$$

Here, V indicates the voltage applied to the resistance wire, and I denotes the current. The total heat losses by conduction and radiation from the system can be expressed as;

$$\Delta Q = \Delta Q_{cond} + \Delta Q_{rad} \tag{3.9}$$

where, ΔQ_{cond} and ΔQ_{rad} refer to the heat loss by conduction and radiation, respectively. Heat loss by conduction through the insulating material surrounding the heated brass block, can be calculated as heat passing as follows;

$$\Delta Q_{cond} = k_{ins} A_{insulation} \frac{\Delta T}{\Delta x} \tag{3.10}$$

Here, k_{ins} refers to the heat conduction coefficient of the insulating material used in the experimental assembly, $A_{insulation}$ refers to the block surface in contact with the insulation material, Δx refers to the thickness of the insulation, and ΔT refers to the temperature difference measured at the inner and outer surface of the insulation. The heat loss caused by radiation was calculated by taking 0.5% of the total heat generation in accordance with the studies in the literature (Adhikari *et al.*, 2020).

3.4 FILTERING VELOCITY DATA COLLECTED BY THERMAL ANEMOMETER

The air velocity was measured utilizing the thermal anemometer in the experimental setup. During air velocity measurements, 1 Hz of velocity data is collected and transmitted via Bluetooth to the computer. As seen in Fig. 3.14, it was discovered that the velocity values fluctuate within a specific range. This may be caused by small fluctuations in flow velocity and/or electronic noise.

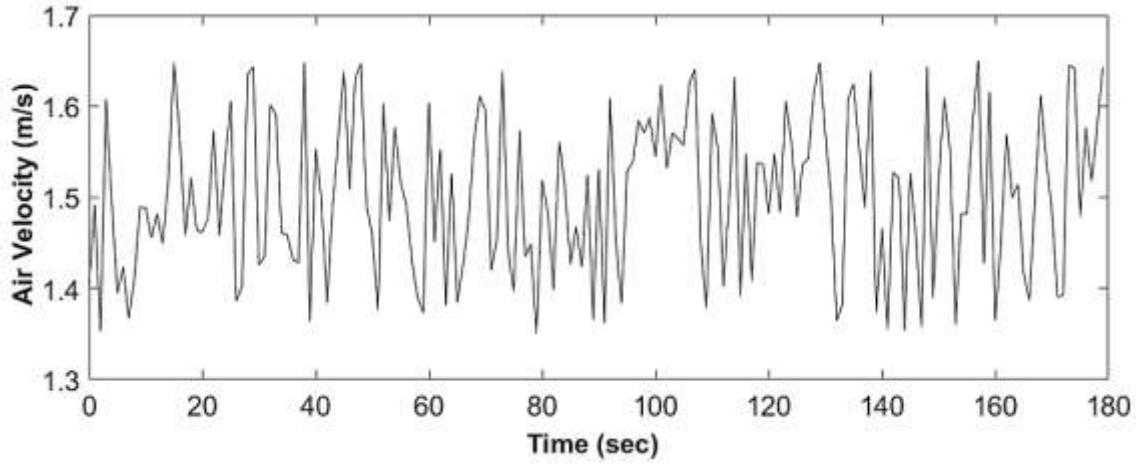

Figure 3.14: Measured instantaneous air velocity values for period of 180 seconds.

To obtain the instantaneous filtered air velocity, the raw velocity data was filtered using the following expression (Turkoglu, 1990):

$$y_n = c\, x_n + (1 - c) y_{n-1} \tag{3.11}$$

where, y_n represents the filtered value, x_n represents the measured raw value from the thermal anemometer, y_{n-1} represents the filtered data at previous instant, and c represents the filtering coefficient. Figure 3.15 shows the unfiltered (raw) and filtered velocity values obtained using two different filtering coefficients. In this study, velocity values were filtered using the filtering coefficient of c=0.01.

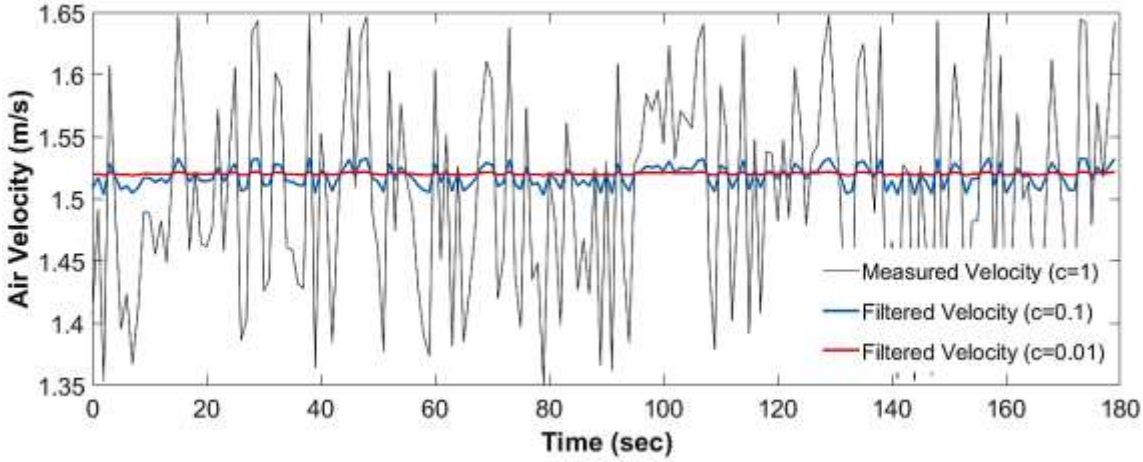

Figure 3.15: Sample unfiltered and filtered velocity values for a period of 180 seconds.

3.5 REPEATABILITY ANALYSIS OF EXPERIMENTAL DATA

To check the repeatability of the experimental data measured, the experiments were performed on three different days at the same thermal and flow conditions, and the results were compared. In these experiments, the Reynolds number was kept constant at 27370, and the electrical power was 18.28 W. The temperature data obtained from Thermocouple#1 and the ambient temperature were compared in Fig. 3.16.

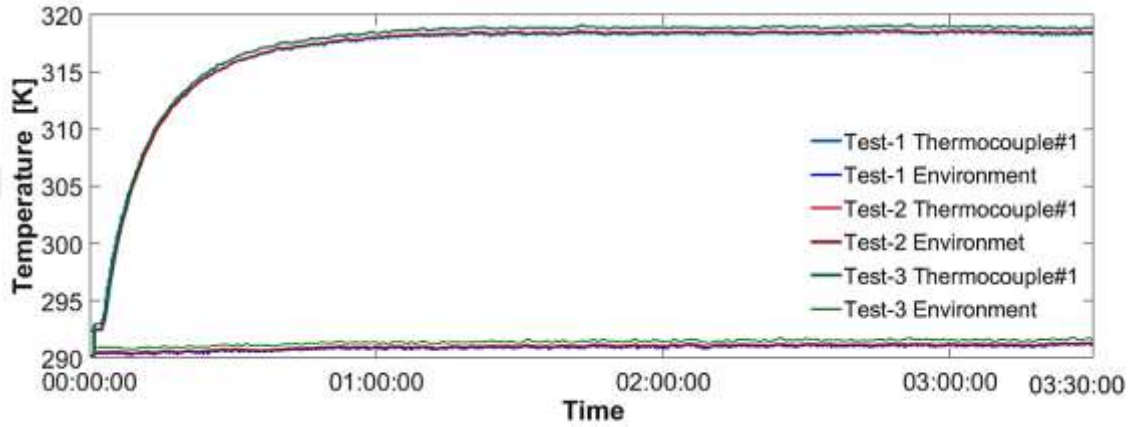

Figure 3.16: Comparison of temperature data obtained from Thermocouple#1 and ambient temperature on three different days.

Figure 3.16 shows that the temperature values obtained from thermocouple #1 on three different days are quite close in Test-1 and Test-2, but the temperature measured by Test-3 is 1.7 K higher. The reason for this difference may due to the difference between the ambient temperature when the tests were carried out. The ambient temperature measured at the time of Test-3 was approximately 2 K higher than the ambient temperature measured on the days of Test-1 and Test-2. As a result, it was observed that the experimental setup yields repeatable results.

3.6 ERROR ANALYSIS

Various errors may occur in the measurement phase of the data obtained by an experimental setup. Therefore, the results may not be compatible with theoretical predictions or other experiments in the literature. In the calculation of value of a measured parameter, a total error calculation should be made by taking into account the errors of the measuring devices used in the experimental setup and also the user

errors. For error analysis in this study, the method proposed by (Holman, 1971) was used.

If a parameter R (it is a dependent variable) is calculated from experimental data $x_1, x_2, \ldots, x_n$, (these are independent variables affecting the dependent variable R), the functional relation can be written as follows:

$$R = R(x_1, x_2, \ldots, x_n) \tag{3.12}$$

The total error contained in parameter R can be found in terms of the error contained in each argument with the following equation:

$$W_R = \left[\left(\frac{\partial R}{\partial x_1} W_1\right)^2 + \left(\frac{\partial R}{\partial x_2} W_2\right)^2 + \cdots + \left(\frac{\partial R}{\partial x_n} W_n\right)^2\right]^{1/2} \tag{3.13}$$

where, W_R represents the amount of total error of the dependent variable and W_1, W_2 and ...W_n represents the amount of error in the independent variables.

Following this approach, an error analysis can be performed for Nusselt number calculated using the measured data. The Nusselt number is calculated from formula given in Eq. (3.14).

$$Nu = \frac{q''}{A\left(\overline{T_p} - T_i\right)} \frac{D_h}{k_f} \tag{3.14}$$

In Equation 3.14, the dependent variable is the Nusselt number, and the independent variables are heat flux (q''), hydraulic diameter (D_h), heat conduction coefficient (k_f) and temperature difference ($\overline{T_p} - T_i$). In order to determine the total error that occurred in the Nusselt number, it is necessary to calculate the errors for each of these independent variables separately. The equation that gives the total amount of error (W_{Nu}) for the Nusselt number can be written as follows:

$$W_{Nu} = \left[\left(\frac{\partial Nu}{\partial q''} W_{q''}\right)^2 + \left(\frac{\partial Nu}{\partial D_h} W_{D_h}\right)^2 + \left(\frac{\partial Nu}{\partial k_f} W_{k_f}\right)^2 + \left(\frac{\partial Nu}{\partial (\overline{T_p} - T_i)} W_{(\overline{T_p} - T_i)}\right)^2\right]^{1/2} \tag{3.15}$$

Here, $W_{q''}$, W_{Dh}, W_k and $W_{\overline{T_p}-T_i}$ represent the errors in the heat flux, the channel hydraulic diameter, the conduction coefficient, and the temperature difference, respectively. The following equations are obtained by taking the derivatives of the above Eq. (3.14):

$$\frac{\partial Nu}{\partial q''} = \frac{D_h}{\left(\overline{T_p} - T_i\right)k_f} \tag{3.16}$$

$$\frac{\partial Nu}{\partial D_h} = \frac{q''}{\left(\overline{T_p} - T_i\right)k_f} \tag{3.17}$$

$$\frac{\partial Nu}{\partial k} = \frac{kD_h k_f^{-2}}{\left(\overline{T_p} - T_i\right)} \tag{3.18}$$

$$\frac{\partial Nu}{\partial\left(\overline{T_p} - T_i\right)} = \frac{q''D_h\left(\overline{T_p} - T_i\right)^{-2}}{k_F} \tag{3.19}$$

Substituting these expressions into Eq. (3.15), the total error in the Nusselt number is obtained as,

$$W_{Nu} = \left[\left(\frac{D_h}{\left(\overline{T_p} - T_i\right)k_f}W_{q''}\right)^2 + \left(\frac{q''}{\left(\overline{T_p} - T_i\right)k_f}W_{D_h}\right)^2 + \left(\frac{kD_h k^{-2}}{\left(\overline{T_p} - T_i\right)}W_{k_f}\right)^2 + \left(\frac{q''D_h\left(\overline{T_p} - T_i\right)^{-2}}{k_f}W_{\left(\overline{T_p}-T_i\right)}\right)^2\right]^{1/2} \tag{3.19}$$

Rearranging Eq. (3.19), the following equation is obtained:

$$\frac{W_{Nu}}{Nu} = \left[\left(\frac{W_{q''}}{q''}\right)^2 + \left(\frac{W_{D_h}}{D_h}\right)^2 + \left(\frac{W_{k_f}}{k_f}\right)^2 + \left(\frac{W_{\left(\overline{T_p}-T_i\right)}}{\left(\overline{T_p} - T_i\right)}\right)^2\right]^{1/2} \tag{3.20}$$

In order to determine the value of the error in the calculation of the Nusselt number, the errors in the variables on which the Nusselt number is dependent must be

calculated or estimated. The error rates for the relevant variables can be found as below.

The error in the temperature difference can be found as follows:

$$\frac{W_{(\overline{T_p}-T_i)}}{(\overline{T_p}-T_i)} = \left[\left(\frac{W_{\overline{T_p}}}{(\overline{T_p}-T_i)}\right)^2 + \left(\frac{W_{T_i}}{(\overline{T_p}-T_i)}\right)^2\right]^{1/2} \tag{3.21}$$

The heat conduction coefficient (k_f) value is taken directly from the catalog and the error is around 1%. The error in calculating the hydraulic diameter of the channel can be assumed as zero.

In order to determine the error in the convection heat flux (q''), it is necessary to determine the error of the other variables which heat flux (q'') is dependent on. For this purpose, the errors of the variables used in calculating the heat flux are given below.

Error in the calculation of the total amount of heat (Q_{conv}) transferred from the brass block can be determined as follows:

$$Q_{conv} = Q_e - (Q_{cond} + Q_{rad}) \tag{3.22}$$

$$\frac{W_{Q_{conv}}}{Q_{conv}} = \left[\left(\frac{W_{Q_e}}{Q_e}\right)^2 + \left(\frac{W_{Q_{cond}}}{Q_{cond}}\right)^2 + \left(\frac{W_{Q_{rad}}}{Q_{rad}}\right)^2\right]^{1/2} \tag{3.23}$$

Error in the calculation of the total amount of power (heat) supplied to heaters:

$$Q_e = P = V\,I \tag{3.24}$$

$$\frac{W_{Q_e}}{Q_e} = \left[\left(\frac{W_V}{V}\right)^2 + \left(\frac{W_I}{I}\right)^2\right]^{1/2} \tag{3.25}$$

And the error in the calculation of total heat loss (Q_i) by conduction:

$$Q_{cond} = k\,A\frac{\Delta T}{\Delta x} \tag{3.26}$$

$$\frac{W_{Q_i}}{Q_i} = \left[\left(\frac{W_k}{k}\right)^2 + \left(\frac{W_A}{A}\right)^2 + \left(\frac{W_{\Delta T}}{\Delta T}\right)^2 + \left(-\frac{W_{\Delta x}}{\Delta x}\right)^2\right]^{1/2} \tag{3.27}$$

The calculation of the total heat loss by radiation (Q_{rad}) was calculated from 0.5% of total heat generation. It has been accepted that the error made with this assumption is 5% (Mancin et al. 2012).

The error of the total amount of heat can be obtained with the help of the above equations. Furthermore, the error of the heat flux passing from the heater block to the fluid is expressed as follows.

$$q'' = \frac{Q_{conv}}{A} \tag{3.28}$$

$$\frac{W_{q''}}{q''} = \left[\left(\frac{W_{Q_{net}}}{Q_{net}}\right)^2 + \left(\frac{W_A}{A}\right)^2\right]^{1/2} \tag{3.29}$$

As a result of the calculations, the error in the temperature difference is obtained approximately 1%, the error in the total power supplied to the heaters is obtained approximately 1%, the error in the total heat loss by conduction is obtained approximately 1.5%, and the error in the total heat loss by radiation is taken as 5%. Similarly, the error in the heat flux is obtained approximately 3.5%. Therefore, it was determined that the error in the Nusselt numbers was determined approximately 6.7%.

CHAPTER IV
MATHEMATICAL FORMULATION

Within the scope of the study, in addition to the experimental study, a numerical study was also carried out. In this chapter, basic approaches used for modelling the flows in porous medium are summarized first. Then, the mathematical formulation used in this study is given. The governing equations and boundary conditions are derived, and the expressions used for the calculation of physical properties in porous medium are given.

4.1 GOVERNING EQUATIONS

As seen in Fig. 4.1, the problem domain consists of a free stream flow zone, a porous zone and a heat generating block (electronic element). The free stream zone (the region outside the porous medium and the heat generating block) consists of flow of air in the channel. In the porous medium, the fluid flows through the pores, and significant friction and heat transfer occur between the fluid and the porous material matrix. In the heated block, there is no fluid flow, and the heat transfer occurs only by conduction. Hence, the governing equations should represent the different physical phenomenon taking place in these three different zones. Thus, the governing equations of turbulent flow and heat transfer equations are modified to model the problem consisting of three different zones by only one set of equations.

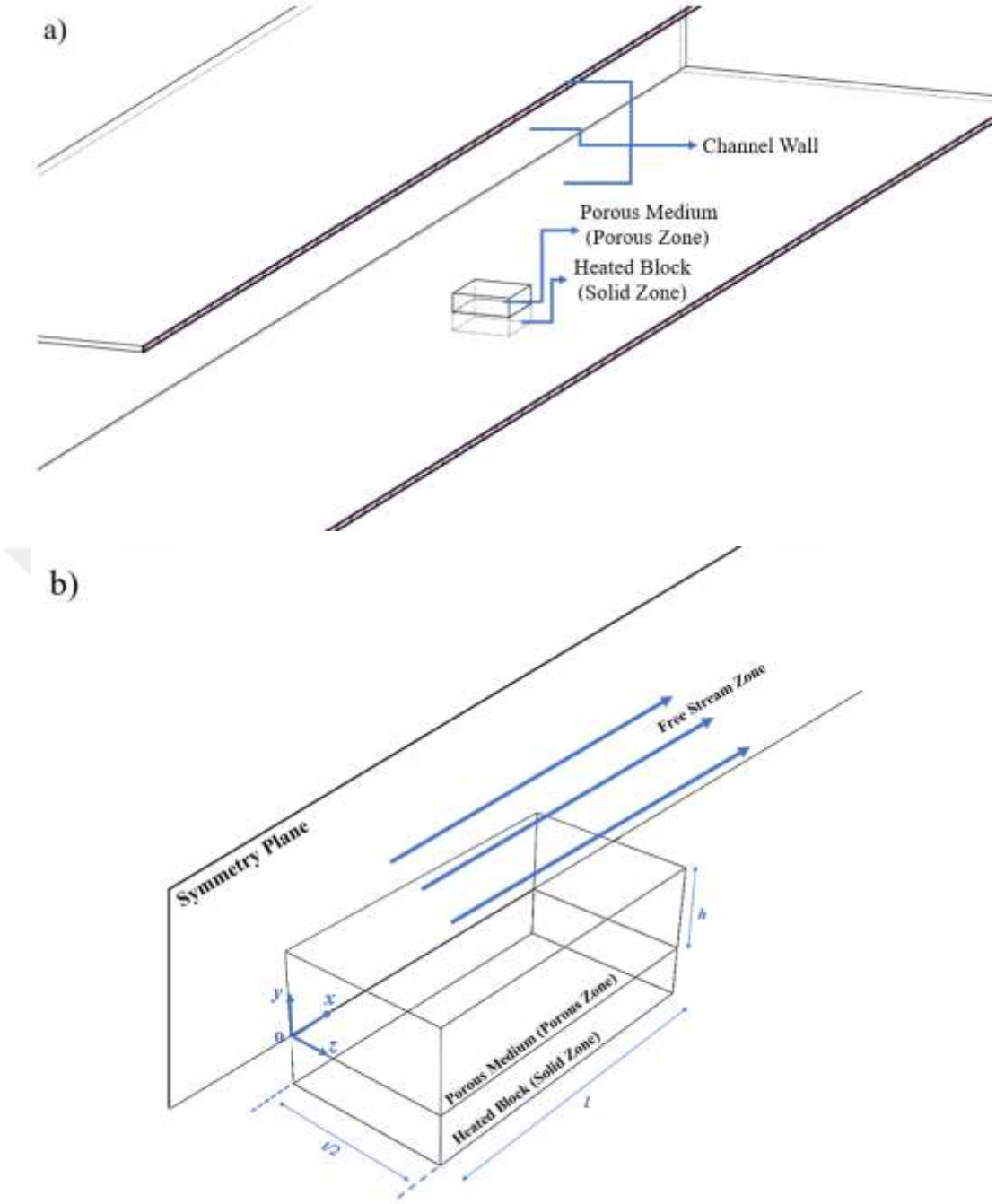

Figure 4.1: Schematic view of the problem domain, a) whole channel and b) computational domain which is half of the channel bounded by symmetry plane.

The problem under consideration is steady and flow is considered to be incompressible. In all the cases considered, the flow is turbulent. The Richardson number for the lowest Reynolds number case considered is calculated as 0.043 which is less than the critical Richardson number 0.1. Therefore, the buoyancy effects are neglected for all the cases considered. The radiation heat transfer is also considered to be negligible.

It is also assumed that fluid is Newtonian, and the thermophysical properties are constant. The solid matrix of the porous medium and the fluid are assumed to be in local thermal equilibrium (LTE) in the porous medium. The problem is three-dimensional, and the flow is symmetric with respect to the vertical plane passing through the middle of the porous layer parallel to the flow along the channel.

With the assumptions stated above, the equations governing the whole flow and temperature fields can be written using modified Reynolds Averaged Navier-Stokes equations (RANS) and modified energy equation for multizone domain consisting of free stream flow zone, porous zone and solid zone.

4.1.1 Continuity Equation

The continuity equation for three-dimensional, incompressible flow can be expressed as follows:

$$\frac{\partial u}{\partial x} + \frac{\partial v}{\partial y} + \frac{\partial w}{\partial z} = 0 \tag{4.1}$$

In this equation, *u*, *v*, and *w* are the velocity components in x-direction, y-direction, and z-direction, respectively.

4.1.2 Momentum Equations

Classical Reynolds Averaged Navier-Stokes equations are valid for free stream flow. For the porous region, the equations must incorporate terms and parameters that represent the effects of the porous medium on the flow and heat transfer. Representing the porous medium effects as source terms, the momentum equation in each coordinate direction can be written as follow:

$$\rho_f \left[\left(\frac{\partial}{\partial \mathrm{x}}(\mathrm{uu}) + \frac{\partial}{\partial \mathrm{y}}(\mathrm{uv}) + \frac{\partial}{\partial \mathrm{z}}(\mathrm{uw})\right)\right] = -\frac{\partial \mathrm{P}}{\partial \mathrm{x}} + \mu_{eff}\left(\frac{\partial^2 \mathrm{u}}{\partial \mathrm{x}^2} + \frac{\partial^2 \mathrm{u}}{\partial \mathrm{y}^2} + \frac{\partial^2 \mathrm{u}}{\partial \mathrm{z}^2}\right) + \delta S_x \tag{4.2}$$

$$\rho_f \left[\left(\frac{\partial}{\partial \mathrm{x}}(\mathrm{uv}) + \frac{\partial}{\partial \mathrm{y}}(\mathrm{vv}) + \frac{\partial}{\partial \mathrm{z}}(\mathrm{wv})\right)\right] = -\frac{\partial \mathrm{P}}{\partial \mathrm{y}} + \mu_{eff}\left(\frac{\partial^2 \mathrm{v}}{\partial \mathrm{x}^2} + \frac{\partial^2 \mathrm{v}}{\partial \mathrm{y}^2} + \frac{\partial^2 \mathrm{v}}{\partial \mathrm{z}^2}\right) + \delta \mathrm{S}_y \tag{4.3}$$

$$\rho_f \left[\left(\frac{\partial}{\partial \mathrm{x}}(\mathrm{uw}) + \frac{\partial}{\partial \mathrm{y}}(\mathrm{vw}) + \frac{\partial}{\partial \mathrm{z}}(\mathrm{ww})\right)\right] = -\frac{\partial \mathrm{P}}{\partial \mathrm{z}} + \mu_{eff}\left(\frac{\partial^2 \mathrm{w}}{\partial \mathrm{x}^2} + \frac{\partial^2 \mathrm{w}}{\partial \mathrm{y}^2} + \frac{\partial^2 \mathrm{w}}{\partial \mathrm{z}^2}\right) + \delta \mathrm{S}_z \tag{4.4}$$

In these equations, ρ_f is the density of the fluid, $\partial P/\partial x_i$ is the pressure gradient, S_x, S_y, and S_z are the source terms representing the porous medium effects on the flow in each coordinate direction. The source terms S_x, S_y, and S_z are multiplied by the constant δ which is zero for the free stream zone and 1 for the porous region. Hence, the source terms will be zero in the equations of the free stream zone, but it will remain in the equations for porous region.

The effect of the porous medium on the flow is calculated using Darcy-Forchheimer expressions as follow (Brinkman 1949, Ergun 1952, Forchheimer 1901)

$$S_x = -\left[\varphi\left(\frac{\mu u}{K}\right) + \varphi^2\left(C_E \frac{\rho|u|u}{K^{0.5}}\right)\right] \tag{4.5}$$

$$S_y = -\left[\varphi\left(\frac{\mu v}{K}\right) + \varphi^2\left(C_E \frac{\rho|v|v}{K^{0.5}}\right)\right] \tag{4.6}$$

$$S_z = -\left[\varphi\left(\frac{\mu w}{K}\right) + \varphi^2\left(C_E \frac{\rho|w|w}{K^{0.5}}\right)\right] \tag{4.7}$$

In these expressions, K is the permeability and φ is the porosity of the porous medium. The porosity φ is 1 in the free stream zone, and it is between zero and 1 in the porous region. The coefficient C_E can be expressed as follows:

$$C_E = \frac{1.75}{(150\varphi^3)^{0.5}} \tag{4.8}$$

In Eqs. 4.2-4.4, the effective viscosity of the fluid, μ_{eff}, is calculated as the sum of the laminar and turbulent viscosities:

$$\mu_{eff} = \mu_{lam} + \mu_t \tag{4.9}$$

The turbulence viscosity is calculated using k-ε turbulence model.

In this way, the momentum equation can be mathematically expressed with a single set of equations for both free stream and porous regions. The heat-emitting block is defined as solid, ensuring that the velocities in this region are zero, and hence only heat conduction takes place in it.

4.1.3 Energy Equation

In deriving the energy equation, it is assumed that the porous structure is homogeneous and isotropic. It is also assumed that the air and the skeleton of the porous medium is in local thermal equilibrium (LTE). Studies have shown that the LTE model gives consistent results in heat transfer analyses of porous structures (Akridiss Abed et al. 2020, Alomar et al. 2015, Settar et al. 2018). Based on these assumptions, the energy equation, which is valid in both free stream, porous and solid regions, can be expressed as follows:

$$\rho_f \left(u\frac{\partial T}{\partial x} + v\frac{\partial T}{\partial y} + w\frac{\partial T}{\partial z} \right) = \Gamma_{eff} \left(\frac{\partial^2 T}{\partial x^2} + \frac{\partial^2 T}{\partial y^2} + \frac{\partial^2 T}{\partial z^2} \right) \tag{4.10}$$

In Eq. (4.10), Γ_{eff} represents the effective total heat diffusion coefficient. In the free stream zone, the effective heat diffusion coefficient is sum of the laminar heat diffusion coefficient of the fluid (air) and the turbulent heat diffusion coefficient as given below:

$$\Gamma_{eff} = \frac{k_f}{C_f} + \frac{\mu_t}{Pr_t} \tag{4.11}$$

where k_f and C_f are the thermal conductivity and specific heat of the fluid (air), respectively. μ_t and Pr_t are the turbulent viscosity and turbulent Prandtl number of the fluid (air) in the free stream flow region, respectively.

In the porous medium, the flow is considered to be laminar, and hence, the effective heat diffusion coefficient would only consist of laminar heat diffusion coefficient and can be expressed as:

$$\Gamma_{eff} = \frac{k_{eff}}{C_f} \tag{4.12}$$

where k_{eff} is the effective heat conductivity coefficient in the porous medium. It is calculated as below (Akridiss et al. 2020)):

$$k_{eff} = (1-\varphi)k_s + \varphi k_f \tag{4.14}$$

Here, k_s is the heat conductivity of the porous material's solid skeleton, and k_f is the heat conductivity coefficient of the fluid flowing through the porous material.

In the solid zone (heat generating block), the effective diffusion coefficient will be as follows:

$$\Gamma_{eff} = \frac{k_{solid}}{C_{solid}} \tag{4.13}$$

where, k_{solid} and C_{solid} are the thermal conductivity and specific heat of block material.

4.1.4 *k-ε* Turbulence Model

In the present study, turbulence in the free stream flow region is modelled using the *k-ε* turbulence model. In Cartesian coordinates, the turbulence kinetic energy and turbulence kinetic energy dissipation equations for steady and incompressible flow can be expressed as follows (Holzmann, 2019).

$$\frac{\partial}{\partial x_j}(\rho u_j k) = \frac{\partial}{\partial x_j}\left[\left(\mu + \frac{\mu_t}{\sigma_k}\right)\frac{\partial k}{\partial x_j}\right] + P_k + \rho\varepsilon + P_{kb} \tag{4.15}$$

$$\frac{\partial}{\partial x_j}(\rho u_j \varepsilon) = \frac{\partial}{\partial x_j}\left[\left(\mu + \frac{\mu_t}{\sigma_\varepsilon}\right)\frac{\partial \varepsilon}{\partial x_j}\right] + \frac{\varepsilon}{k}(C_{\varepsilon 1}P_\varepsilon - C_{\varepsilon 2}\rho\varepsilon + C_{\varepsilon 3}P_{\varepsilon b}) \tag{4.16}$$

where $C_{\varepsilon 1} = 1.44,\ C_{\varepsilon 2} = 1.92, C_\mu = 0.09,\ \sigma_k = 1$ and are $\sigma_\varepsilon = 1.3$. The turbulence viscosity (μ_t) is obtained as follows (Holzmann, 2019).

$$\mu_t = \rho C_\mu \frac{k^2}{\varepsilon} \tag{4.17}$$

Since the flow in the porous region is laminar, the k-ε turbulence model equations are solved only in the free stream flow zone.

4.2 BOUNDARY CONDITIONS

After deriving the conservation and turbulence model equations, the boundary conditions for the solution domain must be determined. The flow is symmetric with respect to the x-y plane passing through the middle of the porous layer parallel to the flow. Therefore, the vertical plane at z=0 is the symmetry plane. A symmetry boundary condition is defined for all variables at this symmetry plane. The side, top, and bottom walls of the channel are insulated. At the outlet of the channel, it is assumed that the variations in all variables are negligible. At the inlet of the channel, a uniform fluid velocity and temperature are defined. Heat flux is applied to the lower surface of the block representing the electronic element. All of these conditions are shown in Fig. 4.2.

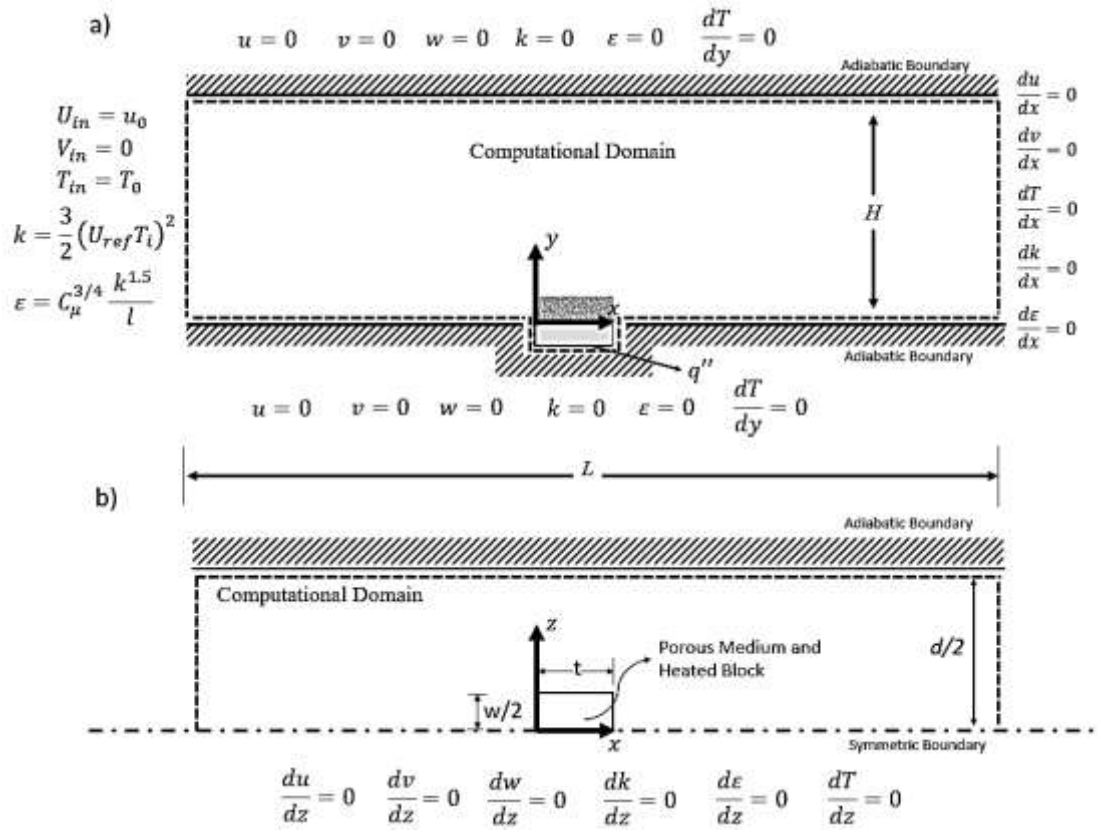

Figure 4.2: Schematic view of computational domain and boundary conditions a) x-y plane (side view), b) x-z plane (top view).

The bottom surface of the channel and the bottom surface of the heated block:

No-slip boundary condition is applied for the velocity components on the surface, i.e,

$u=v=w=0$

It is assumed that the heat generated in the block (electronic element) is applied as a surface heat flux from the bottom surface of the block. Accordingly, the boundary condition for the bottom surface of the block can be mathematically expressed as follows:

$$-\left(k_s \frac{\partial T_s}{\partial y}\right) = q''$$

The bottom surface of the channel is insulated. Therefore, the mathematical expression of the boundary condition on these surfaces can be written as:

$$\left(k \frac{\partial T}{\partial y}\right) = 0$$

Channel entrance, x=-3L/4:

After the honeycomb, it is assumed that the x-component of the air velocity is uniform and the other components are zero. Similarly, the temperature at the entrance is assumed to be uniform and equal to the ambient temperature. Therefore, the velocity and temperature at the entrance can be expressed as follows:

$u = U_0 \quad v=w=0 \quad T=T_0$

At the entrance, the turbulent kinetic energy and turbulent kinetic energy dissipation can be calculated using the following expressions (Holzmann, 2019):

$$k = \frac{3}{2}(|U_{ref}|I)^2 \quad \varepsilon = C_\mu^{3/4} \frac{k^{3/2}}{l}$$

where I is the turbulence intensity which is equal to 0.05. U_{ref} is equal to inlet velocity.

Channel outlet, x=L/4

At the channel outlet, it is assumed that the flow and temperature have reached fully developed conditions and that the changes in all variables in the flow direction (x-direction) can be neglected. Therefore, the following expressions are valid at the exit:

$$\frac{\partial u}{\partial x} = 0 \qquad \frac{\partial v}{\partial x} = 0 \qquad \frac{\partial w}{\partial x} = 0 \qquad \frac{\partial T}{\partial x} = 0$$

$$\frac{\partial k}{\partial x} = 0 \qquad \frac{\partial \varepsilon}{\partial x} = 0$$

Top and side walls of the channel

The top and side surfaces of the channel are insulated solid walls. Adiabatic and no-slip velocity boundary conditions are valid on these surfaces, i.e.

u = 0 v = 0 w = 0 $\frac{\partial T}{\partial n} = 0$

k=0 ε=0

Symmetry plane of the channel (z=0)

The change in the z-direction in all variables on the symmetry surface is zero, i.e.

$\frac{\partial u}{\partial z} = 0$ $\frac{\partial v}{\partial z} = 0$ $\frac{\partial w}{\partial z} = 0$ $\frac{\partial T}{\partial z} = 0$

$\frac{\partial k}{\partial z} = 0$ $\frac{\partial \varepsilon}{\partial z} = 0$

CHAPTER V
NUMERICAL STUDY

The mathematical modeling of the problem results in the continuity, momentum and energy equations, which are inter-dependent and nonlinear differential equations. Therefore, these equations must be solved simultaneously. The solution to these type of problems is possible only by numerical methods.

The numerical solution of a physical problem is carried out in five steps. First, the physical problem and boundary conditions are mathematically formulated. This step requires the derivation of the governing equations and the mathematical expression for the boundary conditions, given in Chapter 4. In the second step, domain discretization is conducted in order to solve governing equations at each node of the mesh system. In the third step, the differential equations are discretized into algebraic equation systems at the nodes. In the fourth step, the algebraic equation systems obtained from the discretization are solved by appropriate algebraic equation solution methods, and the values of the dependent variables (u, v, w, P, T, k and ε) are obtained at grid points. Finally, in step five, vast amount of numerical values of the dependent variables obtained at the nodes are analyzed and desired practically meaningful parameters are calculated. The stages of the CFD methodology followed in this study are illustrated in Fig. 5.1.

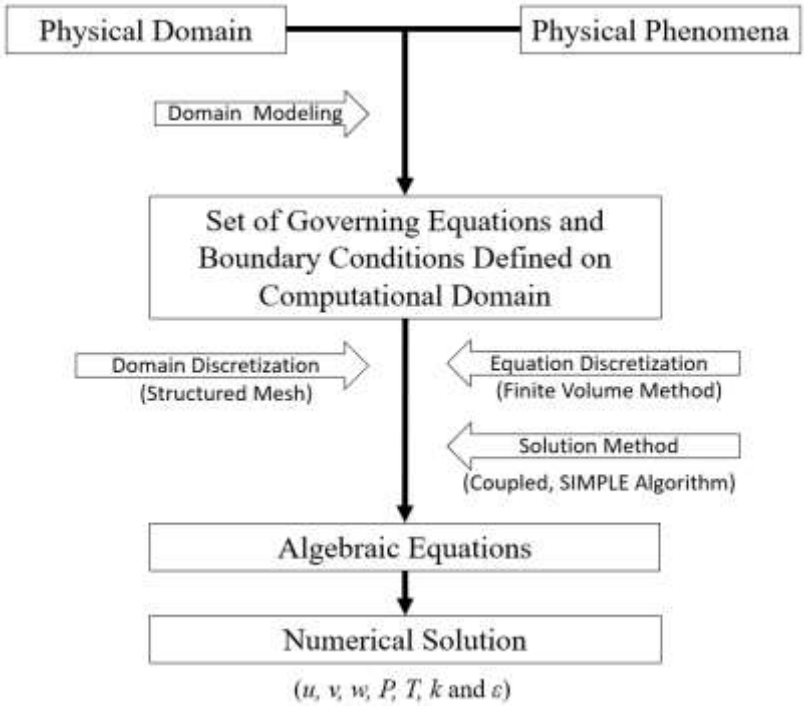

Figure 5.1: The basic stages of the CFD methodology followed in this study

As shown in Fig 5.1, the finite volume method is used to discretize the differential equations into algebraic equations. For the numerical solution of the problem, the problem domain is first divided into finite number of control volumes to create a numerical mesh. The differential equations of the problem are integrated over the finite control volumes and algebraic equations are obtained. For the discretization of the convection terms, the hybrid method is used. For the velocity-pressure coupling, SIMPLE algorithm is utilized.

These techniques are implemented using the *simpleFoam* solver, in the OpenFOAM platform. OpenFOAM does not currently contain momentum and energy equations for porous medium. By modifying the general conservation equations, the equations valid in a porous medium are implemented in *simpleFoam*. The Gauss-Seidel point-by-point iteration technique is used to solve the algebraic equation sets. The convergence of the solution is checked by monitoring the residuals of the continuity, momentum and energy equations. The calculations are repeated until the residuals converge to predetermined convergence criteria. The results obtained from the numerical solution of the problem are presented in the form of velocity vector fields and temperature contour maps in the computational domain. The average Nusselt number over the heated block is calculated from the temperature distribution. Each stage of the CFD methodology is explained briefly below.

5.1 GRID GENERATION

To solve a field equation numerically, a mesh with the finite number of grid points is defined in the computational domain and the values of the dependent variables (u, v, w, P, T, k, and ε) are obtained at these points.

The numerical grid structure significantly affects the numerical solution results. Therefore, the numerical results must be independent of the grid system used. Hence, the grid structure must be carefully created and tested.

The grid system used in the simulations of the present problem is given in Figure 5.2. In this study, a structured mesh was created using the *blockMesh* module of the OpenFOAM platform. A fine mesh structure was formed in the porous medium and its surrounding where the gradients of the dependent variables are high, while a coarse mesh was used in the free flow region. In order to obtain results independent from the number of computational nodes, the simulations were repeated with different grid systems. Evaluating the results obtained with different mesh systems, it was seen that the results independent from the mesh system could be obtained with a mesh of 1362000 nodes. A mesh independence study is conducted for different Reynolds numbers at 14.4 W heat generation rate. As seen in Fig. 5.3, the difference between the numerical and the experimental results are below 0.1% after 1362000 mesh elements. Therefore, it has been observed that the problem becomes independent of the number of mesh elements at 1362000.

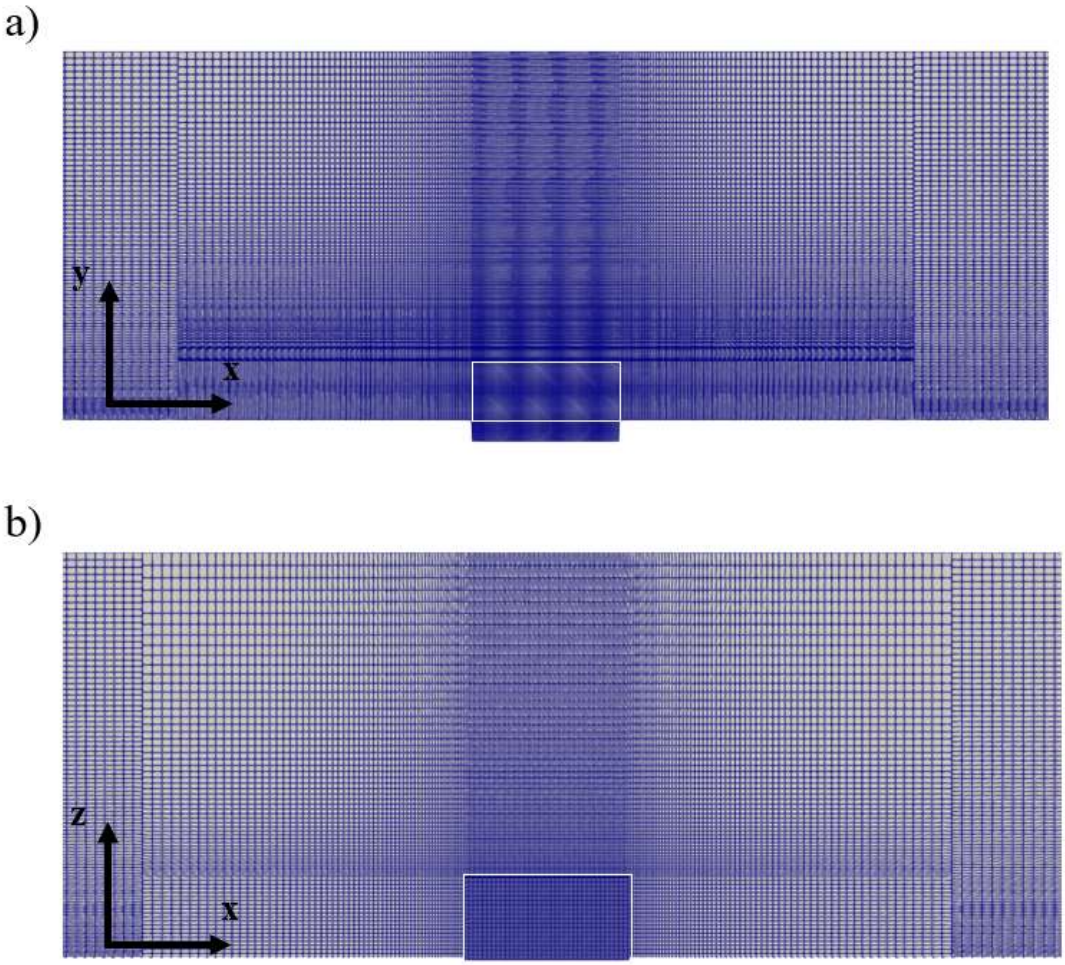

Figure 5.2: Grid structure around the porous medium, a) x-y (vertical) plane, b) x-z (horizontal) plane.

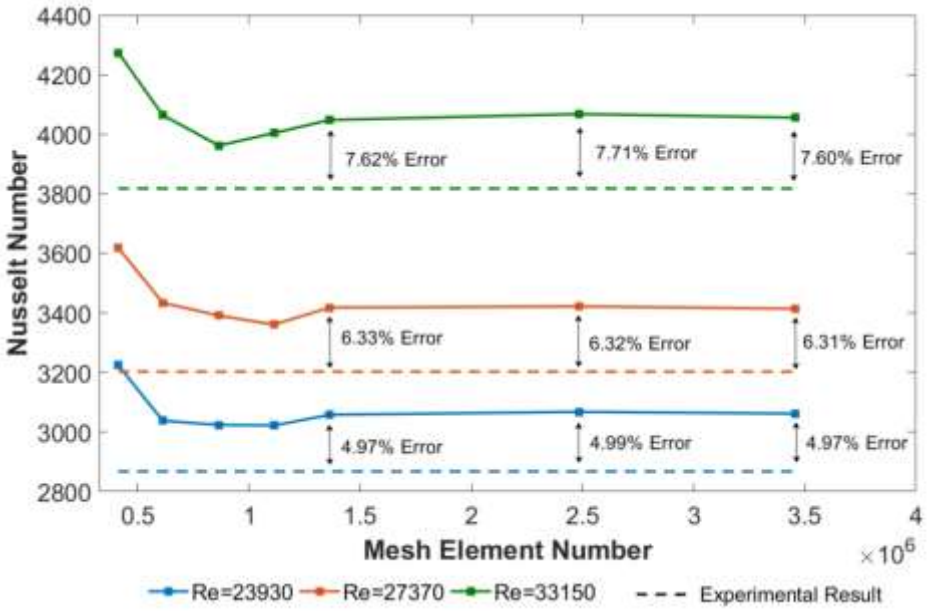

Figure 5.3: Mesh independence study results

5.2 DISCRETIZATION METHODS

In order to solve the governing equations of the problem numerically, the differential equations obtained in Chapter 4 must be discretized. There are four basic methods for discretization. These are:

- Finite Differences Method (FDM),
- Finite Volumes Method (FVM).
- Finite Elements Method (FEM)
- Spectral Method

In this thesis, the open-source CFD solver OpenFOAM, is used to solve the problem. OpenFOAM discretizes governing equations using the finite volume method. FVM involves dividing the computational domain into a set of small control volumes and integrating the governing PDEs within each control volume, a set of algebraic equations are obtained for each dependent variable.

This section provides a brief description about four main discretization methods and the basic differences between these discretization methods. Then, the basic principles of the finite volume method are presented.

5.2.1 Finite Difference Method

The finite difference method is the oldest method used to discretize the differential governing equations. This method uses Taylor series expansion to obtain algebraic formulas for the derivatives in the governing equations, and the equations are transformed into finite difference expressions. As a result, algebraic equations are obtained at each node.

5.2.2 Finite Element Method

The finite-element method, originally developed to solve stress and strain problems in structural analysis. It shares many similarities with the finite-volume method. Both methods are suitable for irregularly shaped computational domains and can handle complex geometries with low error. Linear algebraic equation sets are created to solve unknown flow field variables in the proposed approximate functions for finite elements. By solving the equation sets, the unknown variables in the flow field can be obtained. This approach allows the finite element method to handle complex geometries and boundary conditions. Additionally, the FEM can handle non-linearities and time-dependent problems, which are common in fluid dynamics. There

is no geometric constraint on the solution area in the finite element method. However, more computing resources, i.e., computer time, are required to solve the problem, similar to the finite volume method.

5.2.3 Spectral Method

The spectral method is a type of computational technique that is similar to the finite element methods in that it involves replacing the unknowns of the governing equations with a truncated series in terms of unknown coefficients. The spectral method uses an approximation with either a truncated Fourier series or Chebyshev polynomials for the entire flow domain, whereas the other methods use local approximations. Both the spectral and finite volume methods can be used to solve a wide variety of PDEs, including those that arise in fluid dynamics, structural mechanics, and electromagnetism. The choice of which method to use depends on the specific characteristics of the problem being solved, the complexity of the geometry, and the accuracy required.

5.2.4 Finite Volume Method

The finite-volume method (FVM) is a discretization technique that involves dividing the physical space into a finite number of contiguous control volumes. It was first developed for solution of two-dimensional, time-dependent Euler equations and later extended to three-dimensional flows. In this method, the values of the variables at a grid point in the control volume are calculated. For the variation of the variables between the grid points, generally a piece wise linear function is assumed. An algebraic equation is obtained for each control volume, which includes values from neighboring nodal points.

The finite volume method, which is suitable for structured and unstructured meshes that offer more flexibility for complex geometries. This method is conservative as long as the surface integrals applied at control volume faces are the same for the control volumes that share those faces. The finite-volume method has several advantages, including using a finite-element type mesh made up of triangles or quadrilaterals in two-dimensional and tetrahedra or hexahedra in three-dimensional problems.

In order to formulate the finite-volume method, consider a two-dimensional example of structured (quadrilateral) finite-volumes, as shown in Figure 5.4. This

method relies on the integration the governing equations over control volumes. In this example, the surface areas of the control volume are transformed into projected areas in the x- and y-directions as A_i^x and A_i^y, respectively based on the Cartesian coordinate system. These projected areas are positive if their normal outward vectors point in the same direction as the coordinate system and negative if they do not.

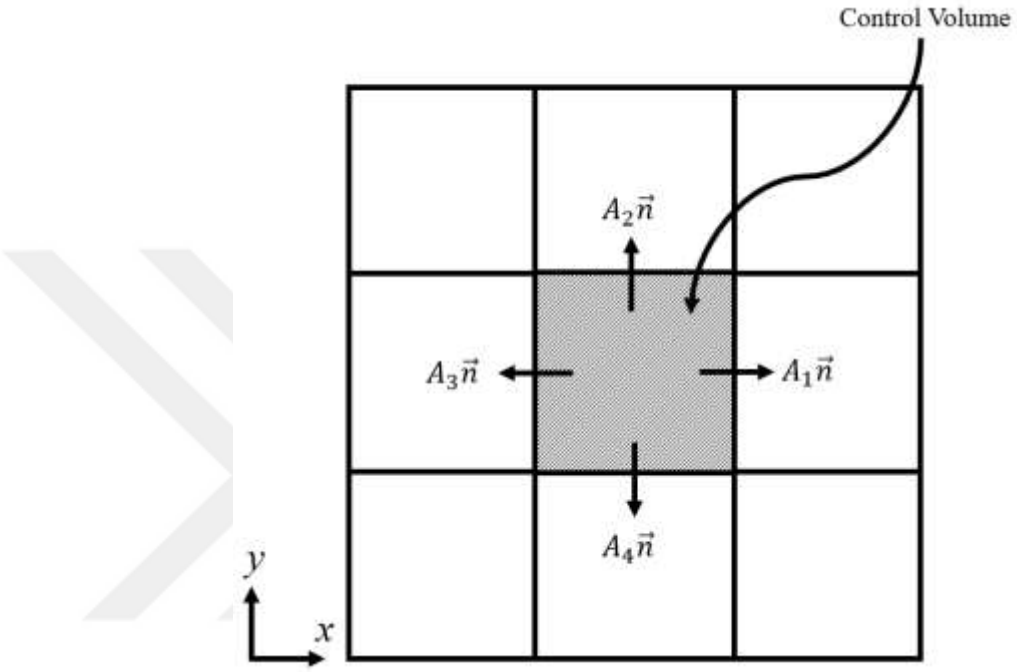

Figure 5.4: A schematic of the structured grid for finite volume method.

The derivative of any field variable (ϕ) in two dimensions of the first order can be obtained by applying the Gauss divergence theorem to the volume integral. The approximations of the variable ϕ along the x- and y-axis are given in Eq. 5.1 and Eq. 5.2.

$$\frac{1}{\Delta V}\int_{\Delta V}\frac{\partial \phi}{\partial x}dV = \frac{1}{\Delta V}\int_{A}\ \phi dA^x \approx \frac{1}{\Delta V}\sum_{i=1}^{N}\phi_i A_i^x \tag{5.1}$$

$$\frac{1}{\Delta V}\int_{\Delta V}\frac{\partial \phi}{\partial y}dV = \frac{1}{\Delta V}\int_{A}\ \phi dA^y \approx \frac{1}{\Delta V}\sum_{i=1}^{N}\phi_i A_i^y \tag{5.2}$$

where ϕ_i are the variable values at the control volume faces and N is the number of bounding surfaces on the elemental volume. It should be noted that N is four since

there are four bounding surfaces of the control volume in Fig. 5.3. In the three-dimensional case, *N* becomes six due to the number of hexagonal element surfaces.

There is no difference in the process of discretizing second-order derivatives compared to first-order derivatives. The second-order derivatives along the x and y directions are given in Eq. 5.3 and Eq 5.4.

$$\frac{1}{\Delta V}\int_{\Delta V}\frac{\partial^2\phi}{\partial x^2}dV = \frac{1}{\Delta V}\int_{A}\frac{\partial\phi}{\partial x}\,dA^x \approx \frac{1}{\Delta V}\sum_{i=1}^{N}\left(\frac{\partial\phi}{\partial x}\right)_i A_i^x \tag{5.3}$$

$$\frac{1}{\Delta V}\int_{\Delta V}\frac{\partial^2\phi}{\partial y^2}dV = \frac{1}{\Delta V}\int_{A}\frac{\partial\phi}{\partial y}dA^y \approx \frac{1}{\Delta V}\sum_{i=1}^{N}\left(\frac{\partial\phi}{\partial y}\right)_i A_i^y \tag{5.4}$$

To calculate the values of the first-order derivatives at the faces of a control volume, discrete values of the surrounding control volumes are usually used. In a structured mesh configuration, as shown in Figure 5.4, where there is only one adjacent control volume on each face surrounding the central control volume, the first-order derivatives can be estimated by using a piecewise linear gradient profile between the central and adjacent nodes. When a higher degree of accuracy is needed for the numerical solution, higher-order quadratic profiles can be used, but this requires more surrounding elements within the mesh system.

Here, in this section, the discrete approximation method of the steady-state diffusion equation, which is also used in the solid region (electronic component) of the computational domain, is shown below as an example.

The steady-state one-dimensional diffusion equation of a variable ϕ can be given by;

$$\frac{\partial}{\partial x}\left(\Gamma\frac{\partial\phi}{\partial x}\right) + S_\phi = 0 \tag{5.5}$$

where Γ is the diffusion coefficient and S_ϕ is the source term. This equation is a one-dimensional diffusion process. As mentioned before, when the finite-volume method is employed, it is necessary to divide the physical domain into a series of finite control volumes situated around specific nodal points, such as *W, P,* and *E*. An illustration of this concept can be seen in Fig. 5.5, which depicts a control volume around the nodal point *P*. The distances between the nodal points *W* and *P* and between the nodal points

P and *E* are denoted by the notations δx_w and δx_E, respectively. In the case of this one-dimensional illustration, the width of the control volume around the nodal point *P* is designated as Δx, as the dimensions of Δy and Δz are of unit length.

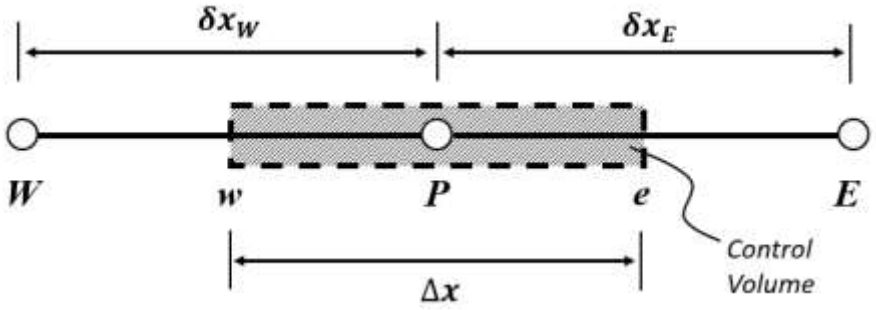

Figure 5.5: A schematic representation of a control volume around a node P in a one-dimensional domain.

In order to apply the finite volume discretization, the steady state diffusion equation in Eq. 5.5 can be approximated by the use of Eq. 5.1.

$$\frac{1}{\Delta V}\int_{\Delta V}\frac{\partial}{\partial x}\left(\Gamma\frac{\partial \phi}{\partial x}\right)dV = \frac{1}{\Delta V}\int_{A}\left(\Gamma\frac{\partial \phi}{\partial x}\right)dA^x \approx \frac{1}{\Delta V}\sum_{i=1}^{2}\left(\Gamma\frac{\partial \phi}{\partial x}\right)_i A_i^x \tag{5.6}$$

In Eq. 5.6, the projected area A_i^x for the one-dimensional case can be defined as $A_1^x = -A_w$ and $A_2^x = A_E$. Source term in Eq. 5.5 can be approximated as

$$\frac{1}{\Delta V}\int_{\Delta V} S_\phi dV = S_\phi \tag{5.7}$$

where the source term is assumed constant within the finite control volume. The final form of the equation becomes as follows:

$$\frac{1}{\Delta V}\left(\Gamma\frac{\partial \phi}{\partial x}\right)_e A_E - \frac{1}{\Delta V}\left(\Gamma\frac{\partial \phi}{\partial x}\right)_w A_W + S_\phi = 0 \tag{5.8}$$

To express Eq. (5.8) in algebraic terms for the nodal points *W*, *E*, and *P*, approximations for the gradients $\partial\phi/\partial x$ at the west and east faces of the control volume are required. For this purpose, the variation of ϕ between the grid points may be considered piece-wise linear to approximate the first-order derivatives at control

volume faces '*w*' and '*e*'. Subsequently, the fluxes resulting from diffusion shall be determined as follow:

$$\left(\Gamma\frac{\partial\phi}{\partial x}\right)_e A_E = \Gamma_e A_E\left(\frac{\phi_E-\phi_P}{\delta x_E}\right) \tag{5.9}$$

$$\left(\Gamma\frac{\partial\phi}{\partial x}\right)_w A_W = \Gamma_w A_W\left(\frac{\phi_P-\phi_W}{\delta x_W}\right) \tag{5.10}$$

Substituting Eq 5.9 and 5.10 into Eq. 5.8;

$$\frac{\Gamma_e A_E}{\Delta V}\left(\frac{\phi_E-\phi_P}{\delta x_E}\right)-\frac{\Gamma_w A_W}{\Delta V}\left(\frac{\phi_P-\phi_W}{\delta x_W}\right)+S_\phi=0 \tag{5.11}$$

Rearranging Eq 5.11 gives;

$$\frac{1}{\Delta V}\left(\frac{\Gamma_e A_E}{\delta x_E}+\frac{\Gamma_w A_W}{\delta x_W}\right)\phi_P=\frac{1}{\Delta V}\left(\frac{\Gamma_e A_E}{\delta x_E}\right)\phi_E+\frac{1}{\Delta V}\left(\frac{\Gamma_w A_W}{\delta x_W}\right)\phi_W+S_\phi=0 \tag{5.12}$$

By identifying the coefficients of ϕ_E and ϕ_W in Eq. (5.12) as a_E and a_W and the coefficient of ϕ_P as a_P, the algebraic form of the differential equation can be written as;

$$a_P\phi_P=a_E\phi_E+a_W\phi_W+b \tag{5.13}$$

where

$$a_E=\frac{1}{\Delta V}\left(\frac{\Gamma_e A_E}{\delta x_E}\right) \tag{5.14}$$

$$a_W=\frac{1}{\Delta V}\left(\frac{\Gamma_w A_W}{\delta x_W}\right) \tag{5.15}$$

$$a_P=a_E+a_W \tag{5.16}$$

$$b = S_\phi \tag{5.17}$$

Equation (5.13) represents the discretized form of the differential equation (Eq. 5.5) through the finite-volume method. For the one-dimensional problem considered here, the face areas A_E and A_W are taken unity since Δy and Δz have dimensions of unit length. A similar method can be applied to two and three-dimensional computational domains.

One of the key components of the FVM is the use of schemes, which are used to approximate the solution of a PDE at the center of each cell in the FVM. There are various types of schemes that can be used for convection terms in the FVM, such as the central difference, the upwind method, the hybrid method, the power law method, and the exponential schemes. Each type of scheme has its own advantages and disadvantages, and the choice of the scheme depends on the specific problem and the desired level of accuracy (Tu et al. 2008).

When these methods are examined individually, it is observed that the central difference method gives good results for low fluid velocity values, but as the velocities increase, accuracy decreases. The first-order upwind scheme is simple and easy to implement, but it is not very accurate. The second-order upwind scheme is more accurate than the first-order upwind scheme, but it is more computationally intensive. The central difference scheme is also more accurate than the first-order upwind scheme, but it is sensitive to grid resolution. The exponential scheme is usually more accurate than low-order schemes, such as the first-order upwind and central difference schemes, but it is also more computationally intensive. It is also more suitable for solving problems involving a high degree of non-linearity, like convection-diffusion problems with a high Peclet number (Ferziger and Perić 2002, Patankar 1980, Tu et al. 2008, Wendt 2009).

In this study, second order upwind method is used to discretize the convection terms.

5.3 SOLUTION OF ALGEBRAIC EQUATIONS

In computational fluid dynamics applications, solving algebraic equations is an essential step in simulating fluid flow behavior. There are two main methods for solving algebraic equations, direct and iterative methods (Tu et al. 2008).

The direct method is a method that solves the system of algebraic equations directly. It is based on using matrix operations. The most common direct method is the Lower-Upper decomposition method, which is used to solve systems of linear equations. This method is efficient and accurate, but it can become computationally expensive for complex problems (Ferziger and Perić 2002, Tu et al. 2008).

The iterative methods are the methods in which the solution is started with assumed values and then iteratively the solution is improved. The Jacobi, Gauss-Seidel, and Successive Over-Relaxation methods are the most common iterative methods. These methods are less computationally expensive than direct methods and can be used for large systems of equations (Ferziger and Perić 2002, Patankar 1980).

In this thesis study, the Gauss-Siedel iteration technique is used to numerically solve the algebraic equation systems obtained by discretizing the governing equations. In this solution method, one unknown is solved from each equation, as if the others were known. Therefore, a set of initial values is assumed for the unknowns in the first iteration, and then the same operations are repeated using the latest current values, and the solution is reached step by step. In such iterative methods, a convergence criterion is needed to control the adequacy of the results. This criterion checks whether the change in all variables in consecutive iterations is sufficiently small and ensures that the iteration is repeated until the changes are less than the prescribed value.

5.4 SIMPLE ALGORITHM

SIMPLE (Semi-Implicit Method for Pressure-Linked Equations) algorithm is an iterative method that is based on the pressure-velocity coupling principle. It is used to solve the governing equations for both incompressible and compressible flows in a relatively simple and efficient way. The algorithm decomposes the Navier-Stokes equations into velocity equations and then solves them iteratively. The pressure equation is solved first, and then the velocity equation is solved using the updated pressure value (Tu et al. 2008). This stage is called as pressure-velocity coupling.

The pressure-velocity coupling principle is used in the SIMPLE algorithm to solve the Navier-Stokes equations iteratively. The algorithm starts by assuming an initial value for the pressure field and then the momentum equations are solved for the velocity field using the assumed pressure value. Next, the pressure correction equation is solved and the pressure field is corrected. Then the velocity field is updated by using

the corrected pressure field solving the momentum equation again. This process is repeated until the solution converges.

The basic steps of the SIMPLE algorithm are as follows (Patankar 1980):

1. Discretization: The first step is to discretize the governing equations using a finite volume method, as mentioned in section 5.2.

2. Momentum equation: The momentum equation is solved for the velocity field. This is done by assuming an initial value for the pressure and then solving the momentum equation for the velocity field using this value.

3. Pressure correction: The pressure correction equation is solved to correct the value of the pressure field. This is done by solving the continuity equation for the pressure field.

4. Velocity correction: The velocity field is corrected by using the updated pressure value. This is done by solving the momentum equation for the velocity field using the updated pressure value.

5. Turbulence and energy equation: The energy equation (T), turbulent kinetic energy (k) equation, and turbulent kinetic energy dissipation (ε) equation are solved.

6. Convergence check: The solution is checked for convergence by comparing the values of the pressure and velocity fields from the current iteration to the values from the previous iteration. The process is repeated until the solution converges.

7. Post-processing: The final step is to post-process the simulation results, which typically includes visualizing and analyzing the data.

5.5 PROGRAM DEVELOPMENT

In this thesis study, a CFD solver for heat transfer and flow analysis have been developed based on OpenFOAM platform. The development process started with a one-dimensional Darcy solver, and then the code was developed step by step into the three-dimensional solver. During the process, the *simpleFoam* solver was utilized. *simpleFoam* is based on the SIMPLE algorithm in the OpenFOAM CFD library. *simpleFoam* is used to simulate incompressible, steady-state, laminar, and turbulent flows. It uses the finite volume method to discretize the governing equations. However, it does not contain the governing equations for porous materials, based on the Darcy-Forchaimer assumptions. Therefore, the governing equations have been

modified as described in Section 4.1, based on the *simpleFoam*. In this section, the solver used during the development process of the final solver have been briefly described. However, the validation and testing procedures have not been covered. In contrast, the validation procedures for the *buoyantPorousSolver*, which is used as the final solver, have been explained in detail.

During the development of the solver, four different solvers were developed progressively. A step-by-step program development strategy is as follows:

1. *darcySolver*: One-dimensional steady-state solver based on Darcy Equation for incompressible fluids.

2. *darcyTempSolver*: Three-dimensional steady-state solver based on Darcy Equation and energy equation for incompressible flows.

3. *porousSimpleFoam*: Three-dimensional steady-state solver for incompressible, turbulent flow. Momentum Equations are modified with source terms that include Darcy-Forcheimer equations. A developed version of the *simpleFoam* that is already included in the OpenFOAM library.

4. *buoyantPorousSolver*: Steady-state, three-dimensional solver for incompressible, turbulent flow. A developed version of the *porousSimpleFoam* in order to solve energy equations. *buoyantPorousSolver* is also the final version of the solver in this thesis study.

5.6 VERIFICATION OF NUMERICAL RESULTS

5.6.1 Verification with an Experimental Study in the Literature

To validate the numerical results, a problem that has been experimentally studied in the literature by Kurtbaş and Çelik (2009) was solved using the developed numerical solution method, and the numerical results were compared with the experimental results. The schematic view of the problem studied by (Kurtbas and Celik 2009) is given in Fig 5.6.

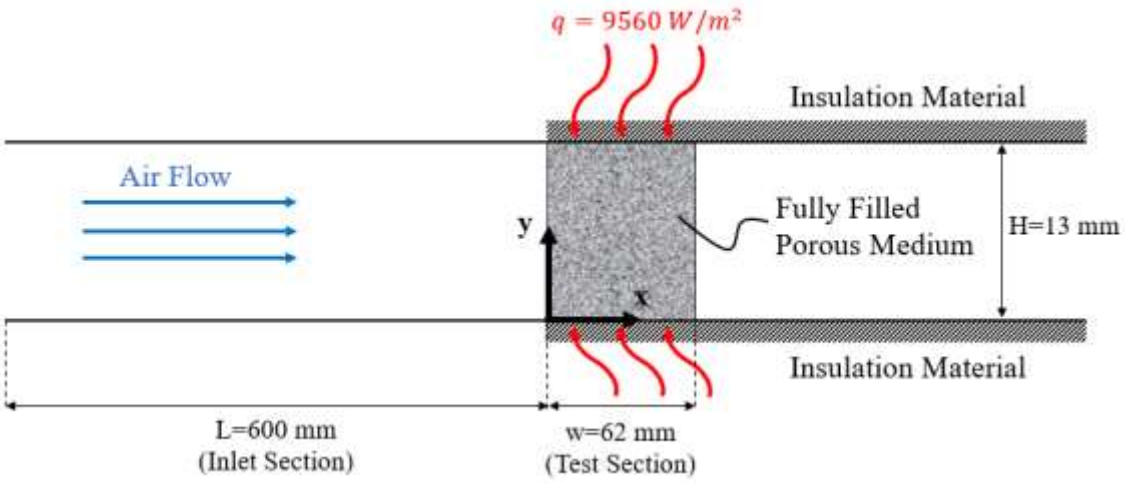

Figure 5.6: The schematic view of the problem studied by Kurtbas and Celik (2009).

The experimental setup is a rectangular channel with a porous medium of 62 mm width at a section of the channel as shown in Fig. 5.5. A constant heat flux of 9560 W/m^2 is applied to the porous material through the channel. Temperature measurements are taken from the test section with 12 thermocouples. Six thermocouples were placed on the lower and upper walls of the test section. The thermophysical properties of the porous medium used in the study are given in Table 5.1.

Table 5.1: Properties of the porous medium used by Kurtbas and Celik (2009).

Pore Density (PPI)	10	20	30
Materials	AL-6101	AL-6101	AL-6101
Porosity	0.93	0.93	0.93
Permeability	1.04E-7	0.76E-7	0.63E-7

The local Nusselt number for each row was determined by using the equation:

$$\mathrm{Nu}_{\mathrm{H,i}} = \frac{q'' H}{(T_w - T_{in})k_{hava}} \tag{5.18}$$

where q″ represents the heat flux applied through the channel wall, k_{air} represents the thermal conductivity of the air, and H represents the channel height. The wall temperature T_w was was calculated as the average of the temperatures measured on the lower and upper walls. No measurements were taken on the front and back walls.

$$T_w = \frac{(T_w)_{upper\ wall} + (T_w)_{lower\ wall}}{2} \tag{5.19}$$

The average Nusselt number was calculated using the following equation:

$$\overline{Nu_H} = \frac{\int_0^L Nu_H dx}{\int_0^L dx} \cong \frac{\Delta x}{L} \sum_{i=1}^{n} Nu_H \tag{5.20}$$

In Eq. 5.20, *L* represents the length of the prous material placed section, *n* represents the number of thermocouples, and *Δx* represents the distance between two thermocouples.

In the validation studies, the Reynolds number range of 8000<Re<18000 was considered and analyses were performed using porous mediums with different permeability.

The Nusselt number results obtained in the experimental study conducted by Kurtbas and Celik (2009) were compared with the results obtained from the numerical analyses in this study. In Fig 5.7, variations of the Nusselt number with Reynolds number for different pore numbers are compared. Upon the examination of the results, it can be seen that the average Nusselt number values obtained from the CFD analyses are slightly higher than the experimental data, but the difference between them is at an acceptable level. The average Nusselt number difference is less than 6% for all analyses. This result shows that the mathematical model, the numeric method and computer program developed in the present study gives acceptable results.

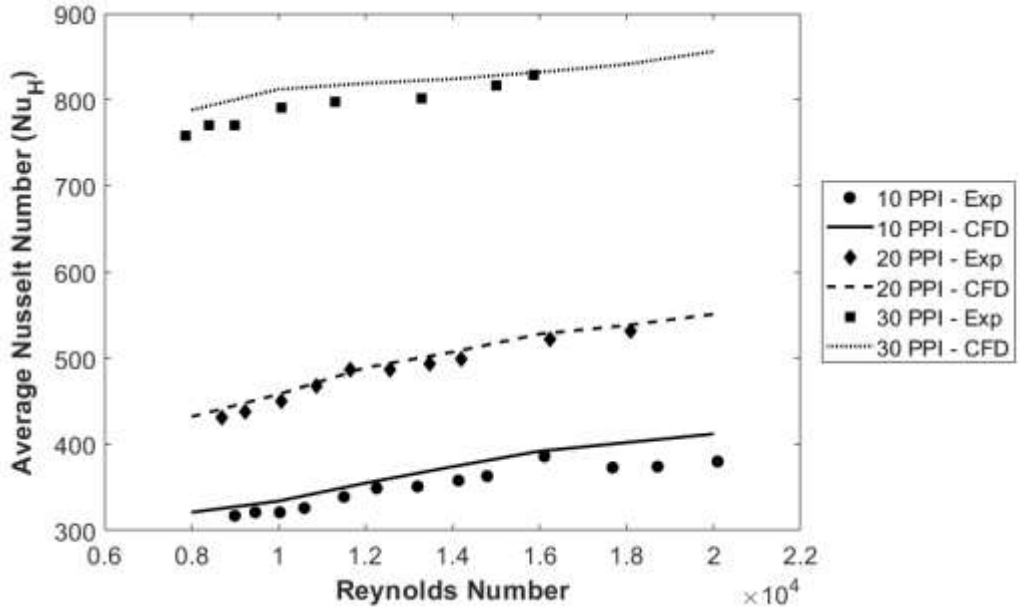

Figure 5.7: Comparison of average Nusselt Numbers obtained numerically in the present study and experimentally by Kurtbas and Celik (2009).

The numerical results have been verified with an experimental study in the literature in this stage of the thesis study as a preliminary study. In the ongoing stage of the study, an experimental data set was obtained within this thesis study from the experimental setup.

5.6.2 Verification with the Experimental Results of the Present Study

The numerical methodology followed here has been used directly to perform validation studies for the experiments carried out within the thesis study. The experimental setup detailed in Chapter 3 was analyzed using the numerical methodology employed in this study. The temperature values of the heated block (brass block) obtained from the experimental study were examined for validation. In addition, both numerical and experimental results were compared using the Nusselt number formulation given in Chapter 3.

Experiments were performed with different heat generation values. Experimental and numerical results obtained at different Reynolds numbers at constant heat generation values are compared in Fig. 5.8. In the numerical study, it was assumed that the temperature data for the 3rd and 4th thermocouples were equal to the temperature values obtained from the 1st and 2nd thermocouples, since the problem was modeled symmetrically. When the graphs are examined, it is seen that the temperature measured by thermocouple 1 and 3 are lower than the temperature values

at points 2 and 4. At the same time, it was observed that the temperature curves show similarity in both studies. The maximum error is 4.17% and occurred at thermocouple#3 when the Reynolds number is 33150 for heat generation Q=18.3 W.

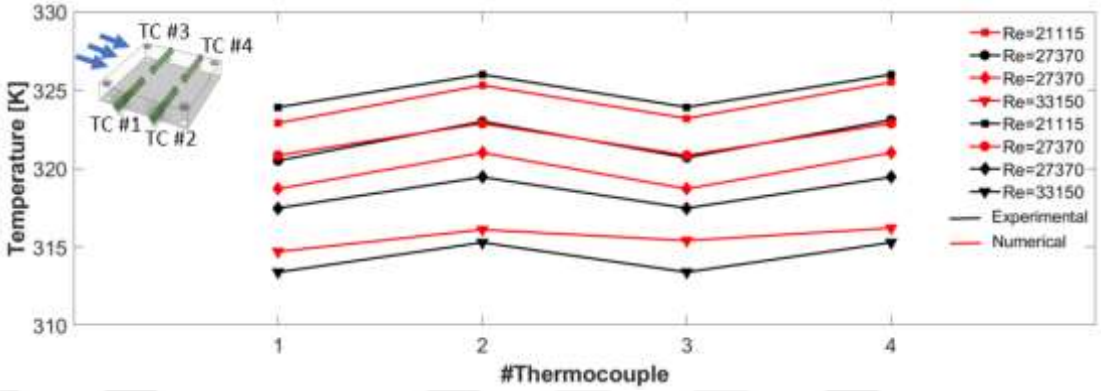

Figure 5.8: Comparison of experimental and numerical temperature data at different Reynolds numbers for heat generation Q=18.3 W

Figure 5.9 shows the variation of the Nusselt number based on the porous medium height with Reynolds number for experimental and numerical studies conducted at different heat generation and Reynolds number values. Since the Nusselt number is independent of the heat generation values, very close Nusselt number values are obtained for a given Reynolds number in the numerical studies. In experimental studies, Nusselt numbers show differences with heat flow, especially at low Reynolds numbers. This can be attributed to measurement errors that occur during experimental studies. When the data is examined, it is seen that the highest Nusselt number difference between experimental and numerical studies conducted under the same conditions occurred at 18.2 W heat generation and 33150 Reynolds number, with a percentage error of 7.33. When this error rate is examined in the literature, it is seen to be within acceptable limits, and it can be said that the developed mathematical model and numerical solution method give realistic results (Mancin et al. 2012).

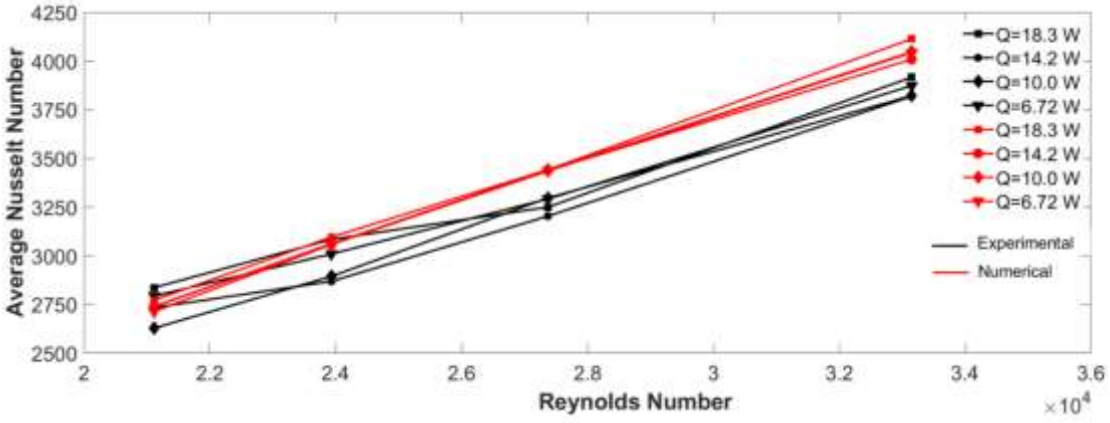

Figure 5.9: Nusselt numbers obtained experimentally and numerically at different heat power and Reynolds number values with the Reynolds number.

CHAPTER VI
EXPERIMENTAL RESULTS

In the experiments, a porous medium made of 99.7% aluminum alloy with 10 PPI pore density, 0.95 porosity, and an average pore diameter of 4 mm was used as the porous medium. A layer of this porous medium is on the top surface of the heat generating block. The experiments were conducted at Reynolds numbers 33150 21150, 23930, and 27370, for heat generating rates of 18.3 W, 14.2 W, 12 W, and 10. In the experimental study, 20 different cases were investigated. The parameter values related to the experimental studies are given in Table 6.1.

Table 6.1: Cases studied experimentally.

Case	Reynolds Number (Re)	Heat Generation (Watt)	Cooling Attachment
1	21115	18.3	Porous Medium
2	23930	18.3	Porous Medium
3	27370	18.3	Porous Medium
4	33150	18.3	Porous Medium
5	21115	18.3	None
6	23930	18.3	None
7	27370	18.3	None
8	33150	18.3	None
9	21115	14.2	Porous Medium
10	23930	14.2	Porous Medium
11	27370	14.2	Porous Medium
12	33150	14.2	Porous Medium
13	21115	10	Porous Medium
14	23930	10	Porous Medium
15	27370	10	Porous Medium
16	33150	10	Porous Medium
17	21115	6.72	Porous Medium
18	23930	6.72	Porous Medium

Table 6.1 Continue

Case	Reynolds Number (Re)	Heat Generation (Watt)	Cooling Attachment
19	27370	6.72	Porous Medium
20	33150	6.72	Porous Medium

Four experiments were carried out without attaching porous medium on the heated block to observe the effect of porous medium on heat transfer. In the rest of experiments, porous medium was attached on the heated block. The experiments were carried out as described in Chapter 4 and the data was evaluated to calculate the Nusselt number.

The temperature values measured inside the block from four points with a heating power of 18.3 W at different Reynolds numbers are given in Fig. 6.1.

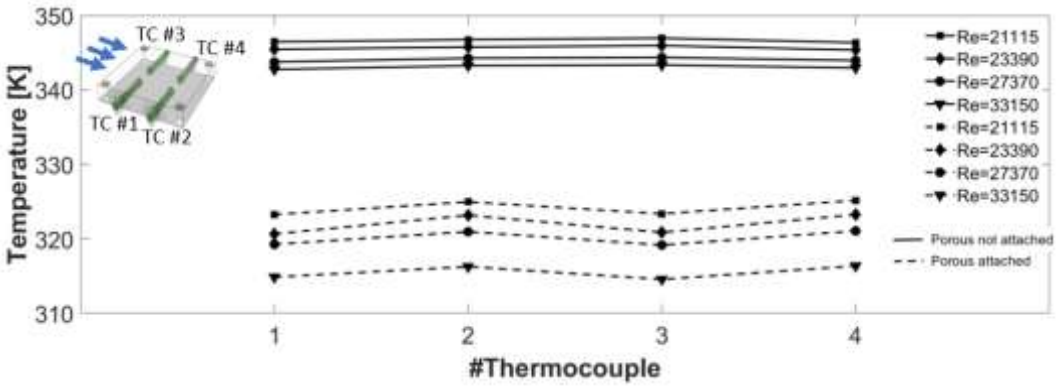

Figure 6.1: Temperature values obtained at different points inside the block with 18.3 W heating power at different Reynolds numbers with and without porous medium.

Upon examining Fig. 6.1, it can be seen that the temperatures in the cases where the surface of the block is covered with porous medium are approximately 25 K lower than the temperatures in the cases where it is not covered with a porous layer for all Reynolds numbers considered. This shows that porous medium can effectively increase the heat transfer when used as a cooling element. In addition, in the experiments where porous medium was used, lower temperatures were observed at points 1 and 3. This is because points 1 and 3 are located at the upstream side of the block. The fluid reaching the porous medium is at the ambient temperature. As the air flows over the porous medium, its temperature increases. As a result, the temperature of the solid matrix at downstream side of the block increases. Thus, the temperature readings from points 2 and 4, which are located on the downstream are higher.

The Nusselt number based on the porous medium height has been calculated at different Reynolds numbers for the cases with and without porous medium. The results obtained are given in Fig. 6.2. When the results are examined, it is seen that the Nusselt number in the cases where porous medium is used is approximately twice the Nusselt number in the cases where porous medium is not used for all Reynolds numbers. The effect of the Reynolds number on the Nusselt number is very small when the porous medium is not used, while when the porous medium is used, there is approximately a linear increase in the Nusselt number as the Reynolds number increases. Therefore, it can be said that porous mediums as a cooling element is an effective technique.

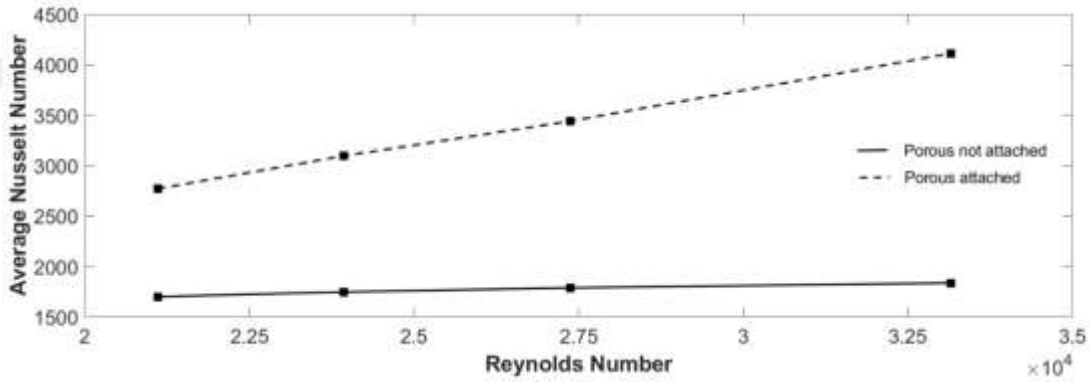

Figure 6.2: Variation of the Nusselt number with Reynolds number with and without porous layer for 18.3 W heating.

With the porous medium placed on the block, experiments were performed with different heat generation values. Experimental results obtained at different Reynolds numbers at constant heat generation values are compared in Fig. 6.3-6.5. When the graphs are examined, it is seen that the temperature measured by thermocouples 1 and 3 are lower than the temperature values at points 2 and 4.

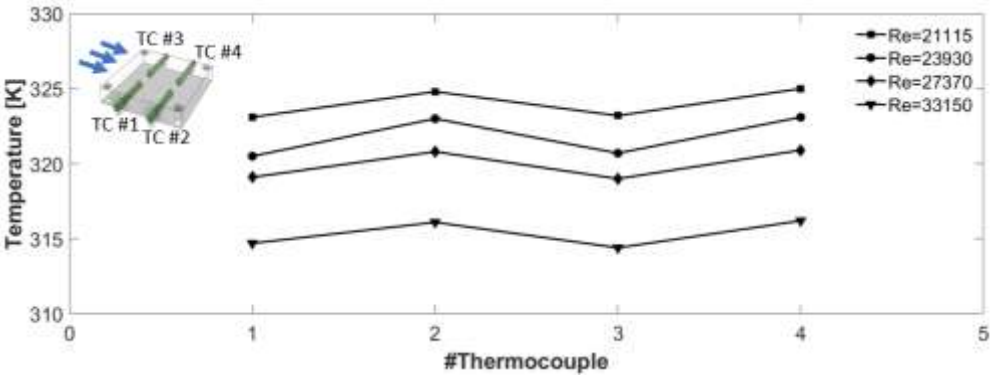

Figure 6.3: Comparison of experimental and numerical temperature data at different Reynolds numbers for heat generation Q=18.3 W

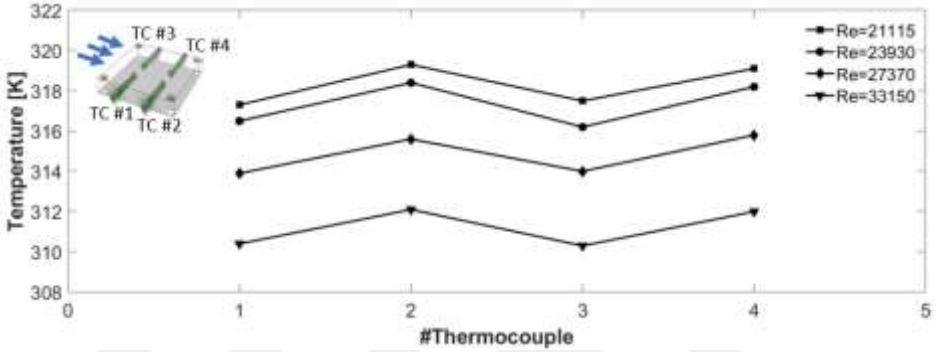

Figure 6.4: Comparison of experimental and numerical temperature data at different Reynolds numbers for heat generation Q=14.2 W

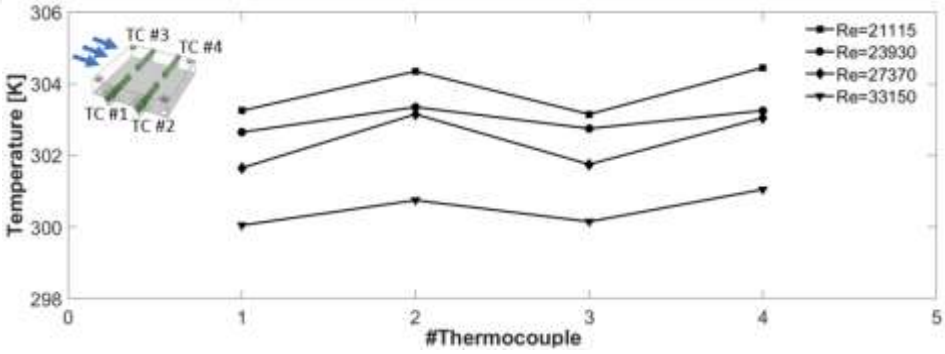

Figure 6.5: Comparison of experimental and numerical temperature data at different Reynolds numbers for heat generation Q=6.72 W

Figure 6.6 shows the variation of the Nusselt number based on the porous medium height with Reynolds number for experimental studies conducted at different heat generation and Reynolds number values. Since the Nusselt number is independent of the heat generation values, very close Nusselt number values are obtained for a given Reynolds number in the numerical studies as shown in Chapter 5.5. In experimental studies, Nusselt numbers show differences with heat flow, especially at

low Reynolds numbers. This can be attributed to measurement errors that occur during experimental studies.

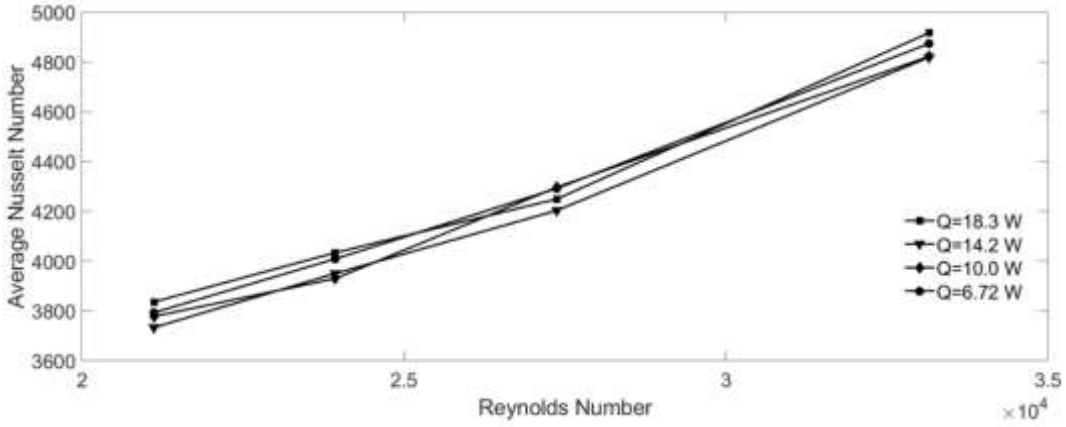

Figure 6.6: Nusselt numbers obtained experimentally and numerically at different heat power and Reynolds number values with the Reynolds number.

CHAPTER VII
NUMERICAL RESULTS

In this chapter, the results of the numerical analysis are presented. In these analyses, the effects of the Reynolds number, the heat generation rate in the block, the porosity of the porous medium, the ratio of the porous layer thickness to the channel height (*h/H*), and the ratio of the porous medium width to the height (*t/h*) on flow and heat transfer were studied under turbulent flow conditions.

The geometry of the problem was selected based on the dimensions of the graphic cards used in a desktop computer and its cooling attachment. The dimensions of the heated block (GPU graphic processing unit) were taken as 40×40×8 mm which are same as the block considered in the experimental study. The porous medium (cooling attachment) height is h=16 mm and completely covers the upper surface of the heated block. In the computational domain, the heated block representing the electronic component and porous medium were modeled as a solid and porous region, similar to experimental studies. However, in order to save computational resources, the flow is considered to be symmetric about the vertical plane passing through the mid-line of the block along the channel.

The air enters the channel with a uniform velocity profile and becomes fully developed in the distance of $20\times D_h$ before reaching the porous medium covered heated block. The air temperature at the channel inlet is taken as T_0=290 K. The heat generated in the brass block (electronic component) is defined as heat flux on the bottom surface of the brass block. The air velocity at the channel inlet is determined based on the Reynolds number for which the analysis is performed. The average Nusselt number over the heated block is calculated from the temperature distribution calculated. However, especially in cases where the effect of channel height is studied, the effect of hydraulic diameter on Nusselt number is dominant compared to the heat transfer coefficient. Therefore, as stated before in Section 3.3, the Nusselt number based on the height of the porous medium has also been calculated for each case.

Numerical analyses were performed for four different heat generation (Q) values, 14 different porosities, eight different h/H values, and four different t/h parameters within the Reynolds number range of 15000-50000. In total, the calculations were performed for 460 different cases, and simulation results are presented for selected cases in this chapter. The values of the parameters considered in the numerical analysis are given in Table 7.1.

Table 7.1: Parameter matrix for numerical analyses

Reynolds Number (Re)	**Heat Generation (W)**	**Porosity (%)**	***h/H***	***t/h***
15000	18.3	0.98	0.064	2.5
20000	14.2	0.95	0.08	2.81
25000	10.0	0.94	0.16	3.125
30000	6.72	0.93	0.20	3.75
35000		0.92	0.25	
40000		0.91	0.33	
45000		0.90	0.5	
50000		0.85	0.66	
		0.80		
		0.75		
		0.70		
		0.65		
		0.60		
		0.55		

7.1 THE EFFECTS OF REYNOLDS NUMBER ON HEAT TRANSFER

In order to observe the effects of the Reynolds number on flow and heat transfer, all the geometric parameters were kept constant, and the Reynolds number was varied between from 15000 to 50000.

Figure 7.1. shows the dimensionless velocity (u/u_∞) profiles at different cross-sections for Q=18.3 W, h/H=0.064, φ=0.95, and t/h=2.5 at different Reynolds numbers. In this figure, the velocity profiles are shown within the range of 0-80 mm of the channel height in order to better visualize the velocity variation better inside the porous medium. When the velocity profiles are examined, it is seen that the changes in u/u_∞ profiles along the y-axis are similar for all Reynolds numbers considered both

in the free stream region and in the porous layer region. This is because the porosity and pore size of the porous medium are the same for the cases presented in Fig. 7.1.

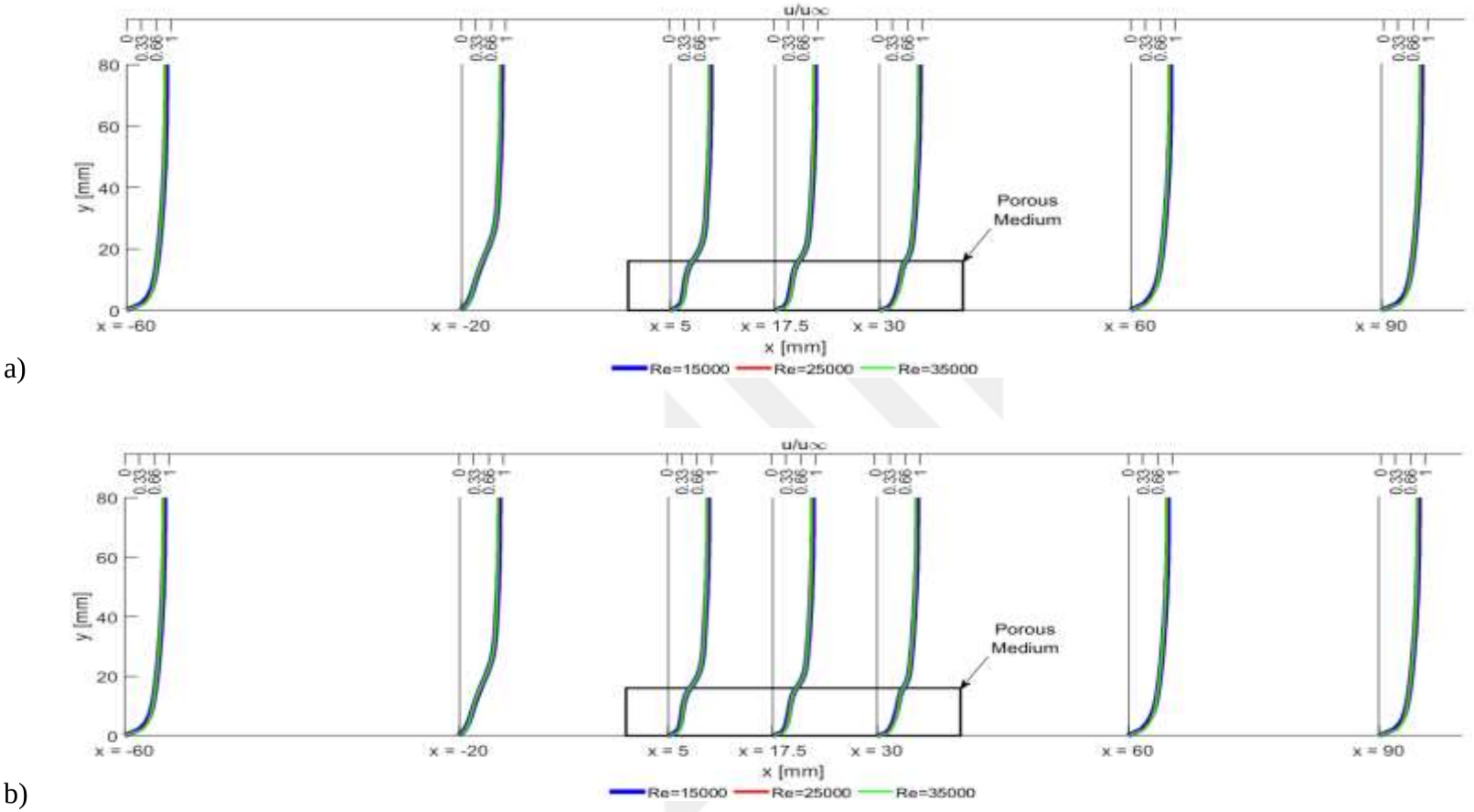

Figure 7.1: Dimensionless velocity (u/u_∞) profiles in the range of y=0 and y=80 mm from the bottom surface at different Reynolds numbers for Q = 18.3 W, h/H=0.064, φ=0.95, and t/h=2.5.

In Figure 7.2., the temperature contours are given for different Reynolds numbers in the vertical plane passing through z=10 mm with 18.3 W heat generation, *h/H*=0.064, *φ*=0.95, and *t/h*=2.5. Figure 7.3 illustrates the temperature contours in the horizontal plane passing through y=0 mm (between the heated block and porous medium) for the same case. It is seen that the Reynolds number significantly affects the temperature field in the heated block and porous medium. At low Reynolds numbers, the temperatures of the heated block and porous medium vary between 320 K - 326 K. However, at high Reynolds numbers, it can be observed that the temperature drops nearly to the inlet temperature, particularly in the region of the porous medium opposing the flow.

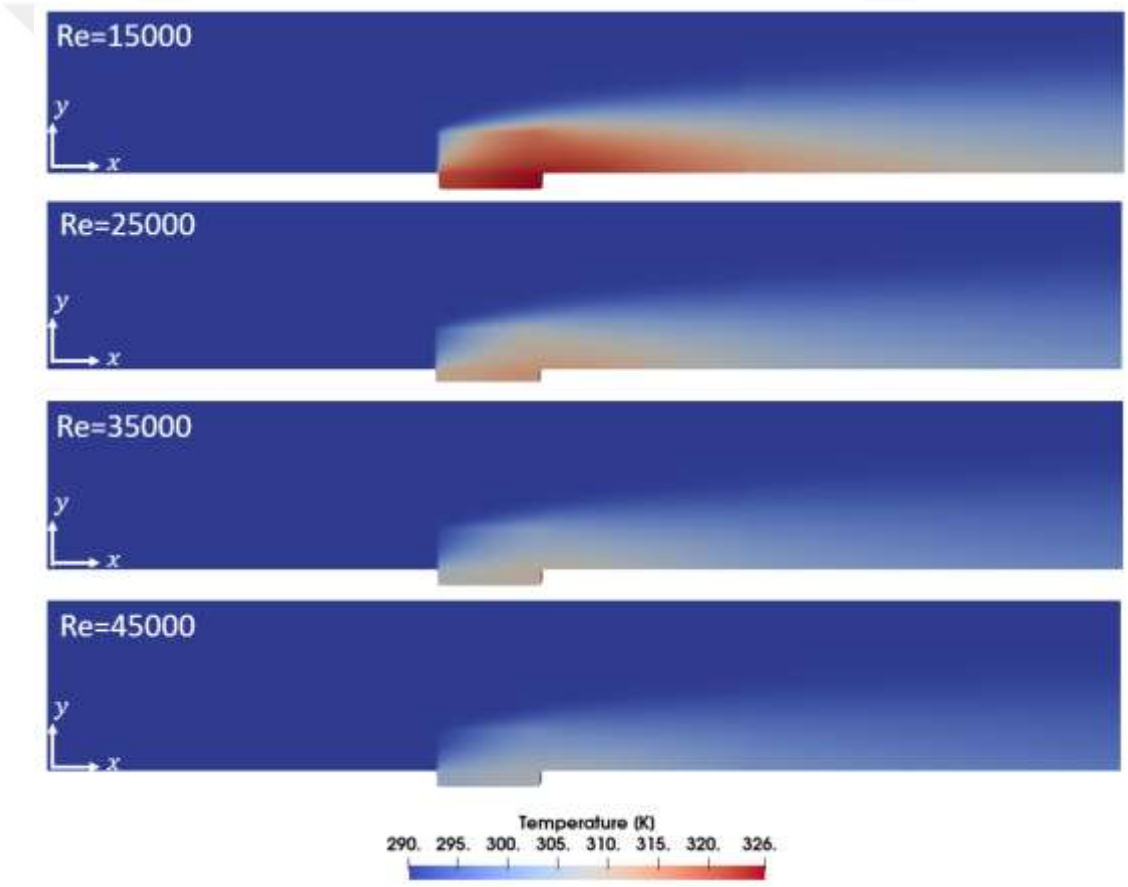

Figure 7.2: Temperature contours on vertical plane passing through z=10 mm in the (x-y plane) at different Reynolds numbers for *Q* = 18.3 W, *h/H*=0.064, φ=0.95, and *t/h*=2.5.

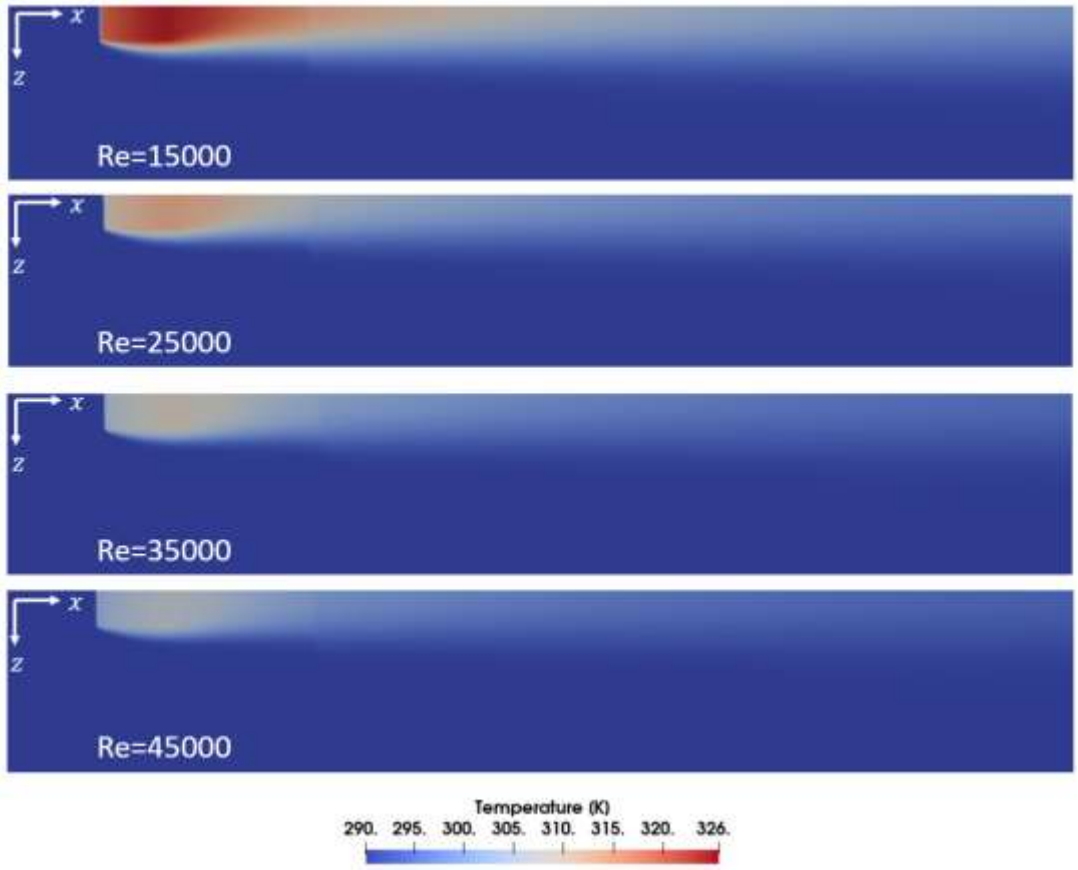

Figure 7.3: Temperature contours at horizontal plane passing through y=0 mm in the x-z plane (bottom view) for Q = 18.3 W, h/H=0.064, φ=0.95, and t/h=2.5 at different Reynolds numbers.

The Nusselt number variations with Reynolds number for different heat generation values are given in Fig. 7.4. As seen in these figures, as the Reynolds number increases, the Nusselt number also increases with a decreasing slope. It is noted that the heat generation rate has no effect on the Nusselt number, resulting in negligible differences in the Nusselt number for the same Reynolds number at each heat generation. As can be seen in the figure, the behavior of the Nusselt number variation does not show any difference in both calculation methods for Nu and Nu*.

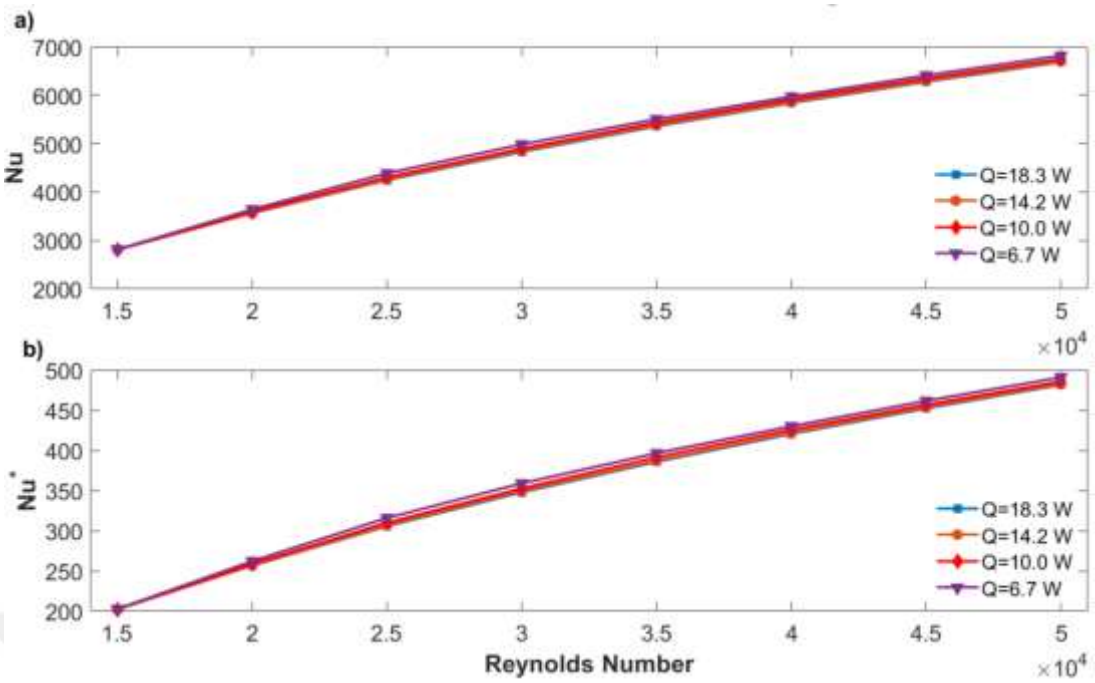

Figure 7.4: Variation of the Nusselt numbers with Reynolds number for different heat generation values at h/H=0.064, φ=0.80, and t/h=2.5, a) Nu-Re and b) Nu*-Re variations

7.2 THE EFFECTS OF POROSITY ON FLOW AND HEAT TRANSFER

Numerical analyses were carried out for different Reynolds numbers with porosity ranging between 0.55 and 0.98 to investigate the effect of porosity on heat transfer in the porous medium.

Figure 7.5 presents dimensionless velocity (u/u_∞) profiles cross different cross-sections of the channel for porosity values of 0.65, 0.75, 0.85, and 0.95 at Reynolds number of 20000, h/H=0.064, and t/h=2.5. In this figure it is seen that the flow reaches fully developed profile before reaching the block (x=-60 mm). As expected, for all the cases u/u_∞ velocity profiles are the same far from the block. However, at cross-sections close to the block (x=-20 mm), near the channel bottom surface, the velocity profiles differ from each other for different porosity values. These profiles clearly show that, in the porous layer velocity decreases and the decrease is higher for small porosity values. This is due to the decrease in permeability as the porosity decreases.

a)

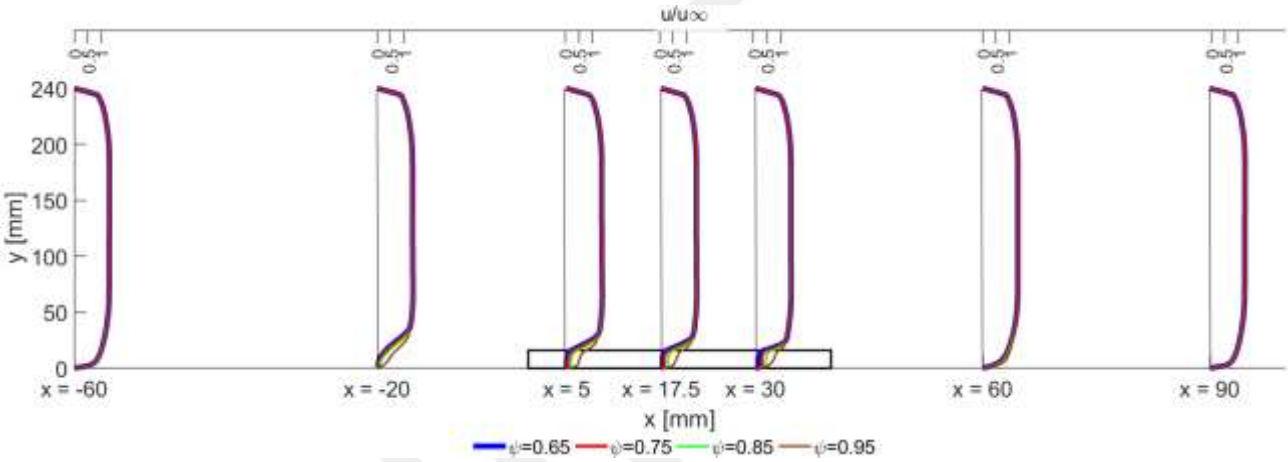

b)

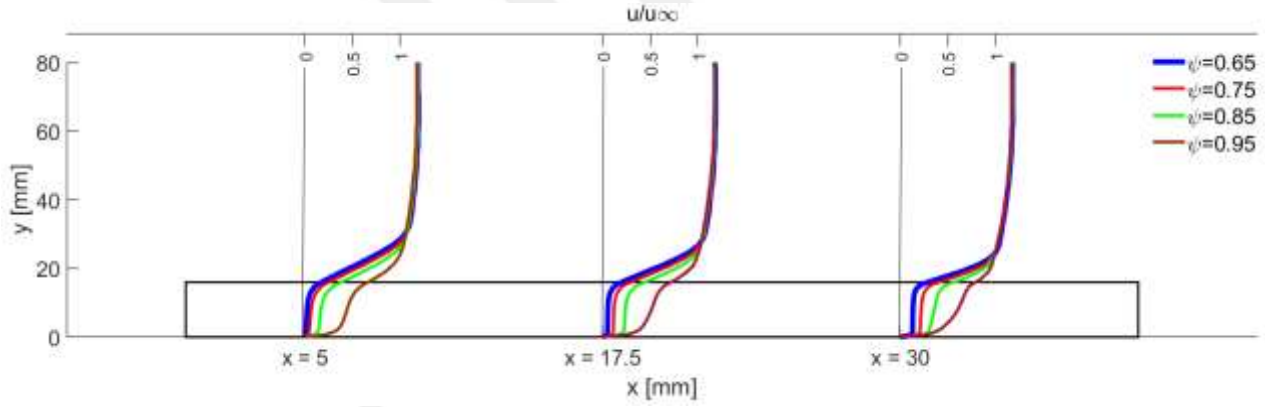

Figure 7.5: Dimensionless velocity (u/u_∞) profiles at different the cross-sections of the channel for different porosity values at Reynolds number of 20000, h/H=0.064, and t/h=2.5, a) general view and b) Close-up view in the porous medium.

Figures 7.6 and 7.7 illustrate the temperature contours in the vertical and horizontal planes, respectively, for different porosity values with a heat generation of 18.3 W, *h/H*=0.064, Re=20000, and *t/h*=2.5. The contours demonstrate that porosity has an important effect on the temperature field of the heated block. In the case of low porosity, the flow velocity decreases due to a decrease in permeability, which reduces the amount of heat transferred from the porous medium to the fluid and leads to higher temperatures in the porous medium and the heated block.

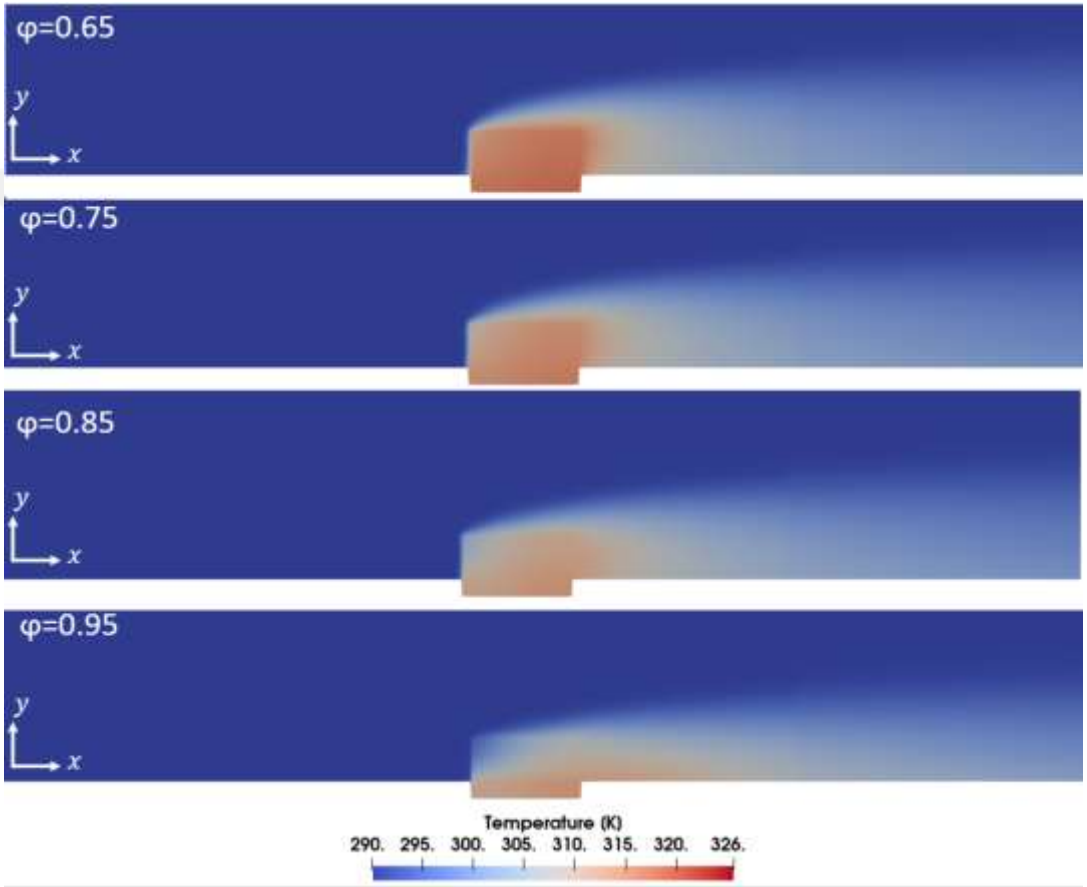

Figure 7.6: Temperature contours at vertical plane along the channel passing at z = 10 mm for different porosity values at Q = 18.3 W, h/H = 0.064, Re = 20000 and t/h = 2.5

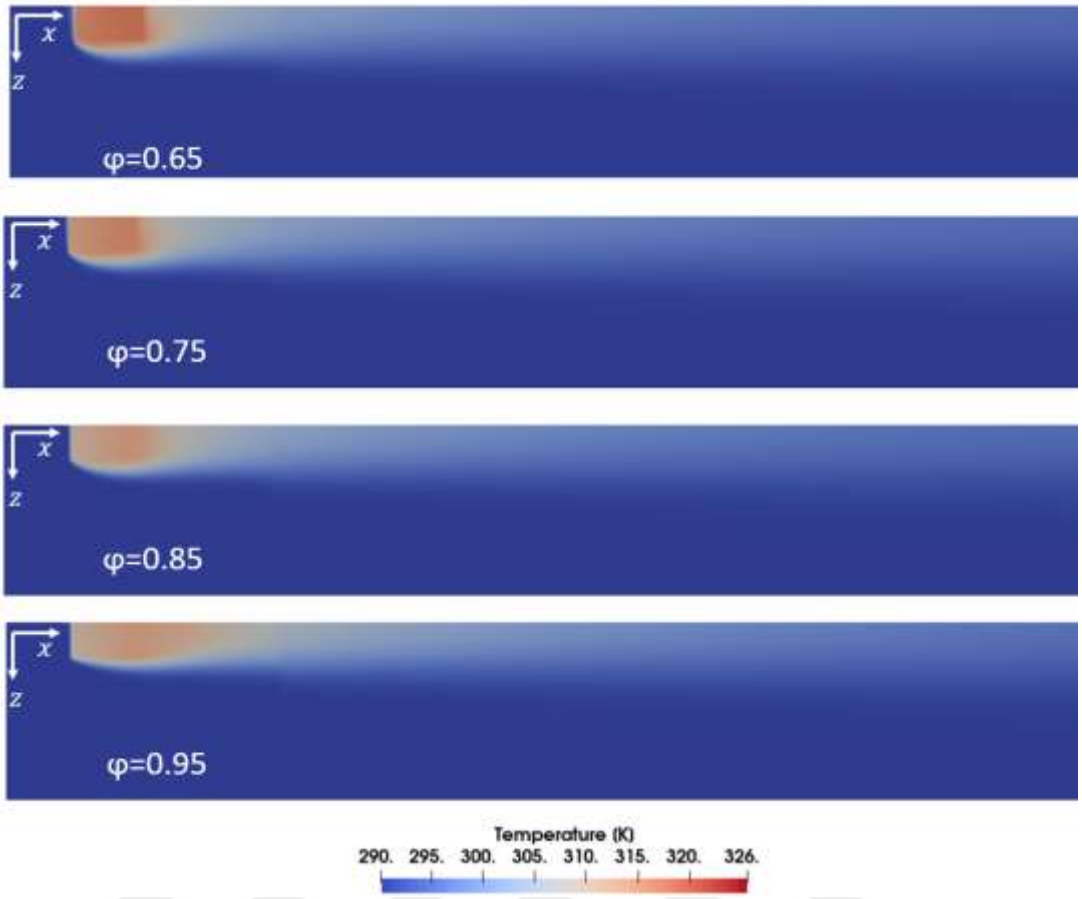

Figure 7.7: Temperature contours at horizontal plane at y=0 for different porosity values at Q = 18.3 W, h/H = 0.064, Re = 20000 and t/h = 2.5

Figure 7.8 presents the Nusselt- Number variation with Reynolds number for various porosity values. Like in the previous cases, it seen that the behavior of Nu and Nu* is similar here as well. Upon examination of this figure, it is observed that the Nusselt number increases approximately linearly with the Reynolds number for all porosity values. At low values of the Reynolds number (approximately Re < 25000), the Nusselt number increases with increasing porosity, but at high values of porosity (0.95), the slope of the Nusselt number decreases with increasing Reynolds number. Based on this result, it can be concluded that the optimal porosity value varies with the Reynolds number for maximum heat transfer. Within the range of Reynolds numbers examined, it was observed that the appropriate porosity value is between 0.85 and 0.95, and an investigation was conducted within these values. The resulting detailed e Nusselt number variations are shown in Figure 7.9.

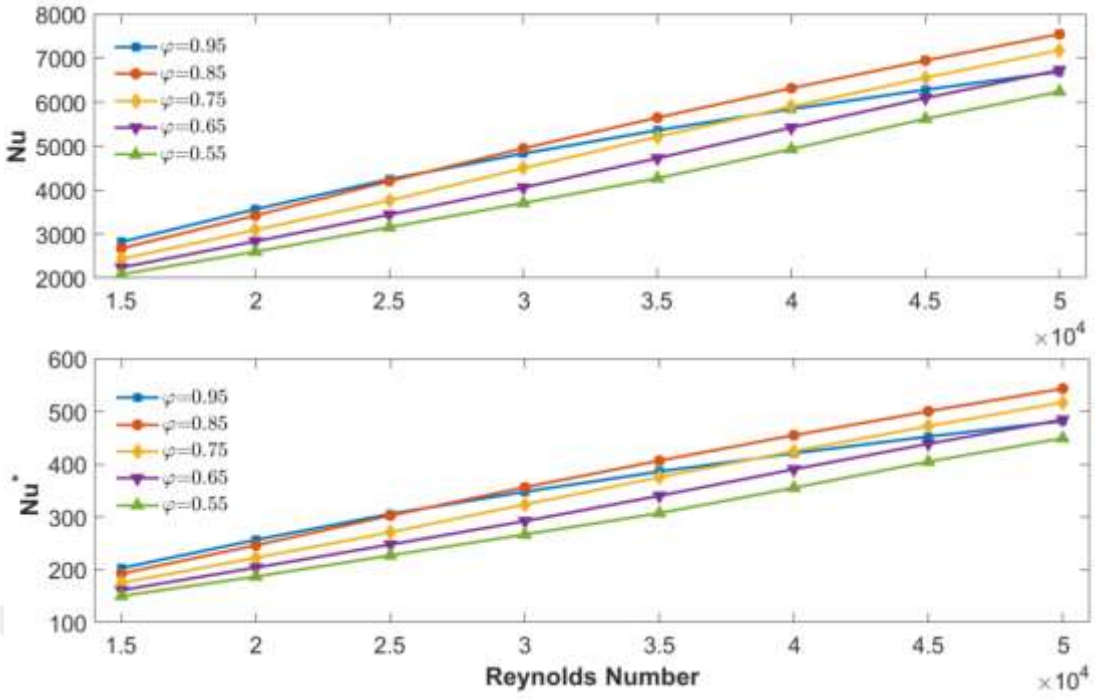

Figure 7.8: Nusselt variation with Reynolds number for different porosity values at Q = 18.3 W, h/H = 0.064, t/h = 2.5, a) Nu-Re and b) Nu*-Re

Upon examination of Fig. 7.9, it is observed that when the porosity is greater than 0.88 the Nusselt number does not change with changing porosity at a given Reynolds number, and particularly in the range of Re < 25000. As the porosity increases, permeability of the porous medium also increases, resulting in an increase in fluid velocity in the porous medium. However, an increase in porosity causes to a decrease in the heat transfer surface area. As a result, it can be stated that the optimum value of the porosity is different at different Reynolds numbers. For the Reynolds number range analyzed it may be concluded that the optimum porosity values is between 0.88-0.92.

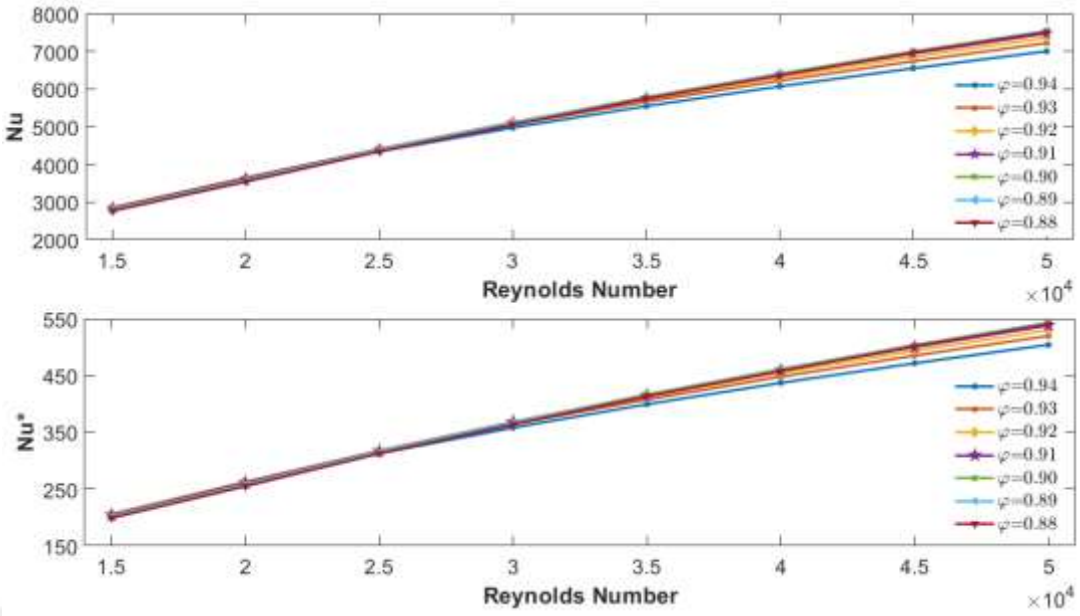

Figure 7.9: Variation of Nusselt number with Reynolds number for different permeability values in the range of φ = 0.88-0.94 at Q = 18.3 W, h/H = 0.064 and t/h = 2.5, a) Nu-Re and b) Nu*-Re

7.3 EFFECT OF POROUS MEDIUM HEIGHT-TO-CHANNEL HEIGHT RATIO ON FLOW AND HEAT TRANSFER

In order to investigate the effects of the porous medium height-to-channel height ratio (*h/H*) on heat transfer, analyses were carried out at different height ratios. Since the aim of this thesis study was to examine the effect of the porous medium on the cooling of electronic components, in this section, the height of the porous medium (*h*) was kept constant while the channel height (*H*) was reduced.

Figure 7.10 presents velocity profiles obtained for different *h/H* ratios for a Reynolds number of Re = 25000, porosity of φ = 0.85, and a heat generation of *Q* = 18.3 W. Since the Reynolds number is kept constant, the flow velocities increase in all of these analyses as the *h/H* ratio increases (hydraulic diameter decreases). Upon examination of the figure, it can be seen that fully developed flow conditions are achieved for all *h/H* ratios at the channel inlet. In the porous medium, it is observed that the velocity of the fluid decreases as it progresses compared to the free stream region. Figure 7.10b provides a focused view of the velocity profiles in the porous medium. Upon examination of this figure, it is clearer that as the *h/H* ratio increases, the u/u_∞ value in the free stream region rises well above 1. Under constant fluid flow rate, as the channel height decreases, the free stream region velocities increase up to

1.2 times. It has also been observed that as the *h/H* ratio increases, the u/u_∞ value increases in the porous medium.

a)

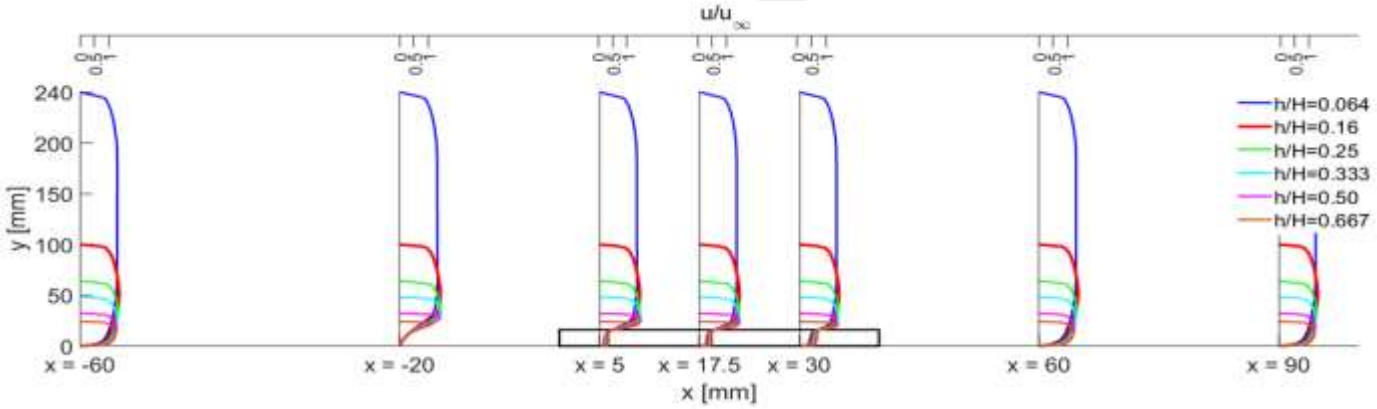

b)

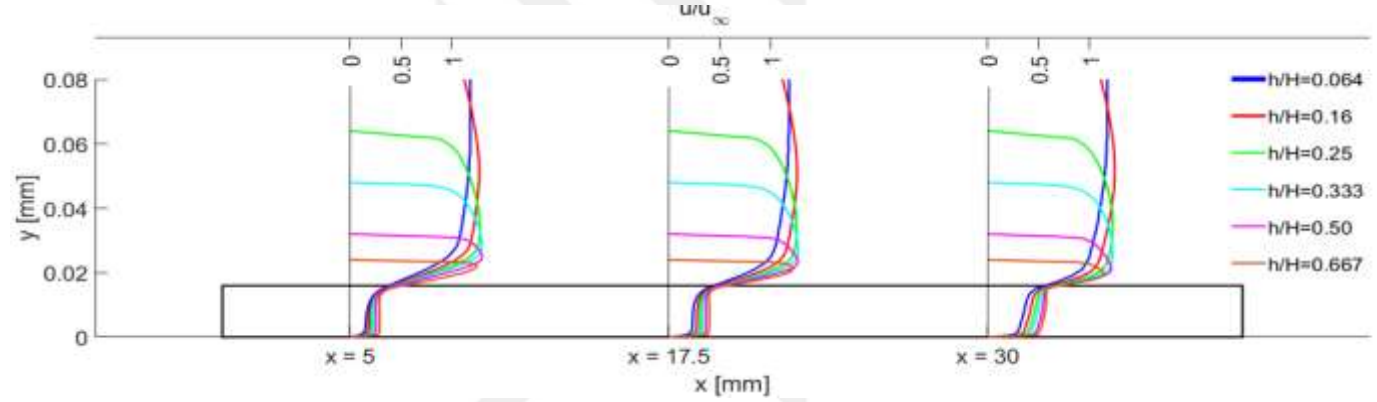

Figure 7.10: Velocity profiles for different *h/H* ratios at Re=25000 a) general view and b) close up view of porous medium

Temperature contours for different *h/H* ratios are presented in Fig. 7.11 and Fig. 7.12 for a heat generation of Q = 18.3 W, a porosity of φ = 0.85, a fluid velocity at the channel inlet of u_∞ = 3.20 m/s, and a *t/h* ratio of 2.5. The fluid velocity defined at the channel inlet is the same for all three analyses. Therefore, the Reynolds numbers are different. Upon examination of the contours, there is no noticeable difference in the temperature contours in the heated block and porous medium regions due to the same flow velocity. However, it has been observed that the average fluid temperature at the channel outlet increases as the *h/H* ratio increases.

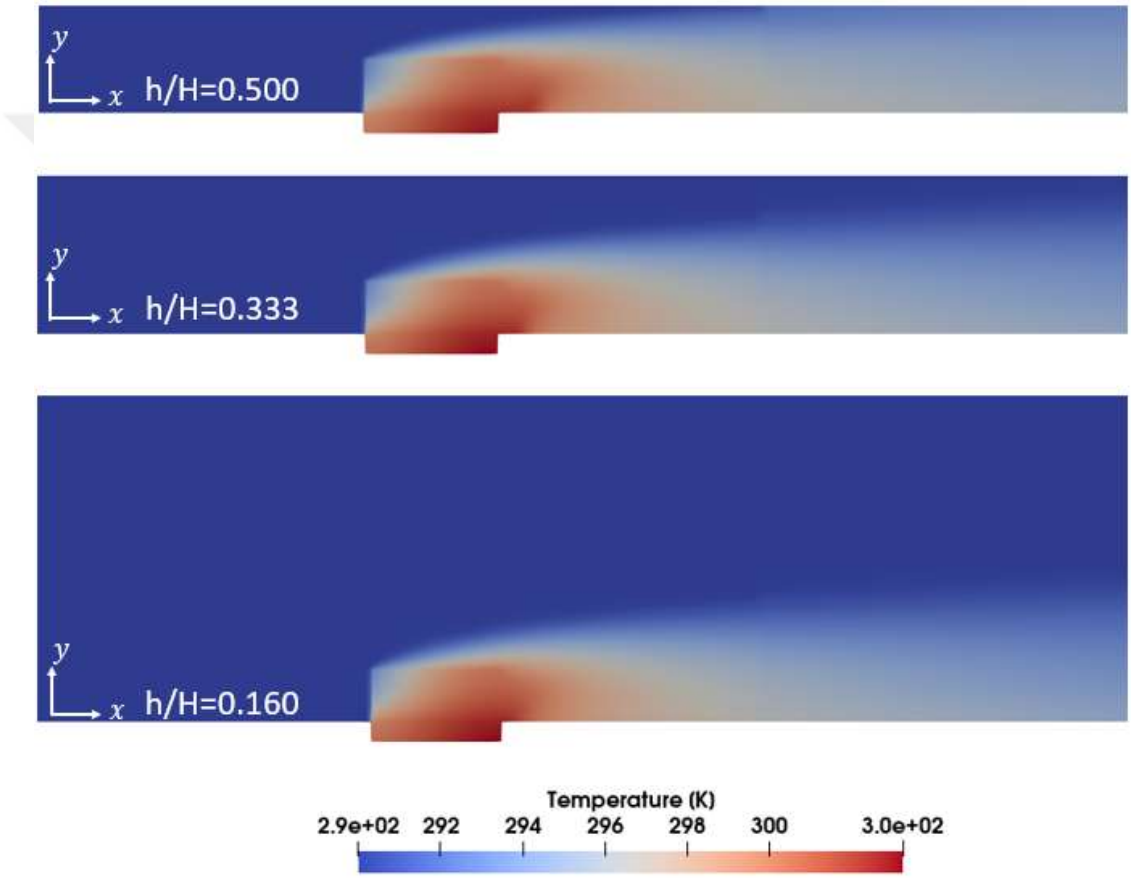

Figure 7.11: The temperature contours obtained at z=10 mm in the x-y plane (side view) for different *h/H* ratios and Q = 18.3 W, φ=0.85, u_∞=3.20 m/s and *t/h*=2.5

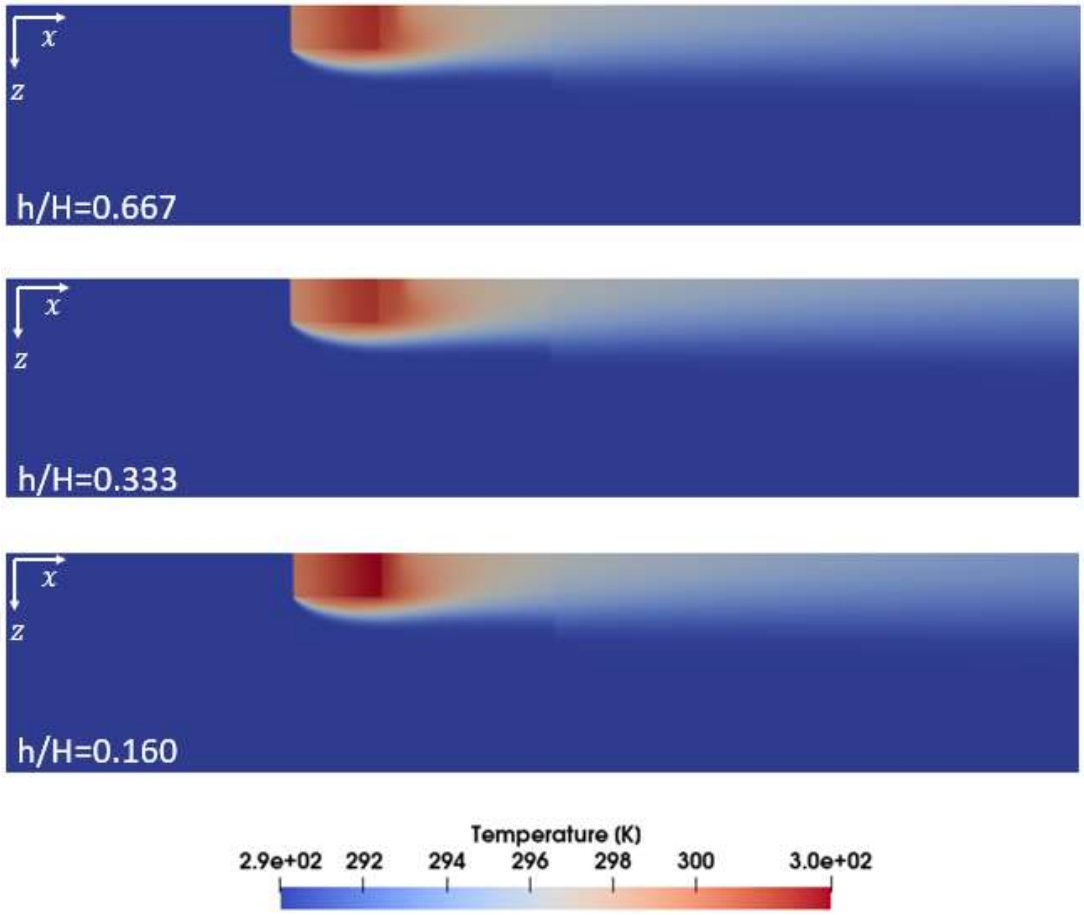

Figure 7.12: The temperature contours obtained at z=10 mm in the x-z plane (bottom view) for different *h/H* ratios and *Q* = 18.3 W, φ=0.85, u_∞=3.20 m/s and *t/h*=2.5

Figure 7.13 illustrates the variation of the local heat transfer coefficient along line **ab** the surface where the heated block contacts the porous medium (z = 0.01 mm). Upon examination of the figure, it can be seen that the heat transfer coefficient on the block surface facing the porous medium is decreasing from the upstream side (point **a**) to the downstream side . In different *h/H* ratios, the local heat transfer coefficient increases in all cases considered as the flow velocity increases with increasing *h/H* ratio (decreasing channel height, *H*). The average heat transfer coefficient shown in Fig. 7.14 also increases as *h/H* increases in all Reynolds numbers considered.

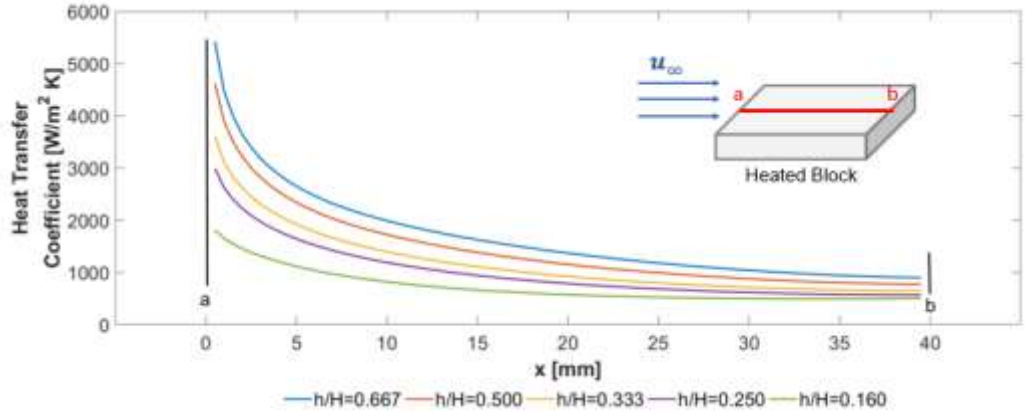

Figure 7.13: The local heat transfer coefficient variation along the line a-b on the surface of the heated block in contact with the porous medium

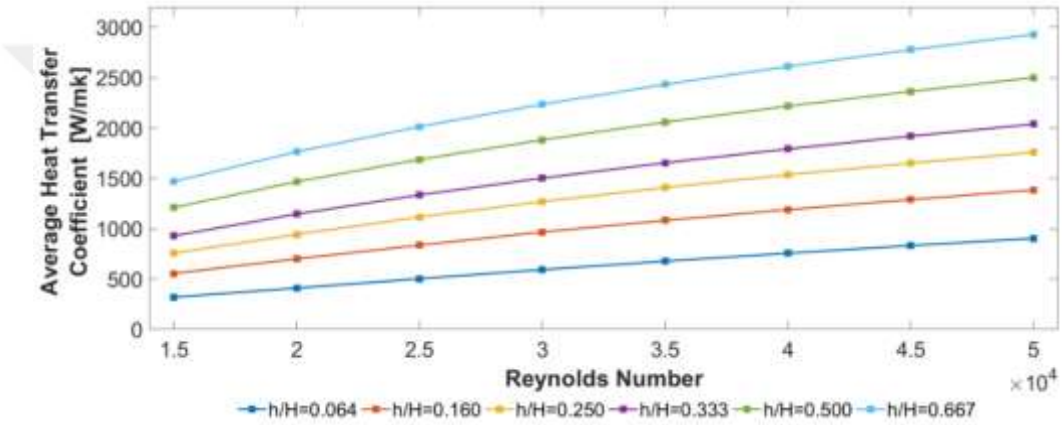

Figure 7.14: The variation of average heat transfer coefficient with Reynolds number for different *h/H* ratios, with Q = 18.3 W, φ=0.85 and *t/h*=2.5.

Figure 7.15 shows the Nusselt number-Reynolds number graphs for different *h/H* ratios. Upon examination of the graph, it can be seen that although the heat transfer coefficient increases, the Nusselt number decreases as the *h/H* value increases. This is due to the D_h parameter included in the Nusselt number formulation. When the effect of the *h/H* ratio on heat transfer is examined, changing the channel height H value also causes the hydraulic diameter D_h value to change. As the channel height decreases, the fluid velocity increases, and the heat transfer coefficient also increases. However, the hydraulic diameter value also decreases as the channel height decreases. For example, when the *h/H* is increased from 0.2 to 0.25 for Re = 25000 and φ = 0.85, the hydraulic diameter value decreases from 0.11428 to 0.0969, a 15% decrease, while the heat transfer coefficient increases from 974 W/mK to 1116 W/mK, a 13.6% increase. Since the proportional change in the hydraulic diameter is larger than the average heat

transfer coefficient, the Nusselt number decreases as the *h/H* increases as seen in Fig. 7.15a.

However, in the calculation of Nu*, the height of the porous material replaces the hydraulic diameter in the formulation. Therefore, the effect of the hydraulic diameter on the Nusselt number does not exist. When Fig. 7.15b is examined, as expected, Nu* is high in cases where the heat transfer coefficient is high. Also, the behavior of the curves is again similar to the heat transfer coefficient.

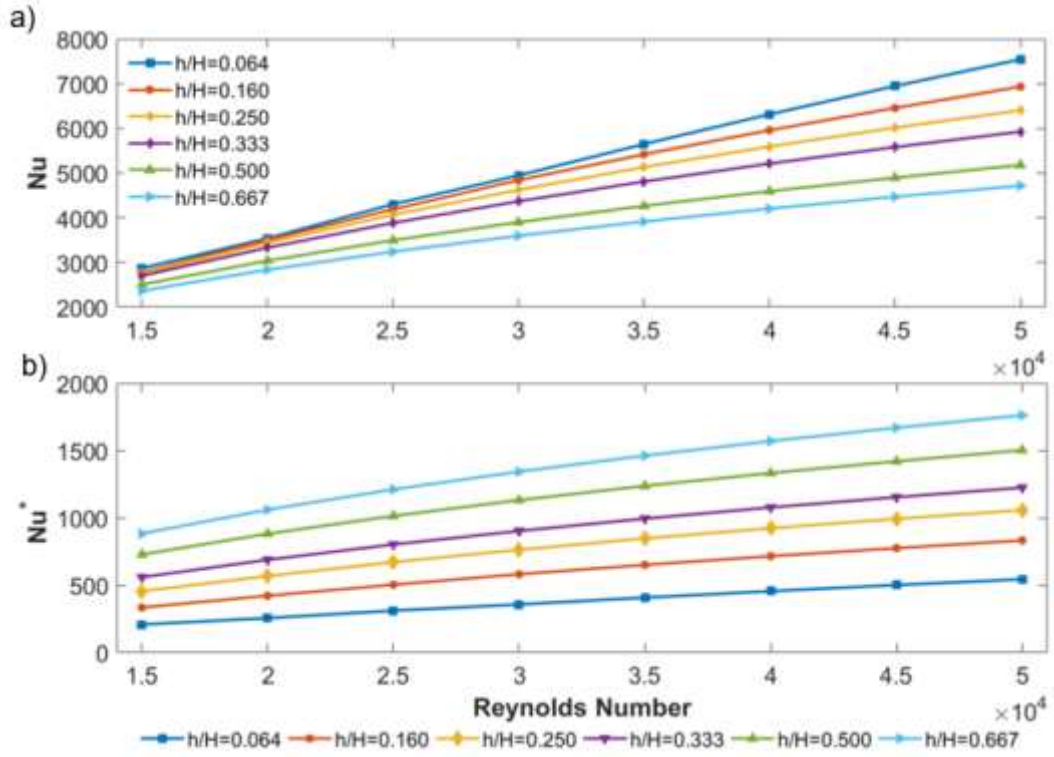

Figure 7.15: Nusselt number - Reynolds number graph for different *h/H* ratios for *Q* = 18.3 W, φ=0.85 and *t/h*=2.5, a) Nu-Re and b) Nu*-Re

7.4 EFFECTS OF THE RATIO OF POROUS MEDIUM WIDTH TO HEIGHT (T/H) ON FLOW AND HEAT TRANSFER

Numerical analyses were carried out with different porous layer width while keeping the height constant in order to study the effect of the ratio of porous medium width to height (*t/h*) on flow and heat transfer. In these analyses, the width of the heated block was also varied as the porous medium width. In previous analyses, heat generation (*Q*) values were defined as boundary conditions by calculating the heat flux to the lower surface of the heated block. However, since the surface area where the boundary condition is defined also changes with the width of the medium, using a

constant heat generation value in the analyses would result in variable heat flux values, making it difficult to compare the temperature contours. It was previously determined that heat generation values do not affect the Nusselt number in Fig. 7.4. Therefore, in order to better examine the effect of porous medium width on heat transfer, the heat flux value defined on the lower surface of the heated block for a heat generation value of 18.3 W (q" = Q/A_s = 11426 W/m^2) calculated in previous analyses was kept constant in all analyses here.

Figure 7.16 presents the velocity profiles obtained for Re = 25000, φ = 0.95, and h/H = 0.16. When the figure is examined, it can be seen that the porous medium width has no effect on the velocity profiles in the x-y plane.

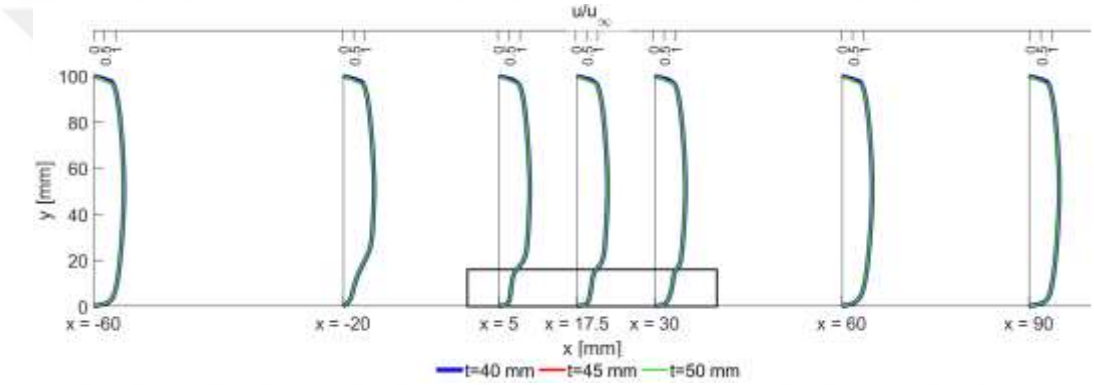

Figure 7.16: Velocity profiles obtained at z = t/2 for different t/h ratios when the constant heat flux (q" = 11426 W/m^2) and Re = 25000, φ = 0.95, and h/H = 0.16.

The temperature contours depicted in Fig. 7.17 were obtained for various t/h ratios and a constant heat flux condition with h/H = 0.064, Re = 20000, and φ = 0.95. Analysis of the contours reveals that the width of the porous medium does not significantly affect the temperature values. The main reason is that the heat flux value defined on the heated block bottom surface is kept constant. As the base area of the heated block increases, the amount of heat supplied to the system also increases in the same proportion due to the constant heat flux, and it is seen that the width of the porous medium does not affect the temperature values in the temperature contours.

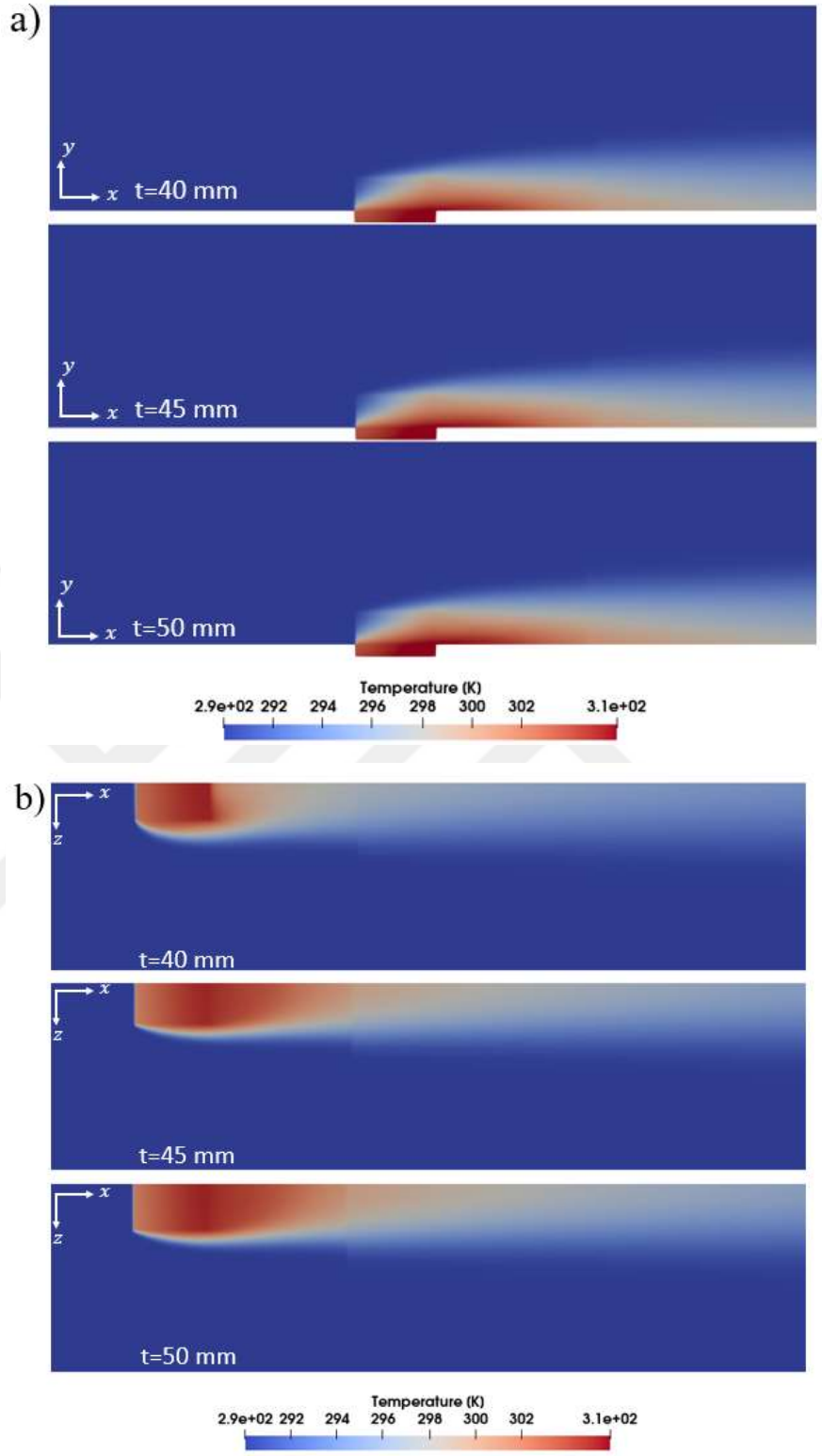

Figure 7.17: Temperature contours obtained for different t/h ratios when the constant heat flux value (q" = 11426 W/m2) and Re = 25000, φ = 0.95, and h/H = 0.16, a) xy-plane (side view) z = 0.01 m, b) xz-plane(bottom view) y = 0

The graph shown in Fig. 7.18 indicates that the both Nu and Nu* values remain relatively unchanged for a given Reynolds number when four different widths of

porous medium are employed. This observation demonstrates that the width of the porous medium has a minimal effect on the Nusselt number.

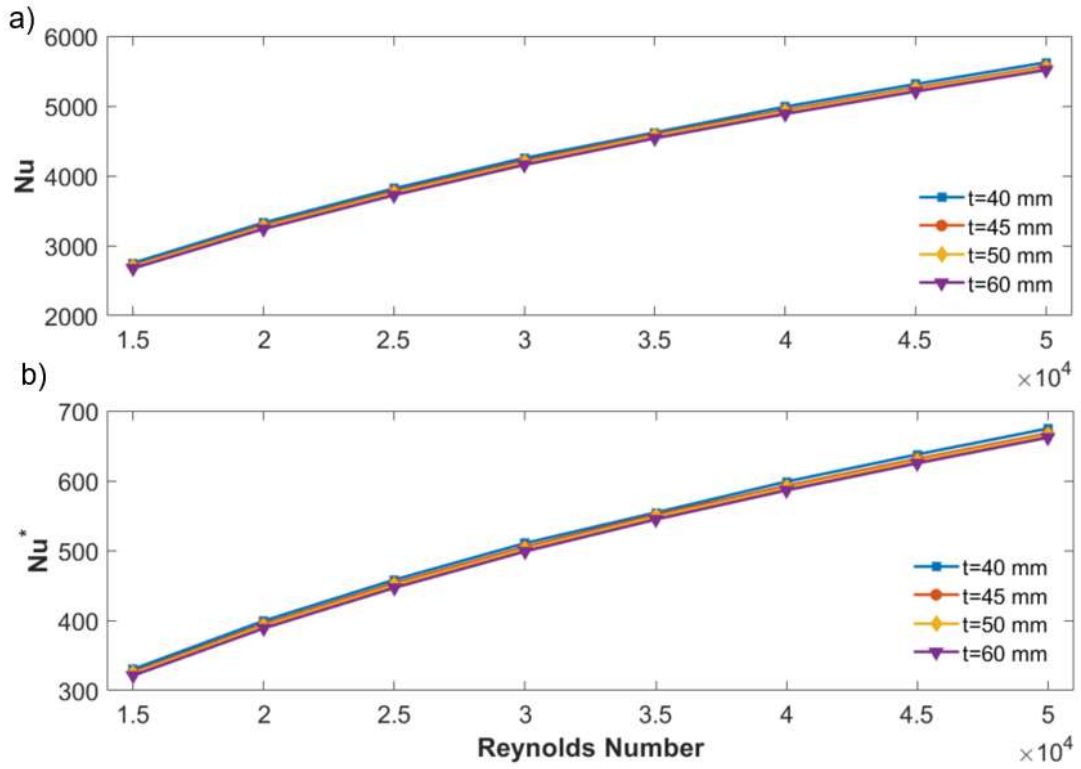

Figure 7.18: Variation of the Nusselt number obtained for different porous medium widths at h/H = 0.16, Re = 20000, and φ = 0.95 as a function of the Reynolds number, a) Nu-Re and b) Nu*-Re

CHAPTER VIII
CORRELATION DEVELOPMENT AND ARTIFICIAL NEURAL NETWORK ANALYSIS

In this section, using the data obtained from the numerical and experimental studies, a Nusselt number correlation equation is developed, and an artificial neural network architecture is created to obtain more accurate Nusselt number estimations for different cases. Within this scope, first, the parameters affecting heat transfer are determined. The parameters are non-dimensionilized by subjecting them to dimensional analysis. The coefficients of the correlation equation, validation points, and errors are determined using a Matlab code. Since the correlation equation obtained in polynomial form resulted in a high error, an exponential regression function was developed. The correlation coefficients were determined with the help of logarithmic transformation. Also, an Artificial Neural Network (ANN) architecture was developed using the data obtained from the experimental and numerical studies. In this stage, the physical constraints and variables of the parameters necessary for the model formulation were determined. Then, the structure of the learning schemes to be used in the ANN algorithm is selected by defining the test data and determining the number of layers of the neural network. Finally, the accuracy of the resulting model is tested by error analysis studies.

8.1 CORRELATION DEVELOPMENT

Statistical techniques are used when the interactions between variables cannot be expressed analytically. The statistical technique used to explain the relationship between variables that are not affected by any factor (independent variable) and variables that are affected by the changes in other parameters (dependent variable) is called curve fitting. Regression and interpolation are approaches used for curve fitting. Which of these will be applied to the given data set of interest is determined by the error rates. The regression approach is used if the error rate of the data values is high and the curve to be created will not pass through each data point but will only be

formed according to the general trend of the data. If the error is small and if the generated curve is to pass through all data points, interpolation approach is utilized (Bingham and Fry 2011)

One of the methods used to find the regression coefficients is the least squares method. It is aimed to minimize the difference between the estimation of the function and the actual values given as a data set. The coefficients are determined such that the sum of the squares of the errors are minimum. This method can be used for linear, polynomial and exponential curve fittings.

In regression analysis, first, classification is made according to the number of independent variables. If there is only one independent variable, simple regression is applied, if there are two or more variables, multiple regression analysis is applied. In the studies conducted in this thesis, there are more than one independent variables, therefore multiple regression analysis was applied.

Correlation analysis is used when deciding on the types of parameters in the data set: whether they are dependent or independent, or whether these parameters should be considered together in the regression set. Since the curve to be obtained must be an approximate function representing the given data set in terms of independent variables, it is very important to know whether there is a relationship between the variables. For the relationship between the variables, the correlation of each variable with the others should be checked, therefore the correlation coefficient (R) should be calculated (Draper and Smith, 1998). Correlation coefficient varies between -1 and 1. In Table 8.1, correlation coefficient limits and their meanings are given.

Table 8.1: Limits of the correlation coefficient values (Tamil 2022)

Range of the R value	**Meaning**
R>=0.8	Very strong correlation
0.6<=R<0.8	Moderately strong correlation
0.3<R<0.6	Fair correlation
R<=0.3	Poor correlation

If the value of the correlation coefficient is 0.3 and below, there is no need to consider the variables together. On the contrary, for the variables with R>0.3, using the variables together increases the accuracy of the regression equation (Tamil 2022). The process diagram that is used in this study for developing the correlation equation is shown in Fig. 8.1.

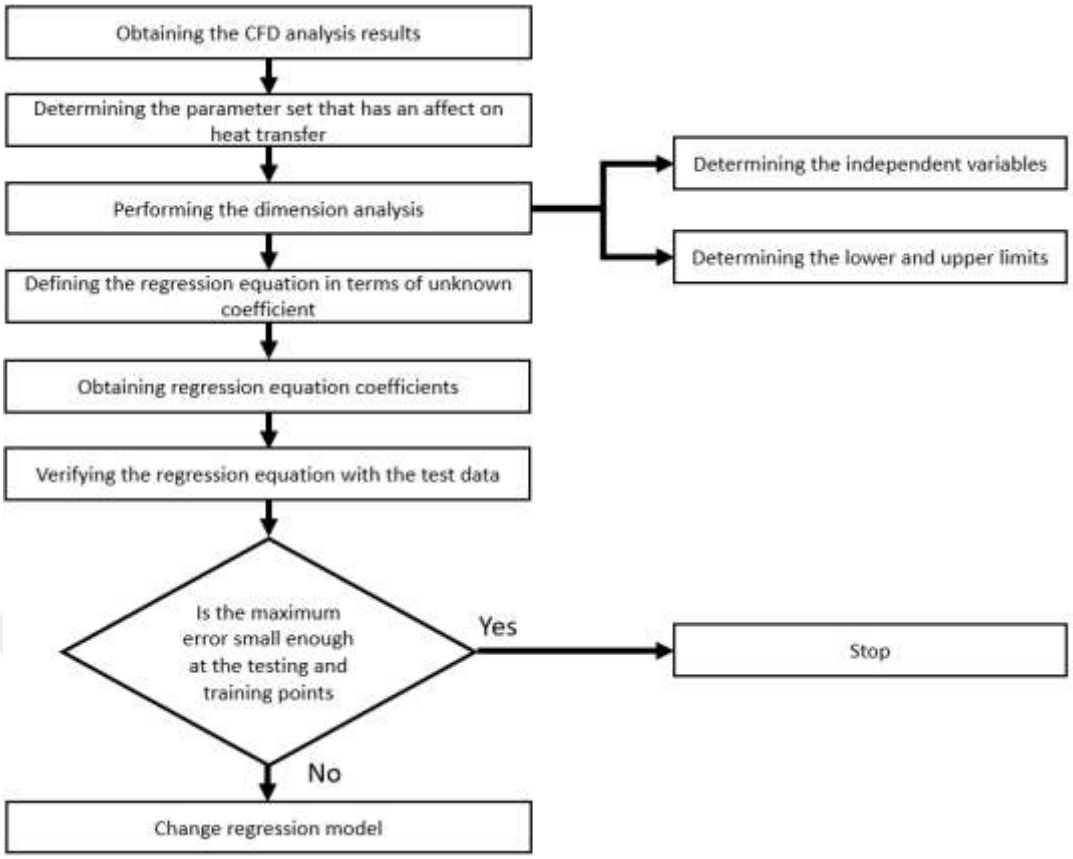

Figure 8.1: Flow chart of the correlation development process.

Correlation equations are usually expressed by low-grade polynomials. In particular, the second degree polynomial correlation model is flexible, easy and parameter estimation is high in accuracy, which is sufficient in many problems.

A general polynomial correlation equation can be written as

$$y = \hat{y} + \epsilon \tag{8.1}$$

$$\hat{y} = \beta_0 + \sum_{i=1}^{N} \beta_i x_i + \sum_{i=1, i<j}^{N} \sum_{j=1}^{N} \beta_{ij} x_i x_j + \sum_{i=1}^{N} \beta_{ii} x_i x_i \qquad i, j = 1, \ldots\ldots N \tag{8.2}$$

In above equations, y denotes the value given as the data set, $\hat{y}$ is the value calculated from the correlation and ε is the error (difference between the data and the corresponding value calculated from the correlation.). Equation 8.2 shows the second order polynomial correlation model to be used as the correlation model. In this equation, β*'s* are the correlation coefficients and x_i represent independent variables.

The data obtained from the numerical analysis were used in a program developed at MATLAB platform and the correlation coefficients, and error rates were obtained.

8.1.1 Error Analysis of Correlation Equation

The error analysis of the correlation equation is performed by comparing the Nusselt number calculated from CFD analysis and experimental studies at data points with the results obtained from the correlation equation developed. Different equations are used in the literature for error analyses. The most commonly used equation is the Root Mean Square Error, given below:

$$\text{Root Mean Square Error}(\ \text{RMSE}_n) = \sqrt{\frac{1}{N}\sum_{i=1}^{N}\left(\frac{y_i - \hat{y}_i}{y_i}\right)^2} \qquad (8.3)$$

where N is the number of verification points, y_i represents the actual value at each verification point and $\hat{y}_i$ represents the calculated correlation output value at each of these points. The error value squared in this method is divided by the number of data. This enables the determination of the average error. Taking a square of the error value prevents the difference from being negative or positive, mathematically affecting the result.

To find the maximum deviation value of the correlation equation in percentage, the Eq. 8.4 is used. This predicts the maximum amount of errors in the results from the model used.

$$\text{Maximum Absolute Error} = \max_{i=1,\ldots n}\left(\frac{|y_i - \hat{y}_i|}{y_i} \times 100\right) \qquad (8.4)$$

Using Eq. 8.5, the mean absolute error can be calculated.

$$\text{Average Absolute Error} = R = \frac{1}{N}\sum_{i=1}^{N}\left|\frac{y_i - \hat{y}_i}{y_i}\right| \qquad i = 1, \ldots \ldots . n \qquad (8.5)$$

8.1.2 Developing Correlation Equation for Nusselt Number

By determining the parameters affecting the Nusselt number in the pipe with the help of the previous section, a CFD-based regression model can be created within certain limits. As in most real applications, since the real response function is not fully known, an approximate response function can be obtained by regression modeling.

For this purpose, first, the parameters are selected and non-dimensionalized, and correlation analysis is performed to ensure that the parameters are not dependent on each other. Then the lower and upper bounds of the parameters are determined and a data set is created within the limits. Multi-variable regression models are established using the data set obtained and the accuracy of these models is compared by examining the error rates.

Determining the Parameters Affecting the Nusselt Number

The Nusselt number is a dimensionless number used in convective heat transfer analysis. The Nusselt number is the ratio of heat transfer by convection to the heat transfer by conduction within a fluid. Based on the CFD analysis performed with the OpenFOAM program, the parameters that affect the Nusselt number are determined as Reynolds number, Darcy number, porosity and geometrical dimensions. Of these parameters, Re, Da, porosity and geometrical parameters are independent variables, and Nusselt number is dependent variable.

Dimensional Analysis

Dimensional analysis is a widely used tool for the determination of dimensionless parameters. After the variables affecting any physical system are grouped as dependent or independent variables, they are reduced to dimensionless terms (π terms) so that all variables are dimensionless.

To find the dimensionless groups, π theorem is commonly used. In applying the π theorem, the following steps are followed (Fox and McDonald 2009):

Step 1: Listing all variables involved in the problem and expressing each of the variables in terms of basic dimensions: In Table 8.2, variables of the problem and their dimensions are given.

Table 8.2: The variables affecting the heat transfer coefficient.

Type of Variable	Symbol	Definition of Variable	Dimension	Unit
Dependent	h	Heat transfer coefficient	M/Tt^3	$[kg/Ks^3]$
Independent Variables	μ	Absolute Viscosity	M/Lt	[kg/ms]
	ρ	Density	M/L^3	$[kg/m^3]$
	D_h	Hydraulic diameter	L	[m]
	C_p	Heat Capacity	ML^2/t^2T	$[kgm^2s^{-2}K^{-1}]$
	V	Velocity	L/t	[m/s]
	K	Permeability	L^2	$[m^2]$
	k	Thermal conductivity	ML/t^3T	$[kgm/s^3K]$
	T	Temperature	T	[K]

Step 2: Determining the required number of π terms: Number of variables (*n*) are set. In the present problem, it is 9. Then the number of primary dimensions is determined which is four for the present problem (L, M, t and T). Therefore, the number of π terms (dimensionless groups) is determined as 9-4=5 for this problem.

Step 3: Selecting number of repeating variables: ρ, D_h, V and k are chosen as repeating variables. Number of repeating variables should be equal to the number of primary dimensions appear in the dimensions of the variables of the problem.

Step 4: Forming pi term: In order to determine pi terms, the repeating variables are grouped with remaining variables in turn in the dimensionless form. First, the dependent variable heat transfer coefficient, h is grouped with the repeating variables (*ρ*, D_h, *V* and *k)* as follows:

$$\pi_1 = h\rho^a V^b {D_h}^c k^d$$

$$M^0L^0t^0T^0 = M^1T^{-1}t^{-3}M^aL^{-3a}L^bt^{-b}L^cM^dL^dt^{-3d}T^{-d}$$

$$\pi_1 = \frac{hD_h}{k} = Nu$$

Remaining Pi terms can be determined using the same method. Grouping the variables μ, T, c_p, and *K* with the selected repeating variables in a similar manner, the following Pi terms are obtained:

$$\pi_2 = \frac{\mu}{\rho V D_h} = \frac{1}{Re}$$

$$\pi_3 = \frac{T\ k}{\rho\ V^3\ D_h}$$

$$\pi_4 = \frac{C_p\ \rho\ V\ D_h}{k}$$

$$\pi_5 = \frac{K}{D_h^2} = Da$$

If we multiply π_3 and π_4 with π_2, Prandtl number and Brinkman number can be obtained.

$$\pi_2 \times \pi_3 = \frac{T\ k}{\mu\ V^2} = \frac{1}{Br}$$

$$\pi_2 \times \pi_4 = \frac{\mu\ C_p}{k} = Pr$$

It is seen that the obtained dimensionless groups show that the Nusselt number is dependent on Reynolds number, Darcy Number, Brinkman Number, and Prandtl number. In all the analyses carried out, the Prandtl number was kept constant. Therefore, in the correlation developed in this study Prandtl number is excluded. The Brinkman number can be used to measure the ratio between the heat generated from viscous heating and the heat exchanged at the wall for laminar flow. (Coelho and Pinho 2009). Since the problem considered in this study involves turbulent flow, it is therefore not applicable to our problem and thus it is not necessary to include it in the correlation equation.

In addition to the Nusselt, Reynolds and Darcy numbers, the ratio of the porous medium height to channel height (*h/H)* was added as a dimensionless geometric parameter to the list of independent parameters. Also, porosity (φ), which is the ratio of fluid volume to whole volume, was used in the correlation equation. Hence a functional relation between the dimensionless numbers can be written as,

$$Nu = f\left(Re, \varphi, \frac{h}{H}, Da)\right)$$

8.2 DETERMINATION OF CORRELATION EQUATION

As shown above, under steady turbulent flow conditions, the Nusselt number for heat transfer thorough a porous layer is dependent on Reynolds number (*Re)*, Darcy number (*Da*), ratio of the height of the porous medium to the channel height (*h/H)*, and porosity (φ).

$$Nu = f\left(Re, Da, \frac{h}{H}, \varphi\right) \tag{8.6}$$

A mathematical relationship for the Nusselt number can be expressed by the following equation.

$$Nu = aRe^{b}Da^{c}\varphi^{d}\left(\frac{h}{H}\right)^{e} \tag{8.7}$$

where, *a* is an unknown coefficient, and *b*, *c*, *d* and *e* are unknown exponents. Taking the logarithm of both sides of the above equation, we obtain the following expression:

$$logNu = loga + blog(Re) + clog(Da) + dlog(\varphi) + elog\left(\frac{h}{H}\right) \tag{8.8}$$

The 460 numeric analysis and 16 experimental analysis performed yielded results that enabled the development of a correlation equation utilizing the least squares linear regression method. Utilizing the least-squares linear regression method, the unknowns were determined and the correlation equation for Nusselt number is obtained as,

$$Nu = 1.2733Re^{0.74}Da^{-0.1378}\varphi^{1.8798}\frac{h}{H}^{-0.1197} \tag{8.9}$$

This correlation is valid for air (Pr=0.7) between the values of parameters in the following intervals:

$$\begin{cases} 15000 < Re < 50000 \\ 0.55 < \varphi < 0.95 \\ 0.064 < \dfrac{h}{H} < 0.5 \\ 0.001 < Da < 0.15 \end{cases}$$

A comparison of Nusselt numbers calculated from the developed correlation equation (Eq. 8.9) and the Nusselt numbers obtained from numerical solutions and experimental results are given in Fig.8.2. The absolute average deviation between the correlation equation and numerical results is 8.82%, and the maximum error is 16.79%. The root-mean-square deviation (RMS) between values calculated from the generalized correlation equation and the values obtained from numerical results is around 0.78 %.

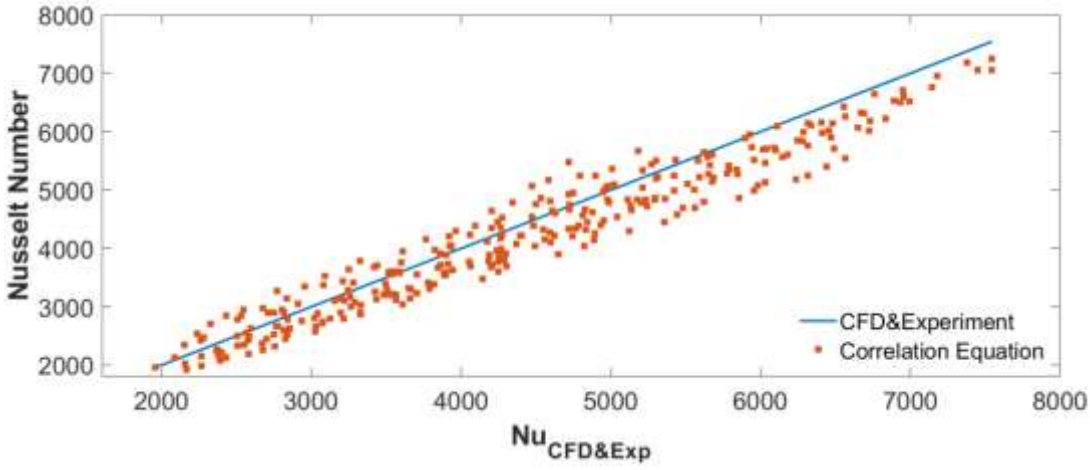

Figure 8.2: Correlation curve compared to numerical and experimental data.

8.3 ARTIFICIAL NEURAL NETWORKS

In the final phase of the thesis study, an Artificial Neural Networks (ANN) model is developed using the data obtained from the experimental and numerical studies. In this stage, it is necessary to determine the physical constraints and variables of the parameters required for the formulation of the model. Then, the structure of the learning schemes to be used in the ANN algorithm is created by defining the test data and determining the number of layers of the neural network. Finally, the accuracy of the resulting model is tested with error analysis studies.

Artificial neural network models do not need to follow a mathematical theory to be able to compute (Haykin 1998). Instead of following a mathematical model,

ANNs reach the required output values with their own learning algorithms. Therefore, no theoretical knowledge is required to train artificial neural networks. Instead of theoretical knowledge, data sets are required. Moreover, when the same problem or structure produces different results over time, ANNs can be re-trained to adapt to the system. All of these abilities are also valid for problems with nonlinear, multi-dimensional, or incomplete data. Therefore, they are practical and economical. However, there is no fundamental rule for the selection of the training model and the determination of the topologies of the networks. The correct selections are completely dependent on the user experience. Moreover, they need many data to predict all the behavior patterns of the problem in nature. Since it only works with numerical data, it is extremely important to evaluate the input and output of the problem on numerical values. Like in regression equations, it does not show the effect of the input parameters on the output. Artificial neural networks are closed systems to the outside world and the behavior of the network cannot be explained. Therefore, artificial neural networks do not provide any clues as to how and why they produce solutions to a problem (Haykin 1998).

The gathering of artificial neurons creates neural networks, which have an architecture similar to the human brain. In neural networks, each neuron is a processing unit and is connected to other neurons by weighted links. Information is transferred from the input layer to the hidden layers and finally to the output layer through these links. Each neuron receives multiple inputs and generates an output according to a certain function. This function is called the activation function. The weights of the links are adjusted during the training phase of the neural network according to a certain learning algorithm. As a result of this process, the network produces the desired output for the given input. In this study, an artificial neural network model is developed to predict the Nusselt number. A simple neural network architecture is given in Fig 8.3.

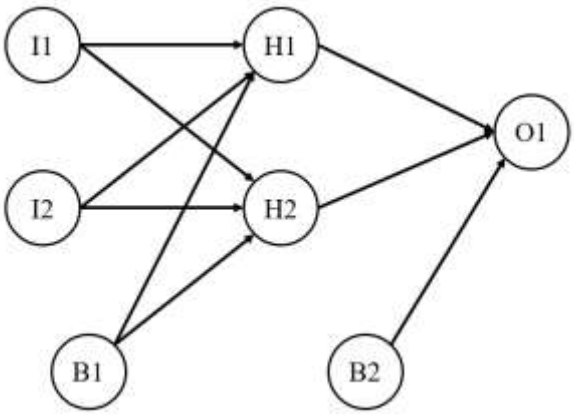

Figure 8.3: A simple artificial neural network architecture with a single hidden layer

Figure 8.3 shows an artificial neural network architecture with one input layer consisting of two neurons, one hidden layer consisting of two neurons, and one output layer consisting of a single neuron. The output of this architecture is the O1 neuron. In order to calculate this neuron, the values of the H1 and H2 neurons must be calculated independently. For the O1 output, the B2 bias neuron only performs a value check on the output and only takes the values 0 or 1.

8.3.1 Activation Functions

In artificial neural networks, the lines between neurons represent the weight. Although the H1 and H2 neurons in Figure 8.3 are fed by the same inputs, the weights and activation functions of the inputs differ. An example of an *S* activation function is given below.

$$S = \left(\sum_{i=1}^{n} w_{ij} x_i + \theta_j \right) \tag{8.10}$$

The fundamental usage of activation functions is to establish the mathematical relationship between input and output. Linear and nonlinear problems can be modeled by using different activation functions for different neurons. Today, most engineering problems do not have a linear relationship between inputs and outputs, so users prefer nonlinear functions. The three most commonly used activation functions are given below.

Linear Activation Function: There is a linear relationship between the input and output values in the linear activation function. If nonlinear problems are modeled using this function, the error in the calculated output value will be larger than in nonlinear models. Its usage is very rare. The linear activation function is given in Eq. 8.11, and its graph is shown in Fig. 8.4.

$$S(x) = x \tag{8.11}$$

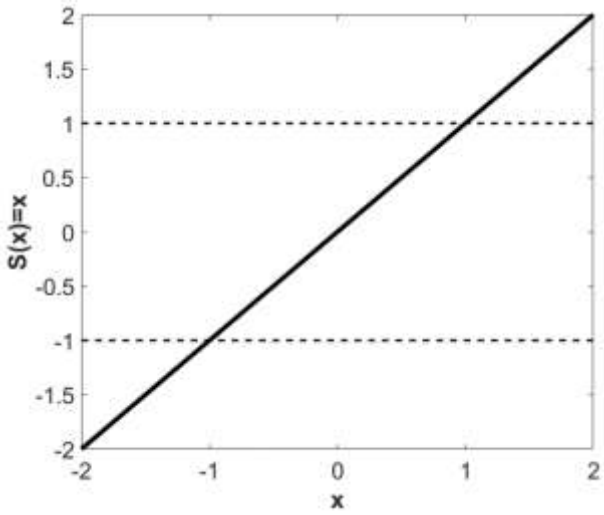

Figure 8.4: Linear activation function graph

Sigmoid Activation Function: The function that is used in nonlinear models. As shown in Fig. 8.5, the output of the function only takes positive values. Therefore, if all the training data are positive, the error values due to the function will be low. The Sigmoid Activation Function is given in Eq. 8.12, and its graph is shown in Fig. 8.5.

$$S(x) = \frac{1}{1 + e^{-x}} \tag{8.12}$$

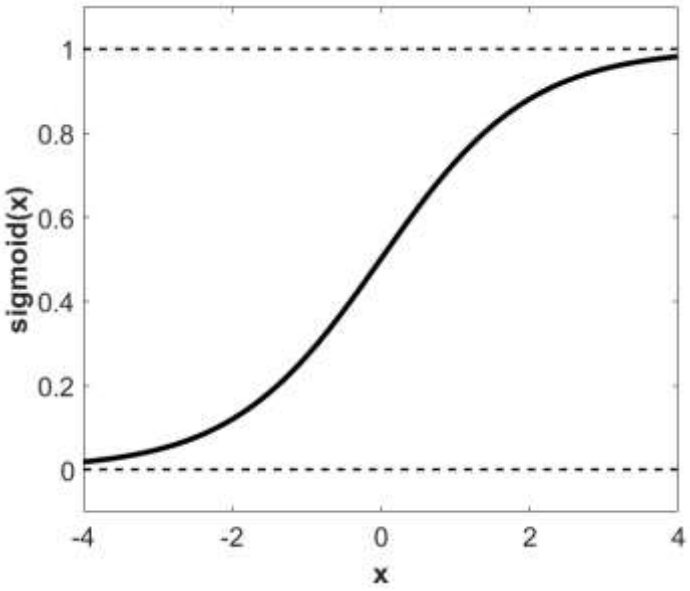

Figure 8.5: Sigmoid activation function graph

Hyperbolic tangent activation function: This function is a nonlinear function that maps its input values to output values within a range of -1 to 1. This function is commonly used in neural networks due to its ability to produce both positive and negative outputs, allowing for a wider range of modeling capabilities compared to other activation functions such as the linear and sigmoid function. The hyperbolic tangent activation function is defined in Eq. 8.13 and its graph is shown in Fig 8.6.

$$S(x) = \frac{e^{2x} - 1}{e^{2x} + 1} \tag{8.13}$$

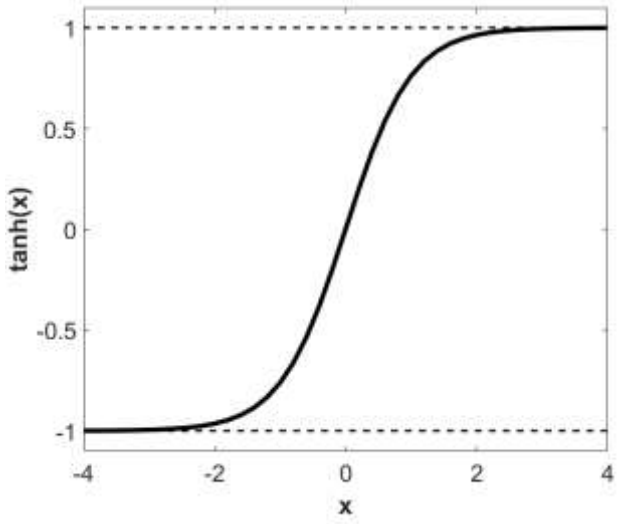

Figure 8.6: Hyperbolic tangent activation function graph

Upon reviewing the literature, it can be seen that more than twenty activation functions are used in artificial neural network applications today. As the use of artificial neural networks expands, new activation functions are also emerging according to need. Other activation functions used in engineering problems are given in Fig. 8.7.

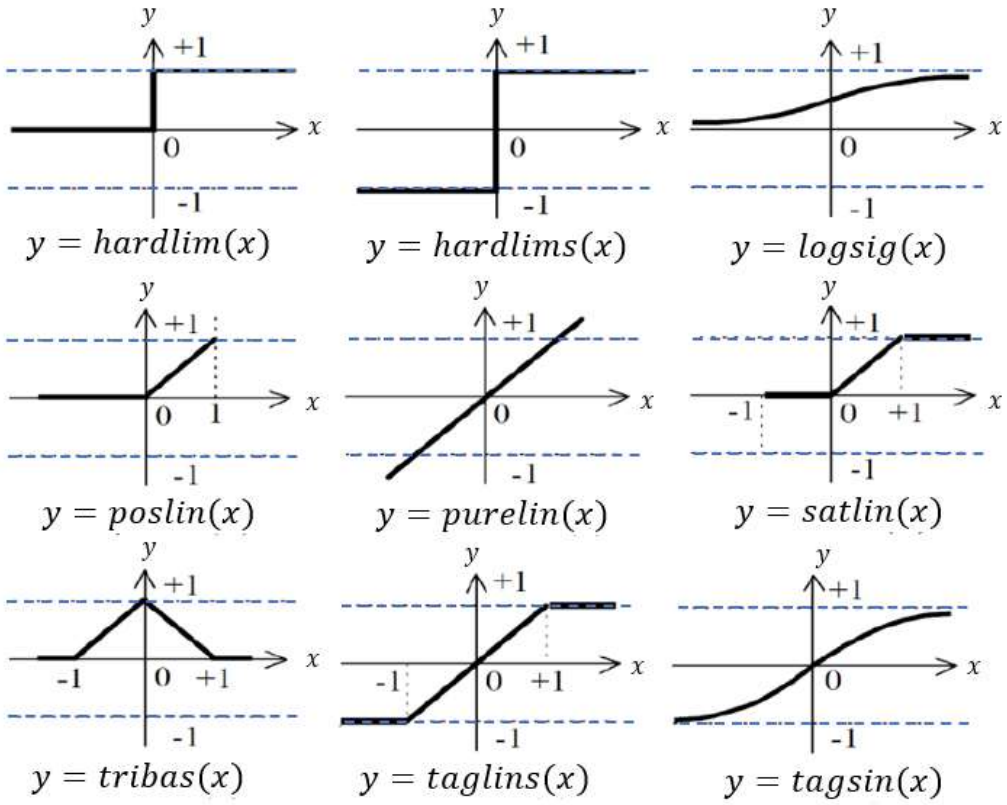

Figure 8.7: Activation functions used for engineering problems in the literature

8.3.2 Bias Value

Activation functions are a parameter that directly affects the error value of the neural network model. Therefore, the higher the flexibility of the use of the activation function, the lower the error rate of the created model. As previously mentioned, the primary input parameter of activation functions is weight. However, some functions can give the same result for different weight values. For example, in Fig. 8.8a, it is seen that the sigmoid activation function gives the same result at x = 0 for four different weight values. This result reduces the flexibility of the function. In such cases, bias values allow the function output to be shifted to the right or left on the x-axis. Thus, the same activation function can be used to expand the calculation range within a

neuron. Figure 8.8b shows the change in the sigmoid function obtained using the same weight value and different bias values.

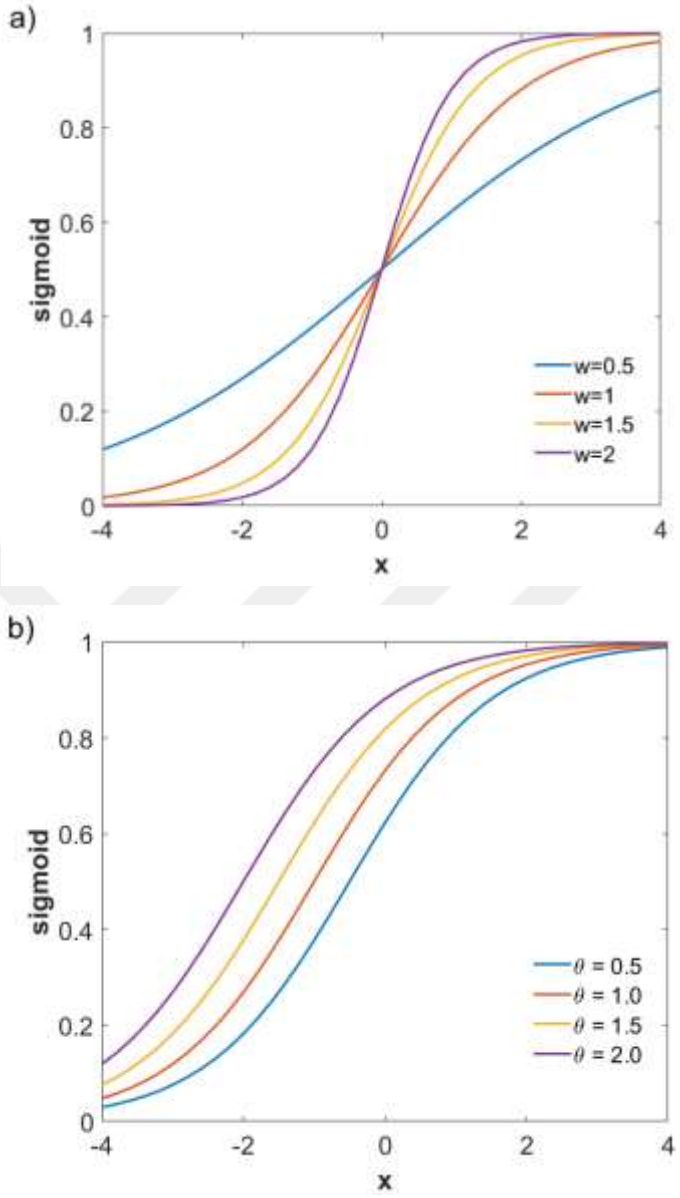

Figure 8.8: Output results for a) different weight values and b) different bias values for the sigmoid activation function.

8.3.3 Hidden Layers

Artificial neural network architectures are divided into three categories: single-layer, multi-layer, and recurrent neural network architectures. The single-layer neural network is the simplest architecture, containing only an input layer and an output layer. The calculations are performed in the output layer, so they are called single-layer. Figure 8.9a shows a single-layer artificial neural network architecture. Multi-layer artificial neural network architectures are created by adding hidden layers to the single-

layer architecture. Hidden layer structures allow for calculations with higher accuracy depending on the number of layers and the activation functions used in the input data. However, a large number of layers does not necessarily mean that the error will definitely decrease. Figure 8.9b shows an artificial neural network architecture with a single hidden layer. In a standard artificial neural network architecture, the elements in the hidden layer are connected to all elements in the next layer.

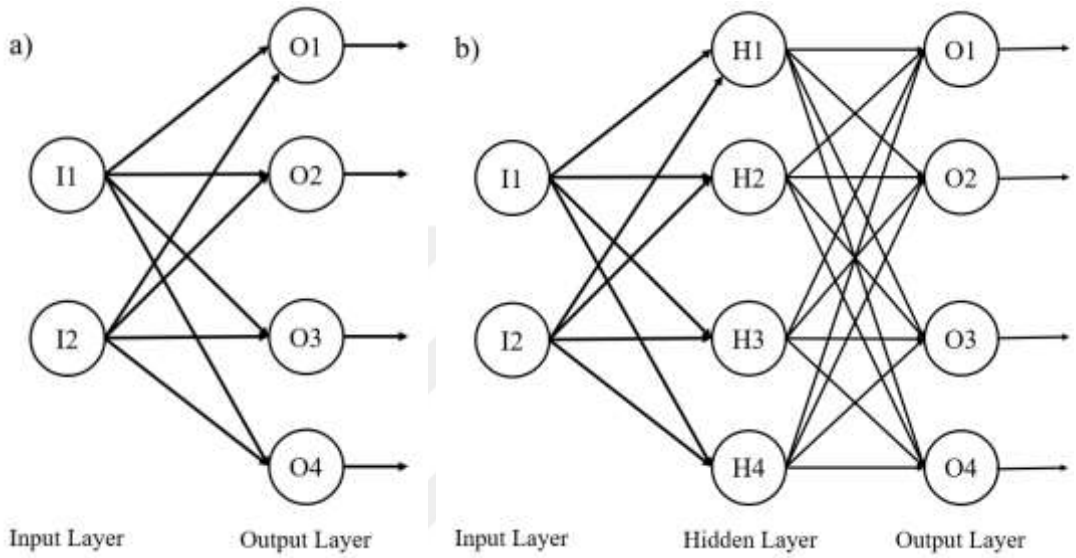

Figure 8.9: Artificial neural network architectures, a) single-layer architecture, b) multi-layer architecture

The most important feature of the recurrent artificial neural network architecture is that it can continuously provide feedback to the input values. They can be used as single-layer or multi-layer. Figure 6.10 shows a single-layer artificial neural network architecture. The unit delay operator in the architecture is used to ensure the continuity of nonlinear feedback. The feedback algorithm allows the neural network to improve its learning ability.

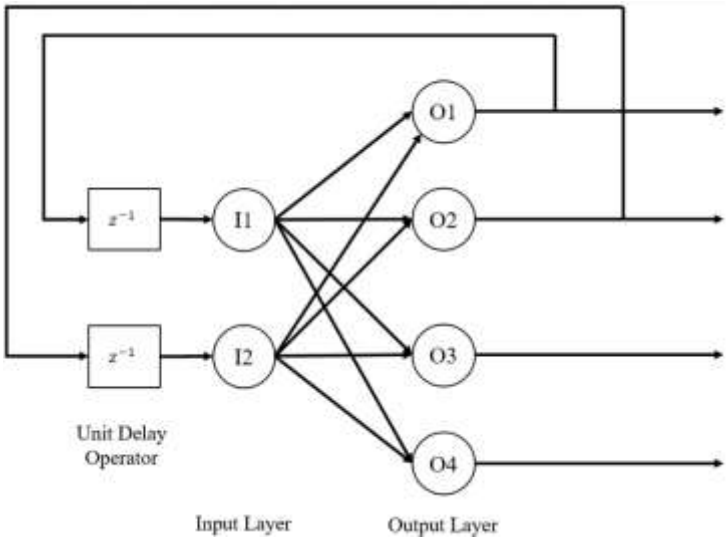

Figure 8.10: Single-layer recurrent artificial neural network architecture

8.3.4 Feedforward and Feedback Networks

Artificial neural networks are classified into two types according to their structures; feedforward networks and feedback networks. In a feedforward network, the process elements are generally divided into layers. The process progresses through unidirectional connections between the input and output layers without delay. The output values are compared with the desired output values from the presented data by the user. Then, an error signal is received, and the network weights are updated to increase the accuracy of the architecture (Galushkin 2007).

In a feedback artificial neural network, there is a network structure in which the outputs in the output and hidden layers are fed back to the input layers or previously hidden layers (Haykin 1998). In this way, inputs are transferred both forward and backward. Calculating errors and finding the optimum weight value takes time in feedback networks. Therefore, the learning time for feedback networks is longer than for feedforward networks (Galushkin 2007). These types of networks have dynamic memories and the output signal responds to both the current and previous inputs. Feedback networks are used especially in prediction applications. In this project, which aims to predict the Nusselt number, a feedback (backpropagation) artificial neural network was used.

The flow chart of the artificial neural network studies to be carried out within the scope of the thesis study is shown in Fig 8.11. As shown in the flow chart, it is necessary to optimize parameters such as learning rate, learning algorithm, number of

hidden layers, and number of hidden layers in determining the final architecture that will minimize the error of the artificial neural network.

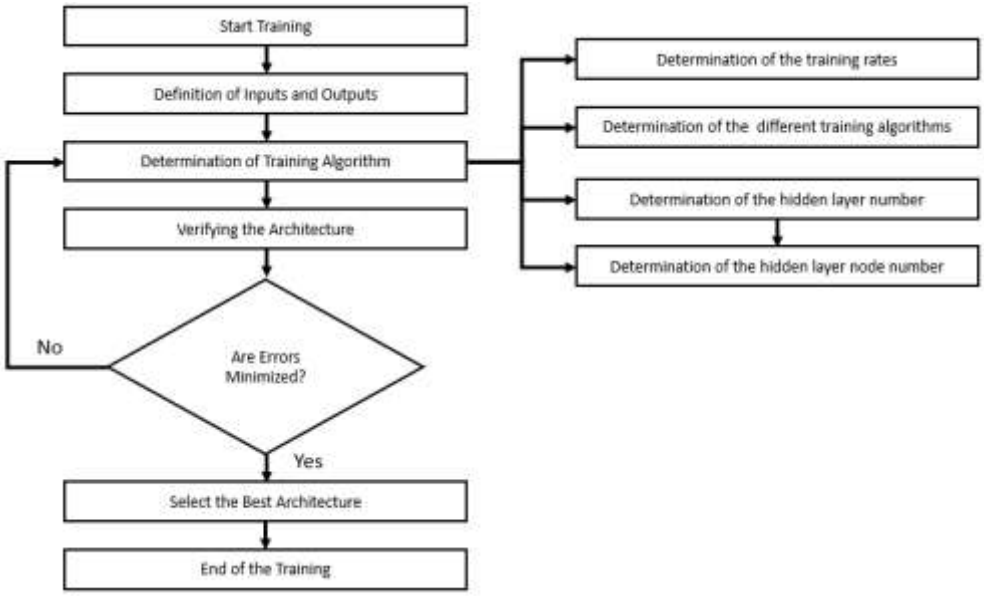

Figure 8.11: The flow chart of the artificial neural network studies

8.3.5 Error Analysis of Artificial Neural Networks

Artificial neural networks, like all other computational methods, are a method of implementation that contains an error in the calculation of outputs. The error in the calculation varies according to the behavior between the inputs and outputs of the models used in the artificial neural network (linear or nonlinear). Therefore, it is necessary to calculate the error amount of each model used in the artificial neural network during the architecture construction and to determine the model with the least error. Knowing this error is also important for knowing the error amount of the results obtained by using this architecture in future studies.

Errors in artificial neural network studies are divided into two, local error and global error. Local errors are obtained from a single neuron and detected using an error function. Global error is calculated by evaluating all of the local errors together. Local error reveals the calculation performance of an activation function in a neuron, while global error determines the calculation performance of the artificial neural network architecture.

In artificial neural network applications, local errors are detected with error functions. The input of a local error function is the real output of a single neuron and

the calculated output. The output of the error function is the error amount obtained from a single neuron. The goal of the training algorithm is to minimize this error.

The most commonly used function for detecting local errors is the linear error function. The linear function calculation uses the equality given below.

$$E = (y_i - y_a) \tag{8.14}$$

In Eq. 8.14, E indicates the error amount, y_i represents the calculated output, and y_a represents the actual output value.

The global error is found by comparing the actual output values with the output values calculated by the artificial neural network. The actual output values are formed by CFD analysis and experimental results in this study. The global error is calculated using the test data that makes up 20% of the data set. The equation for Mean Square Error (RMSE), which is also used for the correlation equation in calculating the global error, is given below.

$$\text{Mean Square Error (RMSE}_\text{n}) = \sqrt{\frac{1}{\text{N}}\sum_{\text{i=1}}^{\text{N}}\left(\frac{\text{y}_\text{i} - \hat{\text{y}}_\text{i}}{\text{y}_\text{i}}\right)^2} \tag{8.15}$$

where N is the validation number, y_i is the real value at the validation node, i, and $\hat{y}_i$ is the calculated model output value at the node i.

To find the maximum deviation value of the global error as a percentage, Eq. 8.16 is used to find the percentage of the maximum absolute error. This allows us to predict the maximum possible error in the results obtained from the model used.

$$\%\text{Maximum Absolute Error} = \max_{\text{i=1,...n}}\left(\frac{|\text{y}_\text{i} - \hat{\text{y}}_\text{i}|}{\text{y}_\text{i}} \times 100\right) \tag{8.16}$$

The average absolute error in Eq. 8.17 can be used to find the average calculation error of the global error.

$$\text{Average Absolute Error} = \frac{1}{N}\sum_{i=1}^{N}\left|\frac{y_i - \hat{y}_i}{y_i}\right| \qquad i = 1, \ldots \ldots . N \qquad (8.17)$$

8.4 CREATING AN ARTIFICAL NEURAL NETWORK

In this study, the aim is to calculate the Nusselt number based on the values of Reynolds number (*Re*), Darcy number (*Da*), the ratio of the porous material height to the channel height (*h/H*), and porosity (φ) using artificial neural network. For this purpose, the data set obtained from experimental and numerical studies was used. For the optimization of the artificial neural network architecture, a data set consisting of the results of a total of 430 different cases, including the effects of different parameters on the Nusselt number, was used. The data set was divided into two parts, with 85% used for training the artificial neural network and 15% used as test data. Backpropagation algorithms such as Bayesian Regularization (BR), Scaled Conjugate Gradient (SCG), and Levenberg-Marquardt (LM) were tested as the training algorithm. The number of hidden layers was changed for each algorithm and the results were tested by error analysis. The number of hidden layers was changed from 1 to 14 in the training stage of the total of 23 different architectures tested. The results of all the architectures used in the study and their performance coefficients are given in Table 8.3. The performance of each architecture was determined based on the R^2 values of the training and test results. When the table is examined, the LM algorithm gave the lowest performance in the 4-4-1 architecture, the BR algorithm in the 4-1-1 architecture, and the SCG algorithm in the 4-4-1 architecture. The highest performance value was obtained with the Bayesian Regularization training algorithm in the 4-6-1 architecture.

Table 8.3. ANN architectures and performance outcomes in this study.

#	**Inputs/ Hidden Layers/ Outputs**	**Training Algorithm**	**R^2**	
			Training	**Testing**
1	4/1/1	Levenberg-Marquardt	0.9281	0.915829
2	4/2/1	Levenberg-Marquardt	0.96482	0.95017
3	4/4/1	Levenberg-Marquardt	0.94742	0.86797
4	4/6/1	Levenberg-Marquardt	0.985	0.95202
5	4/8/1	Levenberg-Marquardt	0.98782	0.949512

Table 8.3 Continue

#	Inputs/ Hidden Layers/ Outputs	Training Algorithm	R^2	
			Training	**Testing**
6	4/10/1	Levenberg-Marquardt	0.98875	0.94835
7	4/12/1	Levenberg-Marquardt	0.98933	0.94879
8	4/14/1	Levenberg-Marquardt	0.9878	0.94012
9	4/1/1	Bayesian Regulation	0.9512	0.94478
10	4/2/1	Bayesian Regulation	0.975045	0.964937
11	4/4/1	Bayesian Regulation	0.97473	0.96299
12	**4/6/1**	**Bayesian Regulation**	**0.97987**	**0.96907**
13	4/8/1	Bayesian Regulation	0.9789	0.96866
14	4/10/1	Bayesian Regulation	0.97957	0.9699
15	4/12/1	Bayesian Regulation	0.9785	0.96752
16	4/14/1	Bayesian Regulation	0.97972	0.96935
17	4/1/1	Scaled Conjugate Gradient	0.9437	0.90051
18	4/2/1	Scaled Conjugate Gradient	0.89761	0.863715
19	4/4/1	Scaled Conjugate Gradient	0.7528	0.72659
20	4/6/1	Scaled Conjugate Gradient	0.85641	0.78421
21	4/8/1	Scaled Conjugate Gradient	0.88901	0.8487
22	4/10/1	Scaled Conjugate Gradient	0.857141	0.77468
23	4/12/1	Scaled Conjugate Gradient	0.8025	0.76141
24	4/14/1	Scaled Conjugate Gradient	0.87585	0.74458

Figure 8.12 shows the R^2 changes based on the number of layers for each training algorithm. As seen in the figures, the accuracy of the outputs obtained during the training process is higher than the accuracy of the outputs obtained during the test process regardless of the training algorithm. The main reason for this result is that the artificial neural network makes corrections to the input signals during its training in the use of the backpropagation architecture. However, the failure to use the correction function used during training for tests leads to a decrease in accuracy level. Nevertheless, it is observed that the test and training curves behave similarly regardless of the training algorithm. In the LM and BR training algorithms with high performance, the R^2 value is nearly constant in architectures with 8 or more hidden layers. As seen in the figures, the effect of the number of layers on accuracy is different in each training algorithm.

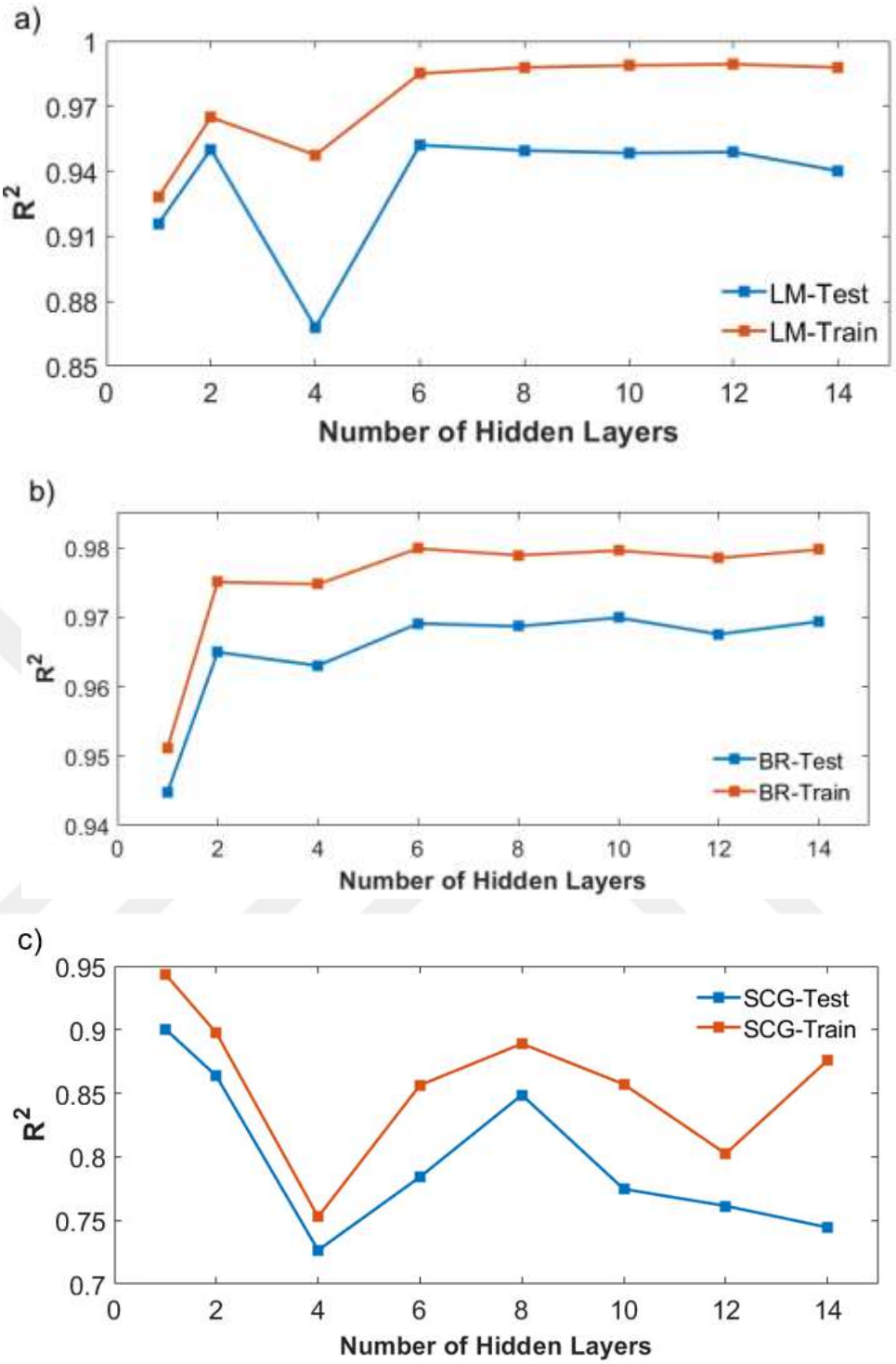

Figure 8.12: Performance change based on the number of layers of different training algorithms a)Levenberg-Marquardt, b)Bayesian Regulation and c) Scaled Conjugate Gradient training algorithm

In Figure 8.13, the performance of the training algorithms is expressed in terms of R^2. LM and BR algorithms perform prediction with high accuracy, while the SCG algorithm shows lower performance. As in Figure 8.12, the change in R^2 based on the number of hidden layers does not exhibit a common behavior. According to the error

analysis, the SCG method has the lowest R^2 values and the highest average error, while the best-performing training algorithm is BR with 6 hidden layers.

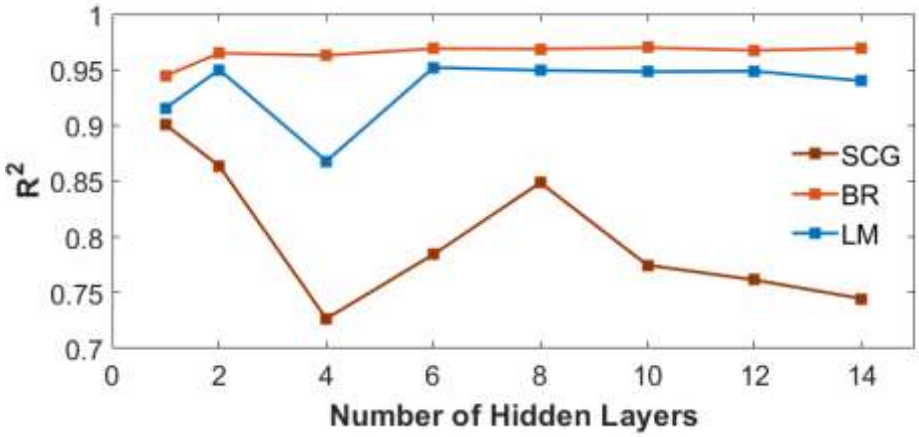

Figure 8.13: Impact of training algorithms on performance

Figure 8.14 shows the training and test data for the best approach 6 hidden layer BR training algorithm and its comparison curves with numerical data. The training R^2 value is 0.97897 and the R^2 value of the test data is 0.96907. The average error value obtained from this BR algorithm with this architecture is quite good, with a value of 1.245% compared to traditional methods.

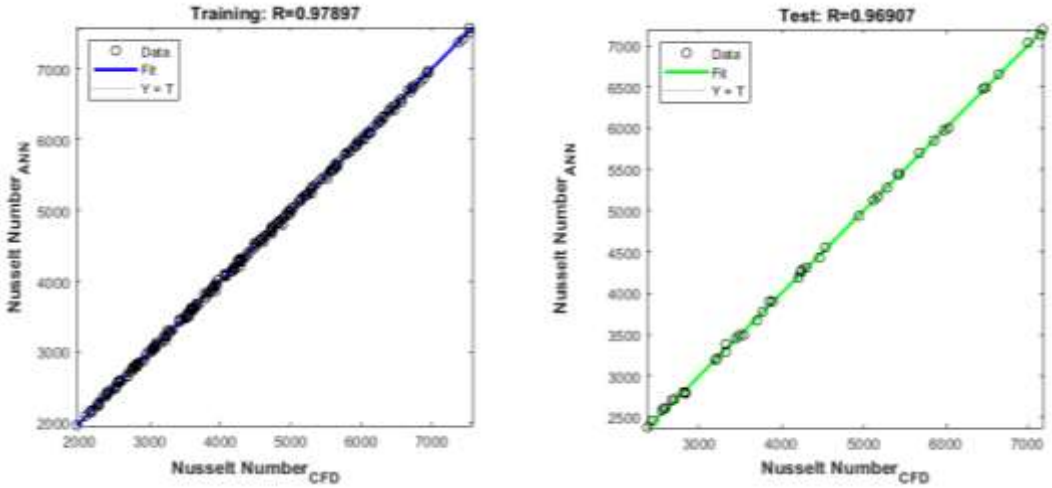

Figure 8.14: Bayesian Regulation training algorithm regression curve with 4-6-1 architecture for best performance

In Figure 8.15, the correlation equation data for both the training and test sets are shown for the ANN prediction results. The average error value decreases from 17.8% to 1.245% when using the best performing ANN architecture. This

demonstrates that an optimized ANN architecture has much higher prediction capability compared to traditional methods.

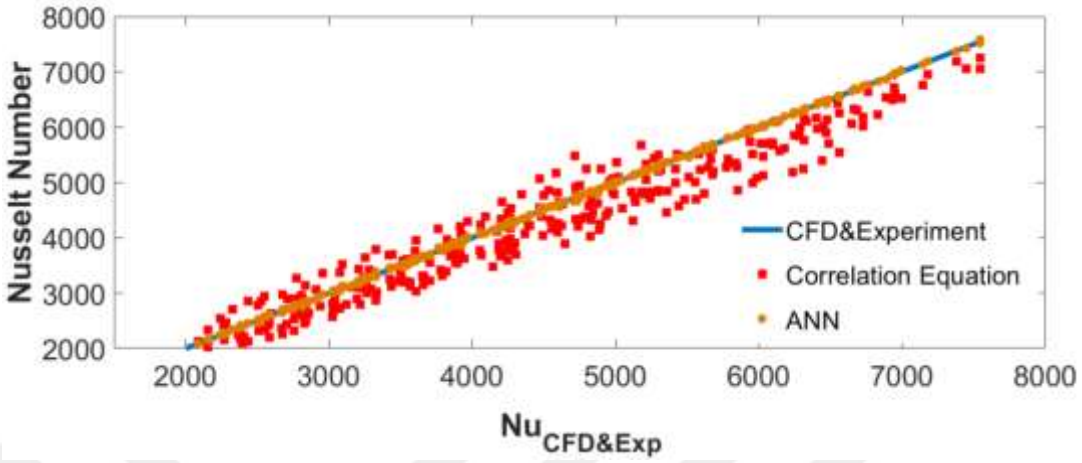

Figure 8.15: Comparison of Nusselt Number from experimental and numerical studies with correlation equation and artificial neural network results

CHAPTER IX
CONCLUSION AND RECOMMENDATIONS

The aim of the thesis study was to investigate the heat transfer and temperature distribution characteristics of an electronic component covered with a porous medium both experimentally and numerically, obtain a correlation and develop an artificial neural network architecture for Nusselt number. An experimental setup was designed and constructed in the Mechanical Engineering laboratory at Çankaya University to conduct heat transfer experiments. For the numerical analysis, a CFD software was developed on the OpenFOAM platform. The experimental results were used to validate the mathematical model and the computer program developed. The validated computer program was used to investigate the effects of Reynolds number, porosity, Darcy number, porous medium sizes and the channel height on the heat transfer rate from the heat-emitting element (electronic component) to the flow and on the temperature of the component. Based on the Nusselt number values obtained both experimentally and numerically, a correlation equation was developed and an artificial neural network architecture was trained for the Nusselt number.

The main conclusions observed from the results of the study are summarized below:

- Porous materials can be used as an alternative technique for the electronic cooling applications.
- The amount of heat generated in electronic components has no effect on the Nusselt number.
- As the Reynolds number of the flow increases, the Nusselt number also increases.
- The porosity of the porous medium is an important parameter affecting the heat transfer rate. The Nusselt number increases with increasing porosity up to porosity of 0.9. However, with further increase in the porosity, the Nusselt number does not change considerable with increasing porosity at a given Reynolds number.

- The ratio of the height of the porous medium to the channel height (*h/H*) is another parameter that is important for the heat transfer. As the *h/H* ratio increases, the average heat transfer coefficient on electronic components increases at a constant Reynolds number.
- The effect of the *h/H* ratio was evaluated by considering two different Nusselt number definition. The Nusselt number defined based on the hydraulic diameter decreases as the *h/H* ratio increases. However, the Nusselt number defined based on the height of the porous medium (*h*) increases as the *h/H* ratio increases.
- The width of the porous medium has no noticeable effect on the Nusselt number.
- The obtained correlation equation contains four different independent parameters contrary to the studies in the literature. By using the Reynolds number, Darcy number, porosity, and the ratio of porous medium height to channel height, the Nusselt number can be obtained with a maximum error of 16.79%.
- Artificial neural network developed reveals as a better tool compared to traditional statistical methods for the determination of Nusselt number. Using the artificial neural network architecture developed within the scope of the thesis, the Nusselt number can be obtained with a maximum error of 1% for similar systems.

The following works are recommended for future studies:

- In this study, the numerical and experimental simulations were performed for the components with parous medium and with no porous medium. A direct comparison with the fin structures used traditionally should be made to better demonstrate the advantages and disadvantages porous layers compared with fin structures in electronic cooling applications.
- The artificial neural network architecture may be improved using different neural networks, such as Feedforward Neural Networks, Deep Neural Networks, or Radial Basis Function Networks.

REFERENCES

ADHIKARI R.C., WOOD D.H. and PAHLEVANI M. (2020), "An experimental and numerical study of forced convection heat transfer from rectangular fins at low Reynolds numbers", *International Journal of Heat and Mass Transfer*, Vol. 163, No. 120418, DOI: 10.1016/j.ijheatmasstransfer.2020.120418.

AHMADI M., MOSTAFAVI G. and BAHRAMI M. (2014), "Natural convection from rectangular interrupted fins", *International Journal of Thermal Sciences*, Vol. 82, pp. 62–71, DOI: 10.1016/j.ijthermalsci.2014.03.016.

AKRIDISS ABED S., SETTAR A., CHETEHOUNA K., KADIRI M.S., El TABACH E. and Gascoin N. (2020), "Numerical study on a porous material subject to SiC particles deposition, using OpenFOAM and sensitivity analysis technique: Effect of clogging evolution on the thermal performances", *Chemical Engineering Science*, Vol. 212, p. 115321, DOI: 10.1016/j.ces.2019.115321.

ALESSA A.H., AL-WIDYAN M.I. and JIAN-ZHONG C.L.I.N. (2008), "Enhancement of natural convection heat transfer from a fin by triangular perforation of bases parallel and toward its tip ", Vol. 29, No. 8, pp. 1033–1044, DOI: 10.1007/s10483-008-0807-x.

ALOMAR O.R., MENDES M.A.A., TRIMIS D. and RAY S. (2015), "Simulation of complete liquid–vapour phase change process inside porous evaporator using local thermal non-equilibrium model", *International Journal of Thermal Sciences*, Vol. 94, pp. 228–241, DOI: 10.1016/j.ijthermalsci.2015.03.007.

AWASARMOL U. and PISE A.T. (2015), "An experimental investigation of natural convection heat transfer enhancement from perforated rectangular fins array at different inclinations", *Experimental Thermal and Fluid Science*, Vol. 68, pp. 145–154, DOI :10.1016/j.expthermflusci.2015.04.008.

BAUER T.H. (1993), “A general analytical approach toward the thermal conductivity of porous media”, *International Journal of Heat and Mass Transfer*, Vol. 36, No. 17, pp. 4181–4191, DOI :10.1016/0017-9310(93)90080-P.

BHATTACHARYA A. and MAHAJAN R.L. (2002), “Finned Metal Foam Heat Sinks for Electronics Cooling in Forced Convection”, *Journal of Electronic Packaging*, Vol. 124, No. 3, pp. 155–163, DOI :10.1115/1.1464877.

BINGHAM N.M. and FRY J.M. (2011), *Regression: Linear Models in Statistics*, Springer London, UK.

BRINKMAN H.C. (1949), “A calculation of the viscous force exerted by a flowing fluid on a dense swarm of particles”, *Flow, Turbulence and Combustion*, Vol. 1, No. 1, p. 27.

CALMIDI V. V and MAHAJAN R.L. (1999), “The Effective Thermal Conductivity of High Porosity Fibrous Metal Foams”, *Journal of Heat Transfer*, Vol. 121, No. 2, pp. 466–471, DOI:10.1115/1.2826001.

COELHO P.M. and PINHO F.T. (2009), “A generalized Brinkman number for non-Newtonian duct flows”, *Journal of Non-Newtonian Fluid Mechanics*, Vol. 156, No. 3, pp. 202–206, DOI:10.1016/j.jnnfm.2008.07.001.

DOGAN M. and SIVRIOGLU M. (2009), “Experimental investigation of mixed convection heat transfer from longitudinal fins in a horizontal rectangular channel: In natural convection dominated flow regimes”, *Energy Conversion and Management*, Vol. 50, No. 10, pp. 2513–2521, DOI: 10.1016/j.enconman.2009.05.027.

DRAPER N.R. and SMITH H. (1998), *Applied Regression Analysis*, Third Edition, John Wiley & Sons, Inc, New York.

EJLALI A., EJLALI A., HOOMAN K. and GURGENCI H. (2009), “Application of high porosity metal foams as air-cooled heat exchangers to high heat load removal systems”, *International Communications in Heat and Mass Transfer*, Vol. 36, No. 7, pp. 674–679, DOI: 10.1016/j.icheatmasstransfer.2009.03.001.

ERGUN S. (1952), “Fluid flow through packed columns”, *Chem. Eng. Prog.*, Vol. 48, pp. 89–94.

FERZIGER J.H. and PERIĆ M. (2002), *Computational Methods for Fluid Dynamics*, Springer, Berlin, Heidelberg, DOI: 10.1007/978-3-642-56026-2.

FIEDLER T., PESETSKAYA E., ÖCHSNER A. and GRÁCIO J. (2006), "Calculations of the thermal conductivity of porous materials", *Materials Science Forum*, Vol. 514–516, No. PART 1, pp. 754–758, DOI: 10.4028/www.scientific.net/msf.514-516.754.

FORCHHEIMER P. (1901), "Wasserbewegung durch boden", *Z. Ver. Deutsch, Ing.*, Vol. 45, pp. 1782–1788.

FOX R. and MCDONALD A. (2009), *Introduction to fluid mechanics*, Wiley, New York.

GALUSHKIN A. (2007), *Neural Networks Theory*, Springer Berlin, Heidelberg.

GHANBARIAN B. and Daigle H. (2016), "Thermal conductivity in porous media: Percolation-based effective-medium approximation", *Water Resources Research*, Vol. 52, No. 1, pp. 295–314, DOI: 10.1002/2015WR017236.

HAMADOUCHE A., NEBBALI R., BENAHMED H., KOUIDRI A. and BOUSRI A. (2016), "Experimental investigation of convective heat transfer in an open-cell aluminum foams", *Experimental Thermal and Fluid Science*, Vol. 71, pp. 86–94, DOI: 10.1016/j.expthermflusci.2015.10.009.

HARAHAP F. and MCMANUS Jr. H.N. (1967), "Natural Convection Heat Transfer From Horizontal Rectangular Fin Arrays", *Journal of Heat Transfer*, Vol. 89, No. 1, pp. 32–38, DOI: 10.1115/1.3614318.

HARAHAP F. and SETIO D. (2001), "Correlations for heat dissipation and natural convection heat-transfer from horizontally-based, vertically-finned arrays", *Applied Energy*, Vol. 69, No. 1, pp. 29–38, DOI: 10.1016/S0306-2619(00)00073-8.

HAYKIN S. (1998), *Neural Networks: A Comprehensive Foundation*, Second Edition, Prentice Hall PTR, USA.

HOLMAN J.P. (1971), *Experimental Methods for Engineers*, Eight Edition, McGraw-Hill Book Company, New York.

HOLZMANN T. (2019), *Mathematics, Numerics, Derivations and OPENFOAM*. https://holzmann-cfd.com/community/publications/mathematics-numerics-derivations-and-openfoam-free, DoA. 02.03.2023.

HSIEH W.H., WU J.Y., SHIH W.H. and CHIU W.C. (2004), "Experimental investigation of heat-transfer characteristics of aluminum-foam heat sinks", *International Journal of Heat and Mass Transfer*, Vol. 47, No. 23, pp. 5149–5157, DOI: 10.1016/j.ijheatmasstransfer.2004.04.037.

HWANG G.J., WU C.C. and CHAO C.H. (1995), “Investigation of Non-Darcian Forced Convection in an Asymmetrically Heated Sintered Porous Channel”, *Journal of Heat Transfer*, Vol. 117, No. 3, pp. 725–732, DOI: 10.1115/1.2822636.

HWANG J.J., HWANG G.J., YEH R.H. and CHAO C.H. (2002), “Measurement of interstitial convective heat transfer and frictional drag for flow across metal foams”, *Journal of Heat Transfer*, Vol. 124, No. 1, pp. 120–129, DOI: 10.1115/1.1416690.

HYUNG J.S., Seo Y.K. and JAE M.H.. (1995), “Forced convection from an isolated heat source in a channel with porous medium”, *International Journal of Heat and Fluid Flow*, Vol. 16, No. 6, pp. 527–535, DOI: 10.1016/0142-727X(95)00032-L.

Intel Corporation (2018), *Intel Xeon Processor Scalable Family Thermal Mechanical Specifications and Design Guide*. https://www.intel.com/content/dam/www/public/us/en/documents/guides/xeon-scalable-thermal-guide.pdf, DoA. 02.03.2023.

ICHIMIYA K. (1999), “A New Method for Evaluation of Heat Transfer Between Solid Material and Fluid in a Porous Medium”, *Journal of Heat Transfer*, Vol. 121, No. 4, pp. 978–983, DOI: 10.1115/1.2826089.

IZADPANAH M.R., MÜLLER-STEINHAGEN H. and JAMIALAHMADI M. (1998), “Experimental and theoretical studies of convective heat transfer in a cylindrical porous medium”, *International Journal of Heat and Fluid Flow*, Vol. 19, No. 6, pp. 629–635, DOI: 10.1016/S0142-727X(98)10035-8.

JONES C.D. and SMITH L.F. (1970), “Optimum Arrangement of Rectangular Fins on Horizontal Surfaces for Free-Convection Heat Transfer”, *Journal of Heat Transfer*, Vol. 92, No. 1, pp. 6–10, DOI: 10.1115/1.3449648.

KAKAC S., SHAH R.K. and AUNG W. (1987), *Handbook of Single-Phase Convective Heat Transfer*, John Wiley and Sons Inc, United States.

KO K.H. and ANAND N.K. (2003), “Use of porous baffles to enhance heat transfer in a rectangular channel”, *International Journal of Heat and Mass Transfer*, Vol. 46, No. 22, pp. 4191–4199, DOI: 10.1016/S0017-9310(03)00251-5.

KO Y.M., LEUNG C.W. and PROBERT S.D. (1989), “Steady-state free-convective cooling of heat exchangers with vertical rectangular fins: Effect of fin material”, *Applied Energy*, Vol. 34, No. 3, pp. 181–191, DOI: 10.1016/0306-2619(89)90045-7.

KURTBAS I. and CELIK N. (2009), “Experimental investigation of forced and mixed convection heat transfer in a foam-filled horizontal rectangular channel”, *International Journal of Heat and Mass Transfer*, Vol. 52, No. 5–6, pp. 1313–1325, DOI: 10.1016/j.ijheatmasstransfer.2008.07.050.

LEDEZMA G. and BEJANT A. (1996), “Heat sinks with sloped plate fins in natural and forced convection”, *Int. J. Heat Mass Transfer*, Vol. 39, No. 9, pp. 1773–1783.

LEE J., KIM H. and KIM D.K. (2017), “Thermal Optimization of Horizontal Tubes with Tilted Rectangular Fins under Free Convection for the Cooling of Electronic Devices”, *Applied Sciences*, Vol. 7, No. 4, p. 352, DOI: 10.3390/app7040352.

LEONG K.C. and JIN L.W. (2005), “An experimental study of heat transfer in oscillating flow through a channel filled with an aluminum foam”, *International Journal of Heat and Mass Transfer*, Vol. 48, No. 2, pp. 243–253, DOI: 10.1016/j.ijheatmasstransfer.2004.08.025.

LEUNG C.W., PROBERT S.D. and SHILSTON M.J. (1985), “Heat exchanger design: Optimal uniform separation between rectangular fins protruding from a vertical rectangular base”, *Applied Energy*, Vol. 19, No. 4, pp. 287–299, DOI: https://doi.org/10.1016/0306-2619(85)90003-0.

LU W., ZHAO C.Y. and TASSOU S.A. (2006), “Thermal analysis on metal-foam filled heat exchangers . Part I : Metal-foam filled pipes”, *International Journal of Heat and Mass Transfer*, Vol. 49, pp. 2751–2761, DOI: 10.1016/j.ijheatmasstransfer.2005.12.012.

MANCIN S., ZILIO C., ROSSETTO L. and CAVALLINI A. (2011), “Heat Transfer Performance of Aluminum Foams”, *Journal of Heat Transfer*, Vol. 133, No. 6, 060904, DOI: 10.1115/1.4003451.

MANCIN S., ZILIO C., ROSSETTO L. and CAVALLINI A. (2012), “Foam height effects on heat transfer performance of 20 ppi aluminum foams”, *Applied Thermal Engineering*, Vol. 49, pp. 55–60, DOI: 10.1016/j.applthermaleng.2011.05.015.

NIELD D.A. and BEJAN A. (2013), *Convection in Porous Media*, Springer, New York.

NOH J.S., LEE K.B. and LEE C.G. (2006), "Pressure loss and forced convective heat transfer in an annulus filled with aluminum foam", *International Communications in Heat and Mass Transfer*, Vol. 33, No. 4, pp. 434–444, DOI: 10.1016/j.icheatmasstransfer.2005.11.003.

OLSON D.A. (1992), "Heat Transfer in Thin, Compact Heat Exchangers With Circular, Rectangular, or Pin-Fin Flow Passages", *Journal of Heat Transfer*, Vol. 114, No. 2, pp. 373–382, DOI: 10.1115/1.2911285.

PATANKAR S. V. (1980), *Numerical Heat Transfer and Fluid Flow*, CRC Press, USA, DOI: 10.1201/9781482234213.

PENG Y. (1984), "Heat Transfer and Friction Loss Characteristics of Pin Fin Cooling Configurations", *Journal of Engineering for Gas Turbines and Power*, Vol. 106, No. 1, pp. 246–251, DOI: 10.1115/1.3239544.

SETTAR A., ABBOUDI S. and LEBAAL N. (2018), "Effect of inert metal foam matrices on hydrogen production intensification of methane steam reforming process in wall-coated reformer", *International Journal of Hydrogen Energy*, Vol. 43, No. 27, pp. 12386–12397, DOI: 10.1016/j.ijhydene.2018.04.215.

STEINBERG D.S. (1991), "*Cooling Techniques for Electronic Equipment*", Wiley, New York.

TAHAT M., KODAH Z.H., JARRAH B.A. and PROBERT S.D. (2000), "Heat transfers from pin-fin arrays experiencing forced convection", *Applied Energy*, Vol. 67, No. 4, pp. 419–442, DOI: 10.1016/S0306-2619(00)00032-5.

TAMIL A.M. (2022), *Correlation & Linear Regression,* http://www.slideshare.net/drtamil/pearson-correlation-spearmancorrelation-linear-regression, DoA. 02.03.2023.

TU J., YEOH G.H. and LIU C. (2008), *CFD Techniques The Basics*, Butterworth-Heinemann, Burlington.

TURKOGLU H. (1990), *Transport Processes in Gas-Injected Liquid Baths* (Doctoral Dissertation), Drexel University, USA.

TZENG S. (2007), "Spatial thermal regulation of aluminum foam heat sink using a sintered porous conductive pipe", Vol. 50, pp. 117–126, DOI: 10.1016/j.ijheatmasstransfer.2006.06.034.

TZENG S.C. and Jeng T.M. (2006), “Convective heat transfer in porous channels with 90-deg turned flow”, *International Journal of Heat and Mass Transfer*, Vol. 49, No. 7–8, pp. 1452–1461, DOI: 10.1016/j.ijheatmasstransfer.2005.09.024.

WENDT J.F. (2009), *Computational Fluid Dynamics*, Springer, Berlin, Heidelberg, DOI: 10.1007/978-3-540-85056-4.